ΕΘΝΙΚΟ ΜΕΤΣΟΒΙΟ ΠΟΛΥΤΕΧΝΕΙΟ
ΔΠΜΣ: ΥΠΟΛΟΓΙΣΤΙΚΗ ΜΗΧΑΝΙΚΗ
ΚΑΤΕΥΘΥΝΣΗ ΜΗΧΑΝΙΚΗ ΤΩΝ ΣΤΕΡΕΩΝ

Πειραματικά και υπολογιστικά μοντέλα μαλακών βιολογικών ιστών

Μεταπτυχιακή εργασία

Άρτεμις Ν. Κούβακα

Επιβλέποντες Καθηγητές: Σωτήριος Κορώσης,
Χριστόφορος Προβατίδης

Αθήνα 2014

Εξεταστική επιτροπή

Ευστάθιος Θεοτόκογλου	Καθηγητής Εθνικού Μετσόβιου Πολυτεχνείου
Αιμίλιος Σιδερίδης	Λέκτορας Εθνικού Μετσόβιου Πολυτεχνείου
Χριστόφορος Προβατίδης	Καθηγητής Εθνικού Μετσόβιου Πολυτεχνείου (Επιβλέπων)

NATIONAL TECHNICAL UNIVERSITY OF ATHENS
DPMS: COMPUTATIONAL MECHANICS
SOLID MECHANICS

Experimental and computational models of soft biological tissue

Master Thesis

Kouvaka Artemis

Supervisors: Sotirios Korossis,
Christopher Provatidis

Athens 2014

.....

Κούβακα Άρτεμις

Διπλωματούχος Εφαρμοσμένων Μαθηματικών και Φυσικών Επιστημών Ε.Μ.Π.

Στο Νίκο, τη Βάσω, τον Ιάσων και την Κατερίνα

Περίληψη

Σκοπός της παρούσας εργασίας είναι η μελέτη της επίδρασης του preconditioning στις μηχανικές ιδιότητες των μαλακών βιολογικών. Θα χρησιμοποιηθούν πειραματικές και υπολογιστικές μέθοδοι που αποσκοπούν στον προσδιορισμό των μηχανικών ιδιοτήτων του ιστού, με βασικό στόχο την ανάδειξη των διαφορών που επέρχονται στο υλικό του ιστού από το preconditioning.

Οι μηχανικές ιδιότητες των αρτηριακών τοιχωμάτων έχουν ενδιαφέρον επειδή επηρρεάζουν την αρτηριακή βιολογία κατι την ανάπτυξη και πρόοδο αρτηριακών νόσων μέσω της επίδρασης τους στη ροή του αίματος και την ανάπτυξη της αρτηριακής μάζας. Επιπλέον, οι τάσεις και παραμορφώσεις που αναπτύσσονται στα αρτηριακά τοιχώματα είναι εξαιρετικής σημασίας παράγοντες στην κατανόηση της παθοφυσιολογίας και μηχανικής του καρδιαγγειακού συστήματος, πεδία με τα οποία η αναγεννητική μηχανική των ιστών συνδέεται άμεσα. Οι τάσεις και παραμορφώσεις δε μπορούν να αναλυθούν περαιτέρω χωρίς ακριβή γνώση των μηχανικών ιδιοτήτων των τοιχωμάτων.

Η παρούσα εργασία εξετάζει την μηχανική απόκριση λωρίδων χοιρινής θωρακικής αορτής κατά την αξονική και την περιμετρική κατεύθυνση κάτω από μονοαξονική επιμήκυνση ως τη θραύση χαμηλού παραμορφωσιακού ρυθμού. Τέσσερις ομάδες δοκιμίων εξετάστηκαν (n =6 ανά ομάδα), ανά κάθε κατεύθυνση, με ή χωρίς preconditioning. Τα δεδομένα φορτίου – μετατόπισης μετατράπηκαν σε γραφήματα τάσης – παραμόρφωσης από τα οποία υπολογίστηκαν οι εξής παράμετροι:

- Μέτρο ελαστικότητας της φάσης ελαστίνης
- Μέτρο ελαστικότητας της φάσης κολλαγόνου
- Παραμόρφωση μετάβασης
- Τάση μετάβασης
- Μέγιστη τάση επιμήκυνσης
- Παραμόρφωση αστοχίας

Οι παραπάνω παράμετροι ελέχθηκαν για παρουσία στατιστικώς σημαντικών διαφορών χρησιμοποιώντας το t – test του Student ανάμεσα στις ομάδες με και χωρίς preconditioning για την αξονική και περιφερειακή κατεύθυνση. Έπειτα, οι καμπύλες τάσεων – παραμορφώσεων χρησιμοποιήθηκαν για την εύρεση μοντέλων υλικών που περιγράφουν καλύτερα την συμπεριφορά του ιστού.

Τα μοντέλα με υψηλό ποσοστό συσχέτισης πειραματικών δεδομένων με θεωρητικών προβλέψεων χρησιμοποιήθηκαν για την υλοποίηση ενός υπολογιστικού μοντέλου της αορτής με πεπερασμένα στοιχεία. Η αορτή μοντελοποιήθηκε ως ενας σωλήνας σταθερού πάχους κάτω από εσωτερική πίεση 120 mmHg (μέγιστη φυσιολογική *in vivo* πίεση). Δύο γεωμετρίες υλοιποιήθηκαν. Η μία περιλάμβανε το μοντέλο αορτής με τους βαθμούς ελευθερίας των δύο άκρων του πλήρως δεσμευμένους και η δεύτερη τους βαθμούς του ενός άκρου πλήρως δεσμευμένους ενώ το άλλο άκρο ήταν ελεύθερο με ένα έμβολο ενσωματωμένο. Τα αποτελέσματα των υπολογιστικών προσομοιώσεων συγκρίθηκαν με πειραματικά δεδομένα από τη βιβλιογραφία.

Λέξεις κλειδιά : Preconditioning, θωρακική αορτή χοίρου, πεπερασμένα στοιχεία, μοντέλα υλικών, μονοαξονική έπιμήκυνση, μηχανική του καρδιαγγειακού συστήματος, υπολογιστικά μοντέλα

Abstract

The purpose of this thesis is the examination of the effect of preconditioning on the mechanical properties of soft biological tissue. Experimental and computational methods will be used to determine the mechanical properties of the tissue with the highlighting of the differences that occur in the tissue material from preconditioning being the main objective.

Mechanical properties of arterial walls are of interest because they influence arterial biology and the development and progress of arterial diseased via effect on blood flow an arterial mass transport. In addition, stresses and strains developed in arterial walls are extremely important factors in the understanding of the pathophysiology and mechanics of the cardiovascular system. The stress and strain cannot be analysed without exact knowledge of the mechanical properties of the wall.

The present thesis examines the mechanical response of strips of porcine thoracic aorta along the axial and circumferential directions under low strain rate uniaxial loading to failure. Four groups of samples were tested (n = 6 per group) along the two directions, with or without preconditioning. The load – elongation data were transformed into stress – strain curves from which the following parameters were calculated:

- Elastin phase elastic modulus
- Collagen phase elastic modulus
- Transition strain
- Transition stress
- Ultimate tensile strength
- Failure strain

Student's t – test was used to detect significant differences between the groups with and without preconditioning for the axial and circumferential directions. The stress – strain curves were then used for the fitting of material models that better described the mechanical behaviour of the tissue.

The best models were then used for the implementation of a computational model of the aorta with finite elements. The aorta was modelled as a straight tube with constant thickness under internal pressure equal to the maximum physiological *in vivo* pressure (120 mmHg). Two geometries were implemented. In the first geometry the ends of the aorta model had all the degrees of freedom fixed and in the second the degrees of freedom of one end were fixed while the other one was free and plugged. The results of the computational simulations were compared to literature results from inflation tests of the porcine thoracic aorta.

Keywords : Preconditioning, thoracic porcine aorta, finite elements, material models, uniaxial tension, cardiovascular biomechanics, computational models

Acknowledgements

Upon the completion of this master thesis I feel the need to thank each and every one that supported, encouraged and contributed with every means to its completing. I would like to thank my parents for the trust they have showed in me all these years and for their unconditional support.

First and foremost I would like to thank my supervisors Professor Provatidis for assigning and supervising this thesis and Dr. Korossis for choosing the subject, guiding, supporting and giving me the chance to come to Hannover to work with him, meet brilliant people and learn so much. Also thank you to Dr. Andres Hilfiker and Dr. Michael Harder for their comments and suggestions on the project.

Special thanks go to Panos Kalozoumis and Sophia Andriopoulou whose help in the technical and laboratory part of this project was of paramount importance . I would also like to say a big thank you to Dr. Lucrezia Morticelli who trained me in the biomechanical experimental techniques and was always willing and happy to answer all my questions.

Finally, thank you to my colleagues here at CrossBIT, Marisa, Eirini, Nikos, Sonia and Daniele for all their help and friendship. I would also like to deeply thank Katerina for her kind words and for always believing in me and supporting me regardless of the circumstances.

This research was funded by the People Programme (Marie Curie Actions) of the European Union's Seventh Framework Programme FP7/2007-2013/ under REA grant agreement n° 317512.

Table of Contents

List of Tables

List of Figures

1. LITERATURE REVIEW

1.1 Function and anatomy of the heart

The heart is a powerful engine – a muscular pump that propels the blood throughout the body. The heart consists of four chambers: the left and right side each have an atrium and a ventricle. When the blood comes into the heart it is collected in the upper chambers, the atria, and then it is pumped through the lower chambers, the ventricles, throughout the body and the lungs. The unidirectional flow of the blood is achieved with a set of four valves. The atrioventricular valves (tricuspid and mitral) only allow blood to pass from the atria to the ventricles and the semilunar valves (aortic and pulmonary) only allow the blood to flow out of the heart through the great arteries.

The right side of the heart receives the de-oxygenated blood that comes from the body and pumps it into the lungs. The blood vessels that carry blood to and from the lungs form the pulmonary circuit. The left side of the heart receives the freshly oxygenated blood returning from the lungs and pumps it throughout the body, supplying it with oxygen and nutrients. The vessels that carry blood to and from the body form the systemic circuit. Although the ventricles pump the same amount of blood with each contraction the left ventricle is much thicker and stronger than the right one. This is due to the fact that the pressure needed to overcome the high resistance required to pump blood into the long systemic circulation is much greater than the pressure needed for the shorter pulmonary circulation.

A cross section of the heart reveals three layers: the visceral pericardium, the middle myocardium and a deep lining called the endocardium. The contracting layer is the myocardium which consists of cardiac muscles arranged in a spiral “8 like” fashion. The left ventricle is connected to the blood vessel that carries oxygenated blood to the rest of the body called the aorta.

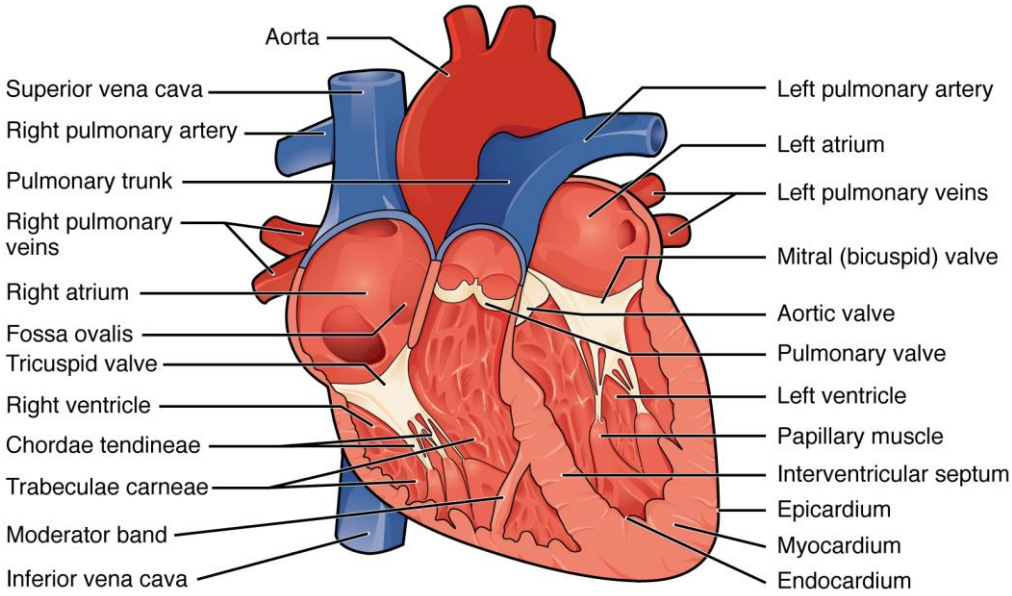

Figure 1.1: Anterior view of the heart showing the major blood vessels and their early branches, the two atria, the two ventricles and the valves (OpenStax 2013)

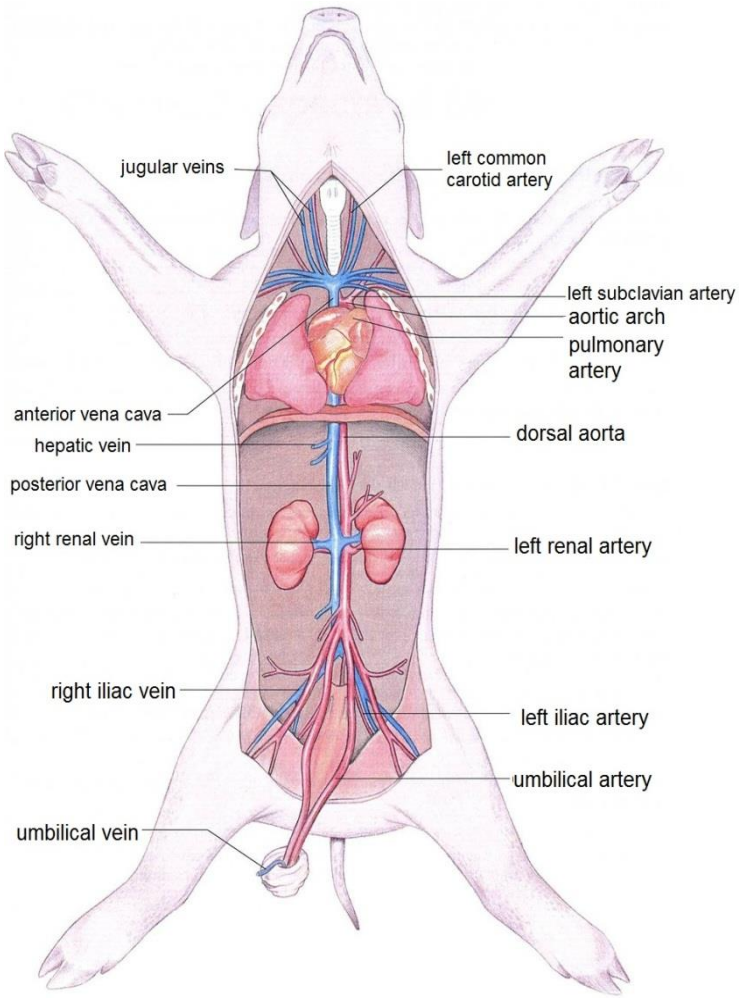

Figure 1.2: Fetal porcine anatomy of the cardiovascular system. (www.biologycorner.com, The Ultimate Fetal Pig Dissection Review)

The aorta is the largest blood vessel in the body approximately 20 mm in diameter. The right ventricle is connected to the pulmonary artery that carries the de-oxygenated blood to the lungs.

A normal porcine heart has many similarities to the human one. It is approximately the size of a large fist and it is located in the middle of the two lungs in the centre of the chest cavity. It is enclosed in a tough, membranous, double-walled sheet called the pericardial sac. The superficial part of the pericardial sac is the fibrous pericardium which protects the heart, anchors it to the surrounding tissues and prevents overfilling of the heart with blood. The inner layer that is in contact with the heart is the visceral pericardium. Between these two layers is the pericardial cavity which contains is a serous fluid. The fluid provides lubrication between the layers so the heart can move with little friction.

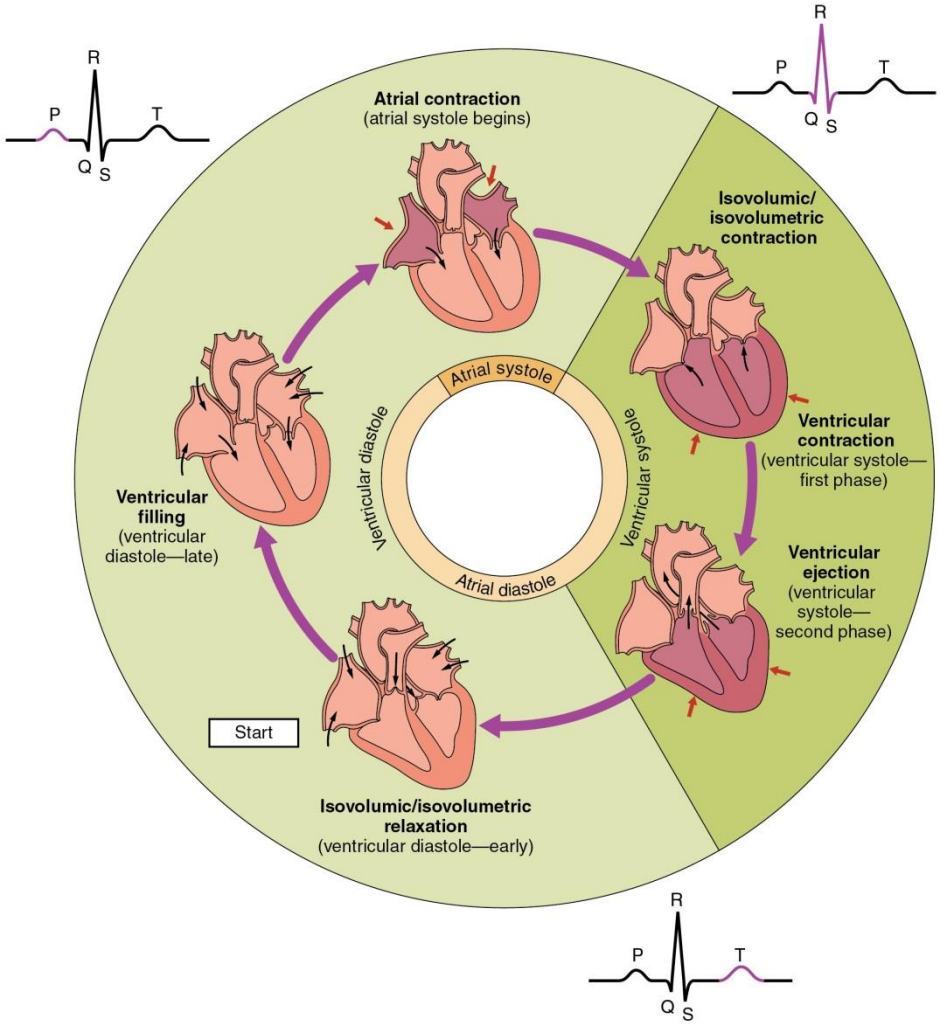

Figure 1.3: The cardiac cycle begins with atrial systole and progresses to ventricular systole, atrial diastole, and ventricular diastole, when the cycle begins again. Correlations to the ECG are highlighted (OpenStax 2013)

Although the heart is filled with blood, its walls are too thick to be supplied oxygen and nutrients by diffusion alone. Therefore, the heart has its own vasculature system. The arterial supply comes from the base of the aorta and consists of the right and left coronary arteries. The cardiac veins drain the de-oxygenated blood into the right atrium so it can be propelled into the lungs for re-oxygenation.

Due to its location in the body the porcine heart has a typical “valentine heart” shape. It weighs 350 gr in average and beats about 70 times per minute while resting (Detweiler & Erickson 2004). The heart is the most hard-working muscle in the body as it contracts over 100.000 times per day in an adult, propelling 8.000 litres of blood throughout the body (Marieb & Hoehn 2013; Weinhaus & Roberts 2009).

1.2 Blood circulation in the heart

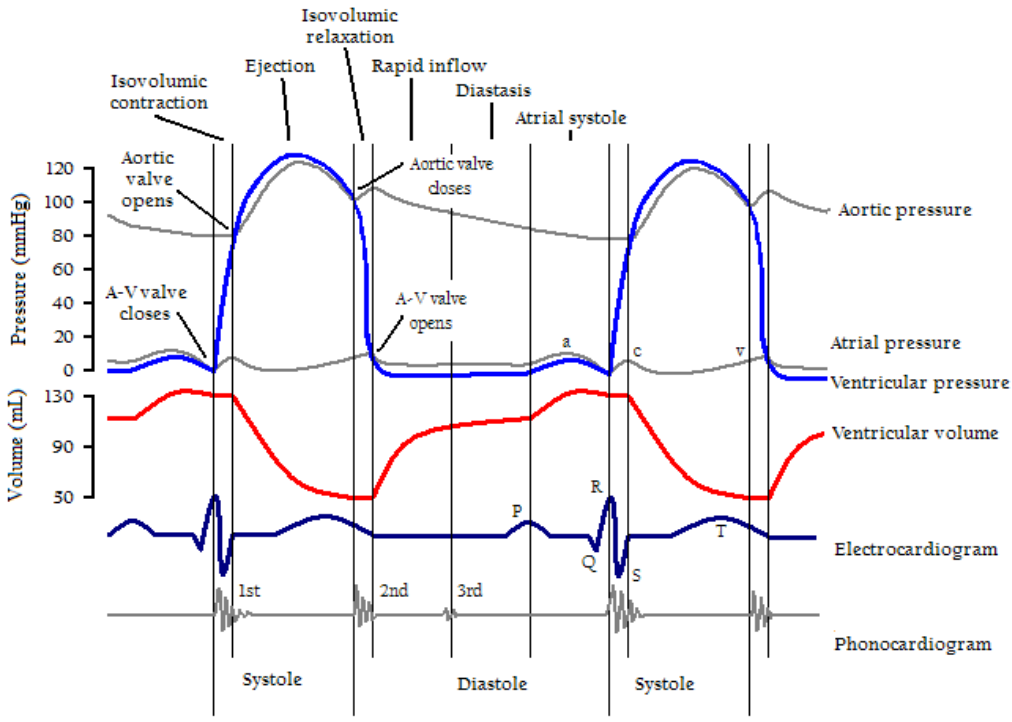

Figure 1.4: Pressure – volume relationship in the cardiac cycle. The x-axis represents the time and the y-axis the pressure and volume (www.wikipedia.org, Cardiac Cycle)

The cardiac cycle, as shown in Figure 1.3, begins with the contraction of the atria and ends with the relaxation of the ventricles. Systole is the period of time when the heart contracts and diastole when it relaxes. As with all fluids, the movement of blood is dictated by pressure gradients, meaning that it flows from regions with higher pressure to regions with lower pressure.

When the heart relaxes, de-oxygenated blood returning from the body enters the heart's right atrium through the vena cava and the coronary sinus. The oxygenated blood returning from the lungs flows into the left atrium through the pulmonary veins. As the atria are filled with blood their pressure rises. An electrical signal starts the heartbeat and causes the atria to contract, heightening their pressure ever more so the blood is pumped to the right ventricle through the tricuspid valve and to the left ventricle through the mitral valve. During ventricular systole, the pressure in the ventricles rises and the blood is pumped into the pulmonary artery and the aorta.

Contraction of the atria causes depolarization, represented by the P wave on the ECG. Ventricles are filled with approximately 70 - 80 % of their capacity during diastole and the remaining 20 -30 % is due to the atrial contraction. Ventricular systole follows the depolarization of the ventricles and is represented by the QRS complex in the ECG. The final T wave in the ECG represents the ventricular relaxation. This whole process lasts about 0.8 sec (Figure 1.4).

1.3 Function and anatomy of blood vessels

The three major categories of blood vessels are the arteries, the veins and the capillaries. The arteries carry blood away from the heart to the rest of the body while the veins carry blood toward the heart. Of all the blood vessels, only the capillaries have direct contact with the tissue cells where exchanges between the cells and the blood happens.

The walls of the blood vessels consist of three distinct layers that cover hollow passageway where blood flows, the lumen (Figure 1.5). The innermost layer is called the tunica intima and is

composed of connective and epithelial tissue layers. Lining the tunic intima is the simple squamous endothelium layer which covers all the vasculature and provides a slick surface that minimises friction as the blood flows through the lumen.

The middle and thickest layer of the vessel wall is called the tunica media which mainly consists of smooth muscle cells supported by elastin fibres which are arranged in circular sheets. In addition there is a network of collagenous fibres that binds the tunica media to the inner and outer tunics. In larger arteries there is a layer that separates the tunica media from the outer tunica externa called the external elastic membrane. Such a layer is not seen in veins and smaller arteries. The role of the tunica media is important as it regulates the pressure and circulation of blood flow. Consequently, because the blood pressure is greater in arteries than in veins, the arterial tunica intima is much thicker.

Finally, the outermost layer of the blood vessel wall is the tunica externa or tunica adventitia. It is a connective tissue sheet composed primarily of loosely woven collagen fibres. Its outer layers are not easily distinguishable as they merge with the surrounding connective tissue outside the vessel, binding the vessel into position. In larger veins this layer is thicker than the tunica media in some larger arteries. In larger vessels the tunica externa contains a system of small blood vessels, the vasa vasorum, that provide nutrients to the external layers of the blood vessel wall.

Arteries can be divided into three categories: elastic (e.g. aorta, carotids and pulmonary arterial vessels), muscular (e.g. coronary, femoral and cerebral arteries) and arterioles. Elastic arteries are closest to the heart and have a high percentage of elastin fibres in all of their tunics. Vessels larger than 10mm in diameter are usually elastic. The high percentage of elastin fibres allow

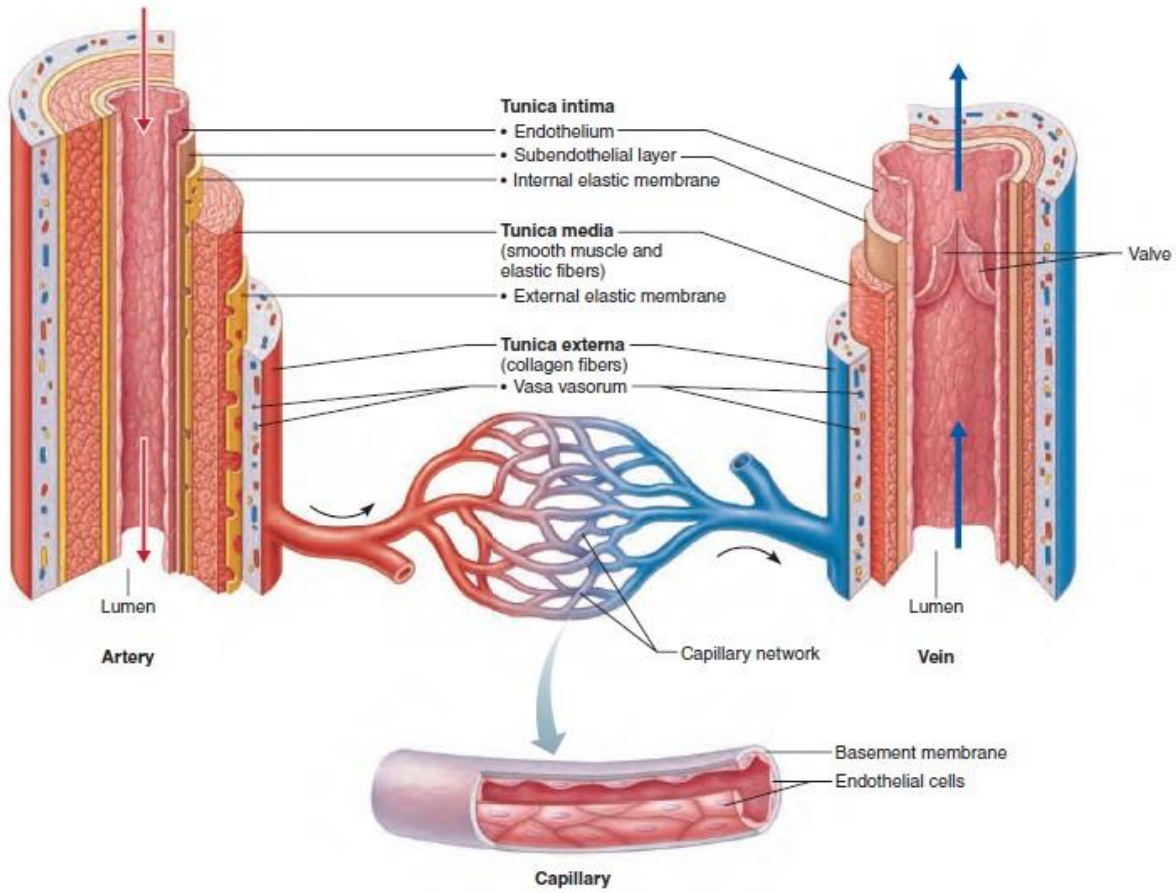

Figure 1.5: Comparison of wall structure of arteries, veins, and capillaries. Note that the tunica media is thicker than the tunica externa in arteries and that the opposite is true in veins (Marieb & Hoehn 2013).

them to withstand the high blood pressure bursts and return to their original state after the surge has passed. The elastic recoil helps to maintain the pressure gradient that drives the blood through the systemic circuit. The elastic arteries are also called conductive arteries because they help conduct the large volumes of blood they receive to the smaller branches.

Distally to the heart, where the blood pressure has dropped, the elastic arteries give way to the muscular arteries. Their size ranges between 0.1 mm and 10 mm. Muscular arteries have less elastic fibres and more smooth muscle cells in the tunica media. For this reason, they play a leading role in vasoconstriction. Because they help distribute the blood to the arteriole network, they are also called distributing arteries.

The arterioles are very small arteries that lead to capillaries. Their lumen diameter is 30 µm or less and helps slow down the blood before it reaches the capillaries. For that reason, they are also called resistance vessels (Marieb & Hoehn 2013; OpenStax 2013).

1.4 Anatomy of the aorta

The aorta is the largest artery in the body. It is about 2.5 cm in internal diameter and its wall is about 2 mm thick, although its size decreases slightly as it runs to its terminus. At the base of the aorta is the aortic valve which prevents backflow during diastole and opposite each aortic valve cusp is an aortic sinus, which contains baroreceptors that regulate reflexes of blood pressure.

The parts of the aorta are named according to their location and shape. From the base of the aorta the right and left coronary arteries emerge. Just after exiting the heart the ascending aorta moves superiorly and to the posterior of the pulmonary trunk for approximately 5 cm where it arcs to the left, forming the aortic arch. In the aortic arch the three branches that arise are the branchiocephalic trunk, the left common carotid artery the left subclavian artery. These vessels supply the head, neck, upper limbs and part of the thorax wall with blood. Beyond this point, the descending aorta continues along the spine where it sends numerous arteries to the thorax wall and viscera before passing through the diaphragm though the aortic hiatus. The part of the aorta above the diaphragm is the thoracic aorta and the part below the abdominal aorta. Finally, the abdominal aorta splits into the left and right common iliac arteries, which supply the pelvis and lower limbs with blood.

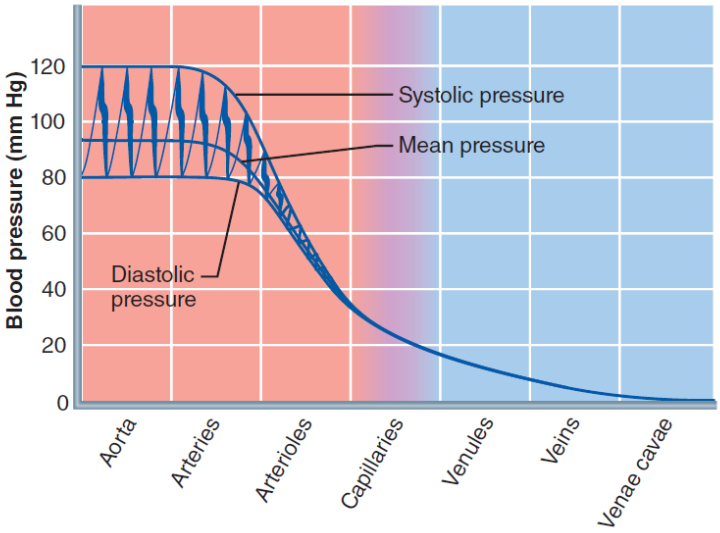

Figure 1.6: Blood pressure in various vessels of the systemic and pulmonary circulation (Marieb & Hoehn 2013).

1.5 Structure function relationship of the components of soft biological tissue

The soft tissue of our body comprises of complex fibre-reinforced composite structures. The concentration, distribution and structural arrangement of components like collagen, elastin, the hydrated matrix of proteoglycans and the topographical site and respective function in the organism strongly influence their mechanical behaviour.

1.5.1 Structure of proteins

Proteins are the basic structural material of the body and compose 10 – 30 % of the cell mass. Apart from structural components, they also play vital role in cell function. In general, their role is diverse as proteins include enzymes (biological catalysts), hemoglobin of the blood, the contractile elements of the muscles and many more. All proteins contain carbon, oxygen, hydrogen and nitrogen, while many contain sulfur as well. Structural proteins like collagen, elastin and keratin provide the extracellular matrix which provides strength, organisation and support for the cells, tissues and organs.

The building blocks of proteins are molecules called amino acids. All amino acids have a functional group called the amine group ($–NH_2$) and an organic acid group called the acid group (–COOH). The part of their molecule that differentiates them and makes them unique is the –R group. The simplest –R group is hydrogen, which forms glycine when combined with the amino acid.

Proteins are long chains of amino acids joined together by a dehydration synthesis, with the amine end of one group joining the acid group of the other. This type of bond is called peptide bond. When multiple amino acids form peptide bonds between them the resulting molecule is called protein when the number of amino acids is over 50. Most proteins are large complex molecules called macromolecules consisting of 100 to over 100.000 amino acids.

The number of amino acids that make up all the proteins is 20. Therefore, we can think the amino acids as the alphabet and the proteins as the words. Changes in the structure of molecules result in proteins with different function or completely non-functional ones. Apart from their simple linear chain structure, further levels of structural complexity include the secondary, tertiary and quaternary structures. The α – helix is the most common secondary structure and it resembles a telephone cord. This structure is a result of hydrogen bonding between different parts of the polypeptide chain. The tertiary structure is achieved when proteins with secondary structure fold up on one another to form globular molecules. When two or more polypeptide chains aggregate in a regular manner to form a complex protein that protein has quaternary structure. It is clear then that the importance of the structure of proteins cannot be overstressed.

1.5.1.1 Collagen

Collagen is the most abundant protein in mammals (~30% of total protein mass) (Ricard-Blum 2011)] and a major component of the extracellular matrix of connective tissue. Its role in human physiology is of utmost importance as it is the main load bearing element in a wide variety of soft tissues. The tropocollagen molecule consists of three polypeptide α – chains, two of the same

and one different kind coiled in a left-handed helix while the molecule itself forms a right-handed superhelix formed by these three chains. This concept is shown in Figure 1.7. There are 28 different types of collagen that have been identified (Ricard-Blum 2011). Depending on the tissue the collagen chains are different. The most common collagen type is I and it is found in any tissue.

Tropocollagen molecules form covalent bonds with each other to build collagen fibrils. The fibrils present a striated pattern with the periodic length of the striation being 640 Å in native and 680 Å in moistened fibrils (Fung 1993). The length of the molecule is 4.4 times the length of the striation period of the native fibril and consists of five segments, four of which have the same length of D and a shorter one with length 0.4D. The gap that is left between the molecules is 0.6D in length. The alignment of the molecules may seem straight in figure 7 but in reality they are bent with varying space between neighbouring molecules, the water molecules being the criterion of the degree of bending.

Their characteristics like diameter and orientation depends on their primary function and strength requirement. Depending on the species and tissue, the diameter varies from 200 Å to 400 Å. Bundles of fibrils have diameters ranging from 0.2 to 12 μm. In tendons and ligaments, collagen is oriented in parallel fibres while in other tissues it forms an intricate disordered network of fibres embedded in a gelatinous matrix of proteoglycans. In their stress free state the collagen fibres are usually found crimped. When loading is applied the crimping is reduced.

The two main types of collagen found in the aorta are types I and III and they account for 80 – 90 % of the total collagen. Types IV, V, VI and VII can be also found in smaller amount (Berillis 2013).

The types that are met in valve tissues are primarily I and III, and small portions of II and V. The normal valve contains approximately 74 % I, 24 % II and 2 % V. (Latif et al. 2005)

1.5.1.2 Elastin

Elastin like collagen is a protein which is a major component of the extracellular matrix of connective tissue. It is present as thin strands in soft tissues like skin, lung, heart valves, ligaments etc. Contrary to collagen that presents both crystalline and amorphous regions, elastin is not considered a fibrous material. It is merely thin strands of a rubbery material. Elastin constitutes quite a large proportion of the material in the walls of arteries especially those close to the heart. The elastin molecules build up a rubber like network, which can be stretched about 2.5 times its initial length. In contrast to collagen fibres, this network does not exhibit a pronounced hierarchical organization. Elastin is the most linearly elastic biosolid material known (Fung 1993) that displays very small relaxation effects and helps the tissue recover its original shape.

Table 1.1: Mechanical properties and associated biochemical data of some representative organs mainly consisting of soft connective tissues (Holzapfel 2000).

Material	Ultimate Tensile Strength [MPa]	Ultimate Tensile Strain [%]	Collagen (% dry weight)	Elastin (% dry weight)
Tendon	50 – 100	10 – 15	75 – 85	<3
Ligament	50 – 100	10 – 15	70 – 80	10 – 15
Aorta	0.3 - 0.8	50 – 100	25 – 35	40 – 50
Skin	1 – 20	30 – 70	60 – 80	5 – 10
Articular Cartilage	9 – 40	60 – 120	40 – 70	-

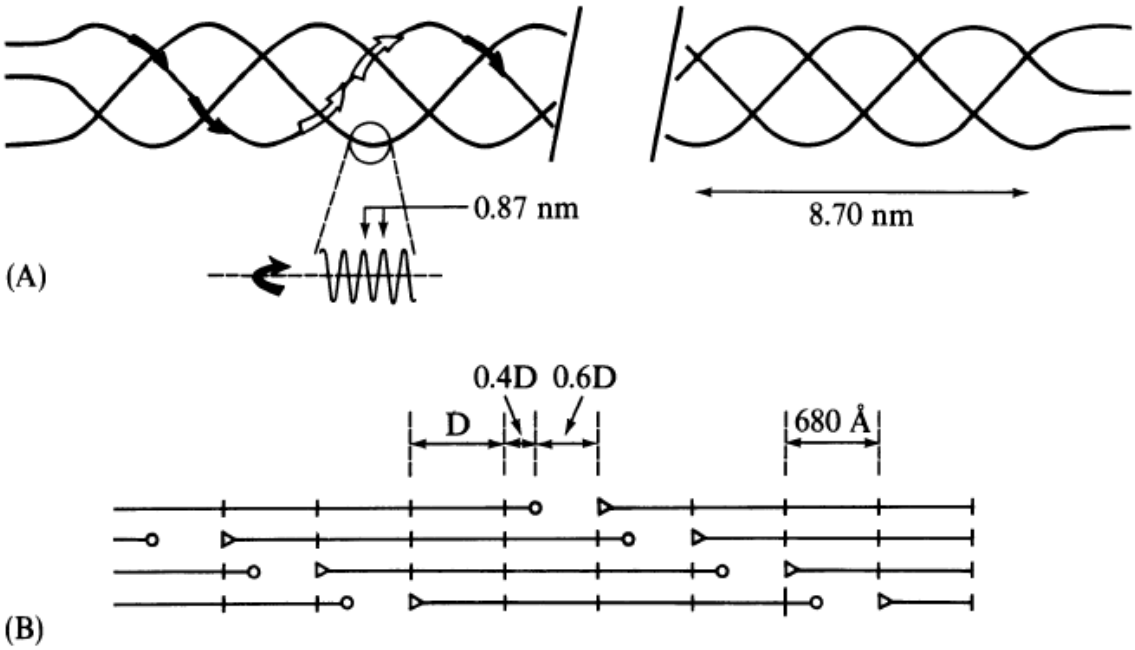

Figure 1.7: Current concept of the collagen molecule and fibril. (A) Sketch showing three chains of amino acid residues constituting left-handed helices with a pitch of 0.87 nm wound together into a right0handed superhelix with a pitch of 8.7 nm. (B) The concept of quarter-stagger of the molecules combined with overlaps and gaps. The length of the molecule is 4.4 times that of a period (D).

1.5.2 Structure of Polysaccharides

Through dehydration one monosaccharide can be combined with another to create a disaccharide. When this process is repeated the result is complex molecules called polysaccharides. Polysaccharides are highly viscous substances with low compressibility, which makes them ideal for lubrication purposes.

1.5.2.1 Glycosaminoglycans

The most abundant unbranched heteropolysaccharides in the body are the glycosaminoglycans (GAGs). The disaccharide unit that is being repeated can contain either of two modified sugars *N*-acetylgalactosamine (GalNAc) or *N*-acetylglucosamine (GlcNAc) and a uronic acid such as glucuronate or iduronate. Their negative charge along with their shape makes the solution highly viscous. They are located in the surface of cells or in the extracellular matrix where they provide passageways between the cells and integrity. The high viscosity they provide along with the low compressibility makes them ideal for lubricating fluid in the joints. Heparin and dermatan sulfate are GAGs that are found in blood vessels (King 2014).

1.5.2.2 Proteoglycans

Most of the GAGs are linked perpendicularly to core proteins forming proteoglycans or mucopolysaccharides. The linking involves a trisaccharide composed of two galactose residues and a xylose residue (GAG-GalGalXyl-O-CH2-protein). Proteoglycans provide lubrication in the cartilage of joints or between collagen and elastin (King 2014).

1.5.2.3 Ground Substance

The ground substance, also called the extrafibrillar matrix, is an amorphous gelatinous substance that surrounds the cells and the connective tissue fibres. Cells of connective tissues are mainly fibroblasts and along with the collagen, elastin and reticulin they are integrated in the ground substance. In dense connective tissues the amount of ground substance is less than in loose connective tissues. The composition of ground substance varies with the tissue, but it contains glycosaminoglycans and tissue fluid. The movement of water through the ground substance and its binding to the collagen fibres is of great importance to the mechanical properties of the tissue.

1.6 Stress-strain relationship of soft tissues under uniaxial elongation

Soft tissues exhibit anisotropic mechanical behaviour owing to a preferred fibre alignment. Because of their composition, it is clear in a microscope that they are non-homogenous materials. In addition, they display viscoelastic behaviour (relaxation and/or creep), which has been associated with the shear interaction of collagen with the matrix of proteoglycans due to the matrix's viscous lubrication between collagen fibres.

The simplest experiment that can be done on a blood vessel is the uniaxial loading test. A vessel or a strip of it is loaded lengthwise while the lateral sides are left free and the force – elongation relationship is recorded. From this recording the stress – strain relationship of the tissue under uniaxial loading can be computed. An important issue in this kind of testing is the identification of the zero-stress state of the specimen. In soft biological tissues the determination of this state is difficult because the tissues are soft and difficult to handle. It is also known that in their natural state the tissues are not stress-free. If an artery is cut it will shrink away from the cut, a tendon retracts away and the lung tissue is in tension at all times. Thus, experimental results are better presented when they refer to a well-defined reference-state which can be arbitrarily chosen as long as it definitive and physiological (Fung 1993).

The tensile stress-strain behaviour of soft biological tissue is shown in Figure 1.8. The deformation behaviour can be studied in three phases I,II and III.

Phase I: In their load free configuration the collagen fibres are relaxed and appear crimped and wavy. In phase I, or elastin phase, the tissue behaves like an isotropic rubber sheet, and the elastin fibres are mainly responsible for the stretching mechanism. The stress-strain relation is approximately linear and the elastic modulus is low.

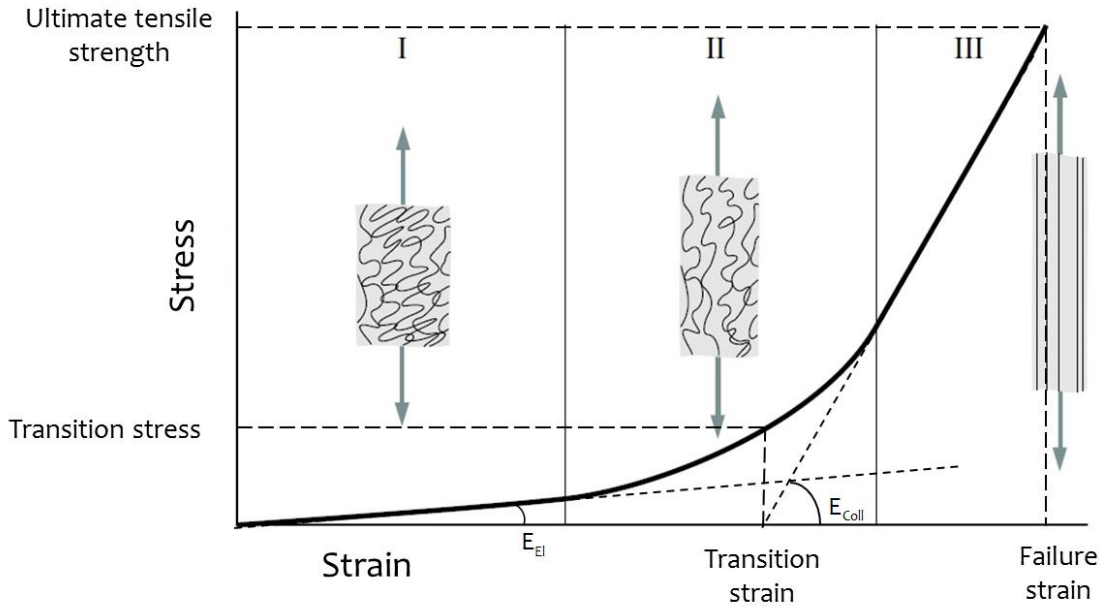

Figure 1.8: Typical stress - strain graph of soft biological tissue showing also the configuration of collagen fibres in the tissue during each phase. (Holzapfel 2000)

Phase II: As the loading is increasing the collagen fibres start to align to the load's direction and bear loads. The crimped collagen fibres gradually elongate and interact with the hydrated matrix.
Phase III: At high tensile stresses the crimps disappear and the fibres become straighter and aligned in the direction of the loading (collagen phase). The straightened fibres resist the load which results in high stiffness and the stress-strain behaviour becomes linear again. Beyond phase III the breaking of collagen fibres ensues at the ultimate tensile strength (UTS).

The parameters that can be extracted from this kind of graph are the collagen phase elastic modulus, the elastin phase elastic modulus, the UTS and failure strain and the strain value that corresponds to the point where the extension of the collagen phase slope cuts the strain axis. It is called transition strain and it is an artificial parameter that is used in the process of preconditioning.

1.6.1 Preconditioning and viscoelasticity of soft biological tissues

Soft biological tissue exhibits viscoelastic properties. If the specimen is subjected to cycling loading and unloading a hysteresis loop can be observed in the stress – strain graph. This loop decreases with each cycle and after a number of cycles it falls into a steady state (Figure 1.9,Figure 1.10A). The process of cyclic loading until this steady state has been reached is called preconditioning. The hysteresis loop has been shown to be independent of the strain rate, with this sensitivity holding within at least a 10^3-fold change in strain rate. During preconditioning the internal structure of the tissue is reorganised until it reaches a steady state and the stress – strain results are predictable, well defined and repeatable (Fung 1993). The limit of the deformation that is imposed cyclically during preconditioning is chosen so that the elongation is within the physiological range in which the tissue normally functions. A change in the limit will cause changes in the internal structure again and the tissue has to be preconditioned anew. For blood vessels, when blood flow through the vasa vasorum

is maintained in the vessel wall, preconditioning is achieved quickly with only a few cycles. However if the supply from vasa vasorum is cut preconditioning may take many cycles.

Other viscoelastic properties of soft tissues include stress relaxation and creep (Figure 1.10B,C). If suddenly a stress σ_0 is imposed to a tissue while its length stays the same, the stress decreases over time until it reaches asymptomatically a certain value σ_1. This phenomenon is called stress relaxation. Similarly, if a tissue is strained to a strain ε_0 while the stress is held constant, the tissue deforms until it reaches asymptomatically a strain value ε_1.

All biological tissues are characterized by non-linear stress – strain relationship, hysteresis loop, creep, relaxation and preconditioning although the degree is different among the tissues. The hysteresis loop and relaxation for elastin and collagen are quite small, while for smooth muscle fibers are very large (Fung 1993).

1.7 Kinematics

1.7.1 Measures of stress and strain

An important distinction between the measures used for the calculation of stress and strain is engineering, nominal, or Piola-Kirchhoff stress and strain versus true, or Cauchy, stress and stress. Stress is always defined as [force] / [area] but the difference lies in the assumption of the status of the cross sectional area. Engineering stress and strain incorporate the undeformed cross sectional are A_0.

$$\boldsymbol{\sigma_E = \frac{F}{A_0}}, \qquad \boldsymbol{\varepsilon_E = \frac{\Delta L}{L_0}} \tag{1.1}$$

True stress and strain account for the changes in the cross sectional area during the material's deformation. Thus the true stress incorporates the instantaneous deformed area A (Equation (1.2)).

$$\boldsymbol{\sigma_T = \frac{F}{A}} \tag{1.2}$$

We can relate the engineering stress with the true stress if we assume that the volume of the specimen remains the same (Equation (1.3)).

$$\boldsymbol{A \cdot L = A_0 \cdot L_0 \Rightarrow A = A_0 \frac{L_0}{L}} \tag{1.3}$$

Combining equations (1.2) and (1.3)

$$\boldsymbol{\sigma_T = \frac{F}{A} = \frac{F}{A_0} \cdot \frac{L}{L_0} = \sigma_E(1 + \varepsilon_E)}. \tag{1.4}$$

Likewise, the true strain can be related to the engineering strain. The instantaneous strain is

$$\boldsymbol{d\varepsilon = \frac{dL}{L}} \tag{1.5}$$

With integration over the specimen length we get

$$\boldsymbol{\varepsilon_T} = \int \boldsymbol{d\varepsilon} = \int_{L_0}^{L_f} \frac{\boldsymbol{dL}}{\boldsymbol{L}} = \boldsymbol{ln}\frac{\boldsymbol{L_f}}{\boldsymbol{L_0}} \tag{1.6}$$

where L_f is the final length of the specimen. Therefore, the true strain is

$$\boldsymbol{\varepsilon_T} = \boldsymbol{ln}\frac{\boldsymbol{L_f}}{\boldsymbol{L_0}} = \boldsymbol{ln}\frac{\boldsymbol{L_0 + \Delta L}}{\boldsymbol{L_0}} = \boldsymbol{ln}(\boldsymbol{1 + \varepsilon_E}) \tag{1.7}$$

For small deformations, the true stress and strain is almost identical to the engineering stress and strain. However, for large deformations the cross sectional area decreases significantly and the true stress can be much larger than the engineering.

1.7.2 Large deformation kinematics and strain energy potential

The deformation gradient is used to describe the movement of objects that go through large deformations. If (X_1, X_2, X_3) is any particle in the original configuration of the object and (x_1, x_2, x_3) is the same particle in the deformed configuration then the deformation vector **u** is defined as such

$$\mathbf{u_i} = \mathbf{x_i} - \boldsymbol{X_i} \tag{1.8}$$

The displacement gradients can be written as

$$\frac{\boldsymbol{\partial u_1}}{\boldsymbol{\partial X_1}} = \frac{\boldsymbol{\partial x_1}}{\boldsymbol{\partial X_1}} - \boldsymbol{1}, \qquad \frac{\boldsymbol{\partial u_2}}{\boldsymbol{\partial X_2}} = \frac{\boldsymbol{\partial x_2}}{\boldsymbol{\partial X_2}} - \boldsymbol{1}, \qquad \frac{\boldsymbol{\partial u_3}}{\boldsymbol{\partial X_3}} = \frac{\boldsymbol{\partial x_3}}{\boldsymbol{\partial X_3}} - \boldsymbol{1} \tag{1.9}$$

and so forth. These nine terms can be written in a matrix form

$$\boldsymbol{H} = \mathbf{F} - \mathbf{I} \Leftrightarrow \mathbf{F} = \mathbf{I} + \mathbf{H} \tag{1.10}$$

where **H** is the displacement gradient, **F** the deformation gradient and **I** the identity matrix. The deformation gradient $\boldsymbol{F} \equiv \frac{\partial \boldsymbol{x}}{\partial \boldsymbol{X}}$ can be written as

$$[F] = \begin{bmatrix} \frac{\partial x_1}{\partial X_1} & \frac{\partial x_1}{\partial X_2} & \frac{\partial x_1}{\partial X_3} \\ \frac{\partial x_2}{\partial X_1} & \frac{\partial x_2}{\partial X_2} & \frac{\partial x_2}{\partial X_3} \\ \frac{\partial x_3}{\partial X_1} & \frac{\partial x_3}{\partial X_2} & \frac{\partial x_3}{\partial X_3} \end{bmatrix} \tag{1.11}$$

The strain tensor introduced by Green and St.-Venant is called Green's strain tensor and is defined as

$$\boldsymbol{E} = \frac{\boldsymbol{1}}{\boldsymbol{2}}(\boldsymbol{F^T F} - \boldsymbol{I}) = \frac{\boldsymbol{1}}{\boldsymbol{2}}(\boldsymbol{C} - \boldsymbol{I}) \tag{1.12}$$

where $\boldsymbol{C} = \boldsymbol{F}^{\boldsymbol{T}}\boldsymbol{F}$ is the right Cauchy – Green deformation tensor. The relation between the Cauchy stress tensor and the first Piola – Kirchhof stress tensor, $\boldsymbol{\sigma}$ and $\boldsymbol{\tau}$ respectively is

$$\boldsymbol{\sigma} = \frac{\mathbf{1}}{\boldsymbol{detF}}\boldsymbol{F} \cdot \boldsymbol{\tau} \Leftrightarrow \boldsymbol{\tau} = \boldsymbol{detF} \cdot \boldsymbol{F}^{-\mathbf{1}}\boldsymbol{\sigma} \tag{1.13}$$

In uniaxial test the first Piola – Kirchhoff stress is often preferred due to the fact that the only parameter used for the calculation is the original cross sectional area A_0. The second Piola – Kirchhoff stress **S**, which is usually present in constitutive equations, is related to the Cauchy and first Piola – Kirchhoff stresses

$$\boldsymbol{\sigma} = \frac{\mathbf{1}}{\boldsymbol{detF}}\boldsymbol{FSF}^{\boldsymbol{T}} \quad , \quad \boldsymbol{\tau} = \boldsymbol{SF}^{\boldsymbol{T}} \tag{1.14}$$

Soft biological tissues are often modelled as hyperelastic materials. Hyperelastic materials are described in terms of a "strain energy potential," which defines the strain energy stored in the material per unit of reference volume (volume in the initial configuration) as a function of the deformation at that point in the material. The invariant – based formulation is described in the next paragraph.

Writing the current position of a material point as $\boldsymbol{x}$ and the reference position of the same point as $\boldsymbol{X}$, the deformation gradient is

$$\boldsymbol{F} \equiv \frac{\boldsymbol{\partial x}}{\boldsymbol{\partial X}} \tag{1.15}$$

then J is the total volume change at the point

$$\boldsymbol{J} \equiv \boldsymbol{det}(\boldsymbol{F}). \tag{1.16}$$

For simplicity we define

$$\overline{\boldsymbol{F}} \equiv \boldsymbol{J}^{-\frac{\mathbf{1}}{\mathbf{3}}}\boldsymbol{F} \tag{1.17}$$

as the deformation gradient with the volume change eliminated.

We then introduce the deviatoric stretch matrix of $\overline{\boldsymbol{F}}$, or the left Cauchy – Green deformation tensor, as

$$\overline{\boldsymbol{B}} \equiv \overline{\boldsymbol{F}} \cdot \overline{\boldsymbol{F}}^{\boldsymbol{T}} \tag{1.18}$$

so we can introduce the first strain invariant as

$$\overline{\boldsymbol{I}}_{\mathbf{1}} \equiv \boldsymbol{tr}(\overline{\boldsymbol{B}}) = \boldsymbol{I} : \overline{\boldsymbol{B}} \tag{1.19}$$

where **I** is the identity matrix, and the second strain invariant as

$$\bar{I}_2 \equiv \frac{1}{2}\left(\bar{I}_1^2 - tr(\bar{\boldsymbol{B}})\right) = \frac{1}{2}\left(\bar{I}_1^2 - \boldsymbol{I} : \bar{\boldsymbol{B}}\right). \tag{1.20}$$

The variations of $\bar{\boldsymbol{B}}$, $\bar{\boldsymbol{B}} \cdot \bar{\boldsymbol{B}}$, $\bar{I}_1$, $\bar{I}_2$ and J will be required during the remainder of the development. We first define some variations of basic kinematic quantities that will be needed to write these results.

The gradient of the displacement variation with respect to current position is written as

$$\delta \boldsymbol{L} \equiv \frac{\partial \delta \boldsymbol{u}}{\partial \boldsymbol{x}}. \tag{1.21}$$

The virtual rate of deformation is the symmetric part of $\delta\mathbf{L}$:

$$\delta \boldsymbol{D} \equiv \frac{1}{2}(\delta\mathbf{L} + \delta\mathbf{L}^T) \tag{1.22}$$

which we decompose into the virtual rate of change of volume per current volume, the virtual volumetric strain rate,

$$\delta \boldsymbol{\varepsilon}^{vol} \equiv \boldsymbol{I} : \delta \boldsymbol{D} \tag{1.23}$$

and the deviatoric strain rate,

$$\delta \boldsymbol{\varepsilon} \equiv \delta \boldsymbol{D} - \frac{1}{3}\delta \boldsymbol{\varepsilon}^{vol} \boldsymbol{I} \tag{1.24}$$

the virtual rate of spin of the material is the antisymmetric part of $\delta\mathbf{L}$

$$\delta \boldsymbol{W} \equiv \frac{1}{2}(\delta\mathbf{L} - \delta\mathbf{L}^T) \tag{1.25}$$

The variations of $\bar{\boldsymbol{B}}$, $\bar{\boldsymbol{B}} \cdot \bar{\boldsymbol{B}}$, $\bar{I}_1$, $\bar{I}_2$ and J are obtained directly from their definitions above in terms of these quantities as

$$\delta \bar{\boldsymbol{B}} = \delta \boldsymbol{e} \cdot \bar{\boldsymbol{B}} + \bar{\boldsymbol{B}} \cdot \delta \boldsymbol{e} + \delta \boldsymbol{W} \cdot \bar{\boldsymbol{B}} - \bar{\boldsymbol{B}} \cdot \delta \boldsymbol{W} = \boldsymbol{H}_1 : \delta \boldsymbol{e} + \delta \boldsymbol{W} \cdot \bar{\boldsymbol{B}} - \bar{\boldsymbol{B}} \cdot \delta \boldsymbol{W} \tag{1.26}$$

where

$$\begin{gathered} (H_1)_{ijkl} \equiv \frac{1}{2}\left(\delta_{ik}\bar{B}_{jl} + \bar{B}_{ik}\delta_{jl} + \delta_{il}\bar{B}_{jk} + \bar{B}_{il}\delta_{jk}\right); \\ \delta(\bar{\boldsymbol{B}} \cdot \bar{\boldsymbol{B}}) = \delta \boldsymbol{e} \cdot \bar{\boldsymbol{B}} \cdot \bar{\boldsymbol{B}} + \bar{\boldsymbol{B}} \cdot \bar{\boldsymbol{B}} \cdot \delta \boldsymbol{e} + 2\bar{\boldsymbol{B}} \cdot \delta \boldsymbol{e} \cdot \bar{\boldsymbol{B}} + \delta \boldsymbol{W} \cdot \bar{\boldsymbol{B}} \cdot \bar{\boldsymbol{B}} - \bar{\boldsymbol{B}} \cdot \bar{\boldsymbol{B}} \cdot \delta \boldsymbol{W} \Rightarrow \\ \delta(\bar{\boldsymbol{B}} \cdot \bar{\boldsymbol{B}}) = \boldsymbol{H}_2 : \delta \boldsymbol{e} + \delta \boldsymbol{W} \cdot \bar{\boldsymbol{B}} \cdot \bar{\boldsymbol{B}} - \bar{\boldsymbol{B}} \cdot \bar{\boldsymbol{B}} \cdot \delta \boldsymbol{W} \end{gathered} \tag{1.27}$$

where

$$(\boldsymbol{H}_2)_{ijkl} \equiv \frac{1}{2}\left(\delta_{ik}\bar{\boldsymbol{B}}_{jp}\bar{\boldsymbol{B}}_{pl} + \bar{\boldsymbol{B}}_{ip}\bar{\boldsymbol{B}}_{pk}\delta_{jl} + \delta_{il}\bar{\boldsymbol{B}}_{jp}\bar{\boldsymbol{B}}_{pk} + \bar{\boldsymbol{B}}_{ip}\bar{\boldsymbol{B}}_{pl}\delta_{jk}\right) + \bar{\boldsymbol{B}}_{ik}\bar{\boldsymbol{B}}_{jl} + \bar{\boldsymbol{B}}_{il}\bar{\boldsymbol{B}}_{jk}; \tag{1.28}$$

$$\delta \bar{I}_1 = 2\bar{\boldsymbol{B}} : \delta \boldsymbol{e}\,; \tag{1.29}$$

$$\delta \bar{I}_2 = 2(\bar{I}_1\bar{\boldsymbol{B}} - \bar{\boldsymbol{B}} \cdot \bar{\boldsymbol{B}}) : \delta \boldsymbol{e}\,; \tag{1.30}$$

$$\boldsymbol{\delta J = J\delta\varepsilon^{vol}}. \tag{1.31}$$

The true stress components are defined from the strain energy potential as follows. From the virtual work principle the internal energy variation is

$$\boldsymbol{\delta W_I = \int_V \sigma : \delta D\, dV = \int_{V^o} J\sigma : \delta D\, dV^o} \tag{1.32}$$

where $\boldsymbol{\sigma}$ is the true stress, V is the current volume and V^o is the reference volume.

We decompose the stress into the equivalent pressure stress

$$\boldsymbol{p \equiv -\frac{1}{3} I : \sigma} \tag{1.33}$$

and the deviatoric stress

$$\boldsymbol{S \equiv \sigma + pI} \tag{1.34}$$

so that the internal energy variation can be written

$$\boldsymbol{\delta W_I = \int_{V^o} J\left(S : \delta e - p\delta\varepsilon^{vol}\right) dV^o}. \tag{1.35}$$

For isotropic, compressible materials the strain energy U, is a function of $\bar{I}_1$, $\bar{I}_2$ and J:

$$\boldsymbol{U = U(\bar{I}_1, \bar{I}_2, J)} \tag{1.36}$$

so that

$$\boldsymbol{\delta U = \frac{\partial U}{\partial \bar{I}_1}\delta\bar{I}_1 + \frac{\partial U}{\partial \bar{I}_2}\delta\bar{I}_2 + \frac{\partial U}{\partial J}\delta J} \tag{1.37}$$

Hence, using equations (1.29) – (1.31)

$$\boldsymbol{\delta U = 2\left[\left(\frac{\partial U}{\partial \bar{I}_1} + \bar{I}_1\frac{\partial U}{\partial \bar{I}_2}\right)\bar{B} - \frac{\partial U}{\partial \bar{I}_2}\bar{B}\cdot\bar{B}\right] : \delta e + J\frac{\partial U}{\partial J}\delta\varepsilon^{vol}}. \tag{1.38}$$

Since the variation of the strain energy potential is, by definition, the internal virtual work per reference volume δW_I, we have

$$\boldsymbol{W_I = \int_{V^o} J\left(S : \delta e - p\delta\varepsilon^{vol}\right) dV^o = \int_{V^o} \delta U dV^o} \tag{1.39}$$

When the material is fully incompressible, U is a function of the first and second strain invariants $\overline{I_1}$, $\overline{I_2}$ only, and we write the internal energy in the augmented form,

$$\boldsymbol{W_I^A} = \int_{V^o} [\boldsymbol{U} - \hat{\boldsymbol{p}}(\boldsymbol{J} - \boldsymbol{1})]\boldsymbol{dV^o} \tag{1.40}$$

Where $\hat{p}$ is a Lagrange multiplier introduced to impose the constraint J – 1 = 0 in such a way that the variation of W_I^A can e taken with respect to all kinematic variables, thus giving

$$\boldsymbol{W_I^A} = \int_{V^o} \left(\boldsymbol{JS} : \boldsymbol{\delta e} - \boldsymbol{J\hat{p}\delta\varepsilon^{vol}} - (\boldsymbol{J} - \boldsymbol{1})\boldsymbol{\delta\hat{p}}\right)\boldsymbol{dV^o} = \int_{V^o} \boldsymbol{\delta U dV^o} \tag{1.41}$$

The Lagrange multiplier $\hat{p}$ is assumed to be constant in most first – order elements and to vary linearly with respect to position in second – order elements. The differentiation of the strain energy functions W with respect to the elastic part of the Green strain tensor gives the second Piola – Kirchhoff stresses.

1.8 Constitutive equations

The constitutive equation of a material describes the relationship between the stress and the strain and can only be determined through experiments. The description of a physical property must be independent of the system of coordinates according to which various quantities are measured. Thus, the constitutive equations must be a tensor equation. Hooke's law is the idealised equation which for certain limits of temperature, strain and strain rate can describe a wide variety of engineering materials. Hooke's law states that the stress tensor is linearly proportional to the strain tensor:

$$\boldsymbol{\sigma_{ij}} = \boldsymbol{C_{ijkl}\varepsilon_{kl}} \tag{1.42}$$

Where σ_{ij} is the stress tensor, C_{ijkl} is the tensor of elastic moduli which are independent of the stress

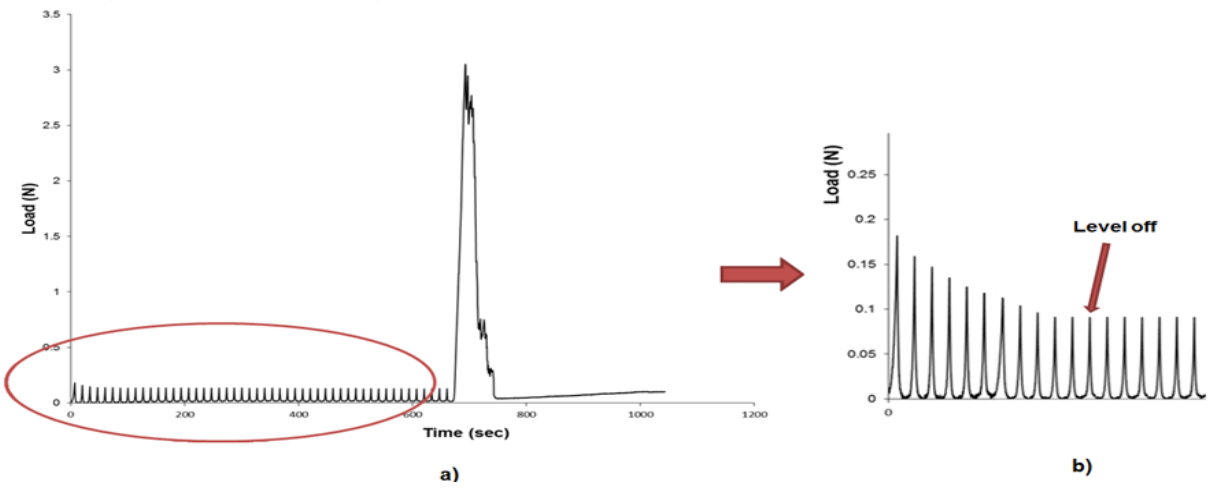

Figure 1.9: Typical load – time relationship of soft biological tissue during preconditioning (a). The red circle indicates the area of the graph zoomed in the picture (b) where the leveling off is visible after a number of cycles.

and strain and ε_{kl} is the strain tensor. Assumptions about the material (e.g. isotropic, orthotropic) can reduce the number of elastic constants required to describe the material. For the case of uniaxial deformation of an ideal elastic isotropic material Hooke's law is simplified in the form

$$\boldsymbol{\sigma} = \boldsymbol{E\varepsilon} \tag{1.43}$$

where σ is the stress, E is the Young's modulus and ε the strain. However, most biological materials cannot be described with so simple constitutive equations.

There are several shortcomings of Hooke's law when it comes to describing biomaterials. Hooke's law does not account for the time history of the material and loading rate. In addition, the hookean relation of stress and strain is only valid for small deformations. For large deformations a different constitutive theory must be formulated in which the stress and strain are defined more generally. Finally, the effects of stress and strain are reversible, meaning that the removal of the stress will cause the deformation to disappear.

On the other hand, biomaterials exhibit non-linear stress – strain relationship in general and the linearity applies only for very small strains. Moreover, the fact that they are anisotropic requires a generalisation of Hooke's law. Finally, the stress and strain depend not only on the strain rate at that time but also on the strain history. Stress relaxation, creep, hysteresis and dependence of the elastic moduli on the strain rate are the manifestation of this dependence. Thus these materials are described as viscoelastic, which means that they are in between of elastic solids and viscous fluids (Fung 1993).

For the study of the elasticity of materials that are capable of finite deformation a strain energy function is postulated. The strain energy function relates stress to strain in a hyperelastic material, which arises from changes in internal energy during loading. The 2nd Piola-Kirchhoff stresses are related to the partial derivative of the strain energy function with respect to the elastic part of the Green strain tensor. The function's determination is an inverse problem. A form of it is assumed and then based and values of stress and strain from experimental data the material properties that agree both with the theoretical and experimental data are determined. This procedure involves non-linear least square fit using algorithms like the Marquardt – Levenberg or Trust – Region.

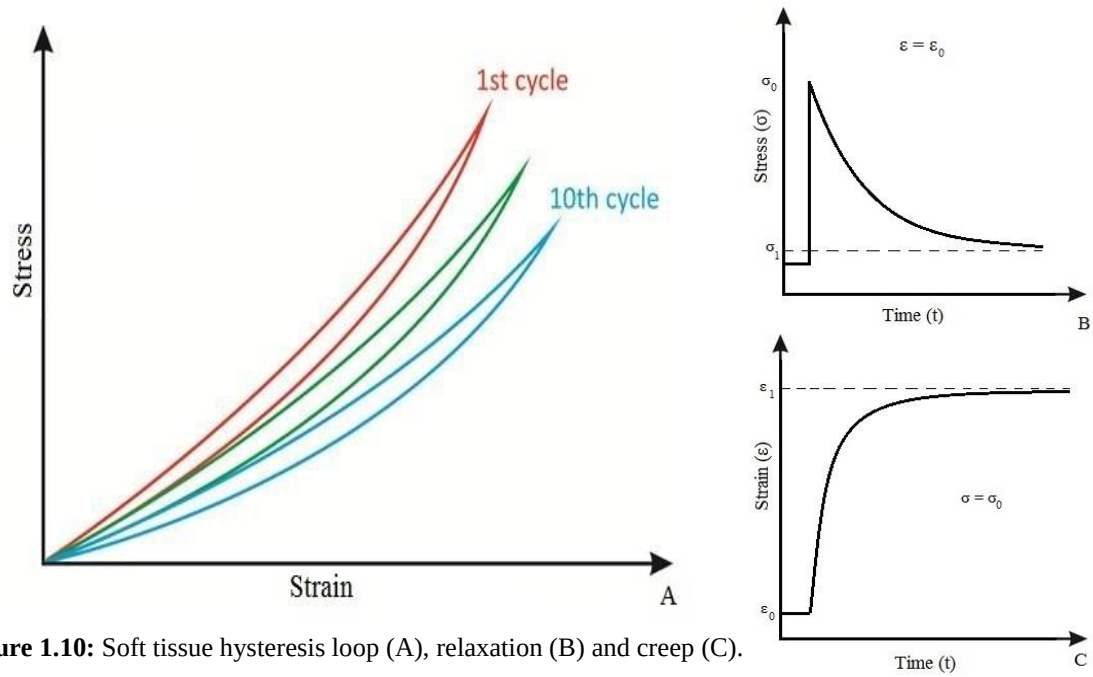

Figure 1.10: Soft tissue hysteresis loop (A), relaxation (B) and creep (C).

1.9 Biomechanical testing of aorta and the effect of preconditioning

The investigation of the mechanical properties of soft biological tissues is a difficult task. Biological tissues are inhomogeneous, anisotropic, and have spatially varying microstructure. Limitations include difficulty in handling, identification of the zero stress state and preservation of the near-physiological condition and limited availability. In addition, *in vitro* with *in vivo* measurements are difficult to correlate. Therefore, these issues have to be handled with special equipment and protocols.

Mechanical properties of arterial walls are of interest because they influence arterial biology and the development and progress of arterial diseases via effects on blood flow and arterial mass transport. In addition, stresses and strains developed in arterial walls are extremely important factors in the understanding of the pathophysiology and mechanics of the cardiovascular system. The stress and strain cannot be analysed without exact knowledge of the mechanical properties of the wall. In addition, knowledge on biomechanical properties of arterial walls is necessary for credible description of their constitutive behaviour in Finite Element Analyses (FEA). Computational modeling enables us a better prediction of the outcome of interventional treatments (e.g. balloon angioplasty). The most usual tests to determine the mechanical properties of arterial walls are uniaxial and biaxial tests on flat specimens. Uniaxial loading tests of a sliced ring of an arterial wall or a strip of tissue is simple but provides us with basic and useful information on the material properties (Hayashi 1993).

When it comes to cardiovascular research, the swine model is a very popular one because of the anatomic and haemodynamic similarities to humans. In addition, the extent of collateral vessels and the size of coronary arteries in the heart are also very comparable to humans. Because of these similarities and the unlimited availability of samples, the swine model is very important in the advance of knowledge of cardiovascular physiology of humans and is imperative for clinical and translational research (Kassab 2006).

Preconditioning is believed by many to be an important component of testing biological tissues. The proposed benefits of preconditioning are that it provides a known loading history and produces a consistent and reproducible state for the period of data recording (Fung 1993). For these reasons, preconditioning has become a standard protocol used in many tests of biological tissues. Many researchers have investigated the stress–strain responses of biological tissues under various combinations of strain and strain rate. In preconditioning, the specimen is loaded and unloaded through several cycles to a fixed target load or a target extension, until adjacent curves “appear” to be identical. The number of reported preconditioning cycles has ranged from 1, (Haut & Little 1972) to a few (3–5), (Carew et al. 1999; Kwan et al. 1993; Pinto & Patitucci 1980) to several (>10), (Carew et al. 2000; Sauren et al. 1983; Schatzmann et al. 1998; Teramoto & Luo 2008) depending on the material being tested and the particular type of uniaxial test. Although the exact mechanisms of preconditioning remain unknown, it is likely that cyclic loading to a fixed load induces some structural rearrangement within the material to which it can return if subjected to the same loading protocol (Quinn & Winkelstein 2011; Miller et al. 2012).

The effect of preconditioning has been investigated for a number of tissues such as aortic valve (Carew et al. 2000; Carew et al. 2004), cardiac muscle (Pinto & Patitucci 1980), ligament and tendon, and brain (Gefen et al. 2003). For example, Carew et al. (2004) suggested using repeated stress–relaxation cycles as a method of preconditioning and Cheng et al. (2009) investigated the effect of preconditioning strain on the stress – strain and stress relaxation responses.

Gefen et al (2003) showed that there is variation in tissue properties when preconditioning is not performed when they did tests on rat brain tissue. They used indentation testing on the brains of

rat of 13, 17, 43 and 90 days old rats and calculated the effective shear modulus in situ and in vitro for a total of 42 animals. The brain – braincase composite was preconditioned in order to stabilize the mechanical response of the tissue by indenting the tissue for 5 cycles to a depth of 1 mm, with the indentor held for 160 sec for each cycle. The non-preconditioned shear moduli at any given age were significantly greater than preconditioned shear moduli.

To test the hypothesis that stretching prior to exercise can protect against injury, researchers have investigated the effect of preconditioning on ligaments and tendons. Schatzmann et al. (1998) tested the human quadriceps tendon – patella (QT-B) patellar ligament – tuberosity (PL-B) complexes with cyclic preconditioning cycles that consisted of uniaxial loading from 75 N to 800 N during 200 sinusoidal cycles. After cyclic preconditioning the tendons and ligaments were immediately loaded to ultimate failure in the same way as the tendons and ligaments that were not preconditioned. Failure loading was obtained with uniaxial loading parallel to the fibre axis at a deformation rate of 1 mm/s. the comparison of results showed that there were significant differences between the preconditioned and not preconditioned QT-B and PL-B complexes for the elasticity modulus at 200 N and 800 N. For the ultimate stress only and patellar ligament – bone complex showed significant differences. This was attributed to the structure of the fibres within the tendons. While patellar tendons consist mainly of parallel oriented fibres, quadriceps tendons show four obliquely structured layers. These obliquely running layers cannot perform the same uniform recruitment patterns as the patellar ligament during uniaxial loading because of scissoring movements. Su et al. (2008) tested medial collateral ligaments (MCL) and patellar tendons (PT) from male Sprague – Dawley rats. The samples were loaded to failure after sinusoidal cyclic loading. For the control, the contralateral specimens were preconditioned by five cycles of load as low as the cyclic stretching, and then were stretched to failure immediately. Specimens were preloaded for 1 N, and then subjected to sinusoidal strain oscillation profiles. The cyclic sinusoid oscillation profile was then applied under displacement control mode, with amplitude of 0.04 mm (0.5% strain) to maintain tensile loading from 0.5 to 1.5 N at 0.5 Hz during 150 sinusoid cycles. For the material properties, ultimate stress was significantly increased by cyclic stretching in both the MCLs (25%) and the PTs (54%), as was ultimate strain after cyclic stretching in the MCLs (16%) and PTs (21%). Elastic modulus in the cyclic group improved significantly in both the MCLs (14%) and PTs (53%). Teramoto & Luo (2008) tested Achilles rat tendons at six different preconditioning protocols. The samples in the control group were loaded to failure without preconditioning. In preconditioning groups, 30, 100, 300, 600, and 1000 s stretching at 2% strain were performed. The samples were subsequently loaded to failure. Statistical analysis of the results showed that preconditioning for 30 sec up to 600 sec to 2% strain increased the ultimate failure load and strength, while there were no significant differences in elastic modulus, stiffness and cross-sectional area.

1.10 Modelling of the aortic walls

Arterial tissue is a layered structure composed of elastin and collagen fibers. In general, this tissue is heterogeneous, anisotropic, and nonlinearly elastic (Fung 1993). Many different constitutive models have been developed for arterial tissue. The constitutive models that most accurately represent the hyperelastic behavior of arterial walls are based on two- or three-dimensional strain energy functions. Strain energy function is described as polynomial or exponential form of strain tensor components or strain invariants. Different strain energy functions for hyperelstic materials have been proposed by Mooney – Rivlin, Yeoh, Arruda – Boyce , Van der Waals, Ogden, Neo – Hookean , and

Fung, (ABAQUS User Manual). Strain energy from Mooney – Rivlin, Yeoh, Neo – Hookean, and Fung's models are a polynomial function of strain invariants. Arruda – Boyce and Van der Waals' models are more complicated formulations than previously mentioned polynomial formulations, containing a term for locking stretch. At the locking stretch, the slope of stress-strain curve increases significantly in the former model, while the latter model cannot be used because strain energy goes to infinity. Ogden's strain energy function is described as a function of principal stretches. Depending on the parameters that can be chosen by the user, the Ogden's model can be turned into the Mooney – Rivlin or the Neo – Hookean model. Such functions can model the non – linear elastic deformation of arterial walls, but they do not capture the anisotropy that is seen in most arterial tissue. Anisotropic, nonlinearly elastic models such as those of Fung (1979), Takamizawa & Hayashi (1987) and Humphrey (1995) are widely used for arterial tissue. Although these models may be suitable for the description of their overall mechanical response, they are incapable of providing insight into the microscopic level. At the same time, the physical meaning of the parameters in the models is unclear.

Therefore, increasing effort has been made in developing structural models that are able to relate the overall mechanical response to the corresponding effects at microscopic level. Holzapfel et al. (2001); Holzapfel & Weizsäcker (1998) and Gasser et al. (2006) have developed a constitutive model that combines isotropic and anisotropic hyperelastic strain energy functions. This model is suitable for orthotropic, nonlinearly elastic tissues, and accounts for the anisotropy and fibre dispersion through a fiber orientation angle parameter and a dispersion parameter. A possible application is shown in Hariton et al. (2007) for soft tissue remodeling, i.e. the orientation of the collagen fibres in the directions of the principal stresses. In Vychytil et al. (2012) it is used as part of an idealised model of an arterial wall as a two-layer system and tested on porcine carotid arteries under inflation. In Itskov et al. (2006) an anisotropic hyperelastic material is proposed for fibre-reinforced materials. Taking into account an arbitrary number of fibre families, the strain energy function is proposed as a sum of exponential functions which makes is suitable for the description of soft collagenous tissues. Also, an issue of polyconvexity as a favorable property of strain energy functions is addressed. The model is generalised in Ehret & Itskov (2007) and applied for the description of uniaxial and biaxial tension tests with human coronary arteries and abdominal aorta.

1.11 Aim and objectives

The overall objective of this study is to determine the effect of preconditioning on the mechanical properties of the porcine thoracic aorta and to formulate a finite element model based on the data from the mechanical tests in order to quantify the effect of preconditioning the behavior of the aorta under internal pressure loading. Towards that goal, uniaxial tensile tests on four groups of porcine thoracic aorta were performed in the axial and circumferential directions both with and without preconditioning. The data analysis of the raw data included the calculation of the elastin and collagen phase elastic modulus, the transition strain and stress and the ultimate tensile strength and failure strain. The existence of significant differences between the preconditioned and the not preconditioned groups was tested with Student's t-test.

The data from the tensile tests were used for the finite element modelling of the porcine aorta as a straight tube with constant thickness. Several material models were tested, elastic, hyperelastic, isotropic and anisotropic to determine the model with the best fit. Finally, the results of

the computational simulations were compared to literature results from inflation tests of the porcine thoracic aorta.

2. MATERIALS AND METHODS

2.1 Tissue procurement and dissection

Fresh porcine thoracic descending aorta samples were collected from the local abattoir directly after the slaughter. To minimise variability due to the topology of the tissue, the same anatomical part was isolated for the experiments. The part of the tissue had a length of approximately 5 cm right after the aortic arch. The samples were kept in phosphate buffered saline (PBS) (Dulbecco's PBS 2.7 mM KCl, 1.5 mM KH_2PO_4, 136.9 mM NaCl, 8.9 mM $Na_2HPO_4 \cdot 7H_2O$, Biochrom) while they were carried back to the lab to prevent dehydration. Once in the lab, the samples were cleaned from excess fat and blood clots and were cut axially along the side where the spine arterioles are branching (Figure 2.1)Figure 2.1: **The process of cutting samples for mechanical testing. In figure A the cutting block is put across the sample to acquire a circumferential strip (B). In figure C the cutter is placed axially and an axial strip is cut (D).**. Thus there were no holes in the tissue that was used for the biomechanical testing. 5 mm wide strips of tissue were cut axially and circumferentially (Figure 2.2) out of every sample and tested under tensile loading, using the cutting block shown in Figure 2.3.

2.2 Histological examination

Tissue samples were subjected to histological examination in order to visualise its histoarchitecture, which is a vital part to the response of the tissue under mechanical loading. Basic hematoxylin & eosin (H&E) stainings were carried out while the extracellular matrix's morphology was visualised with Elastica van Gieson. The methods are described in the following paragraphs.

2.2.1 Fixation, paraffin embedding and sectioning

2.2.1.1 Tissue fixation

The samples were placed into individual histological cassettes (Turboflow MICROM) fixed for 4-6 hours in neutral buffered formalin 10% v/v.

2.2.1.2 Dehydration and paraffin embedding

After fixation, the samples were placed into 70% absolute ethanol. For dehydration, the samples were immersed sequentially in solutions of ethanol starting at 70% followed by two steps of 90% and 100% ethanol for one minute each and finally in xylene for three steps, one minute each.

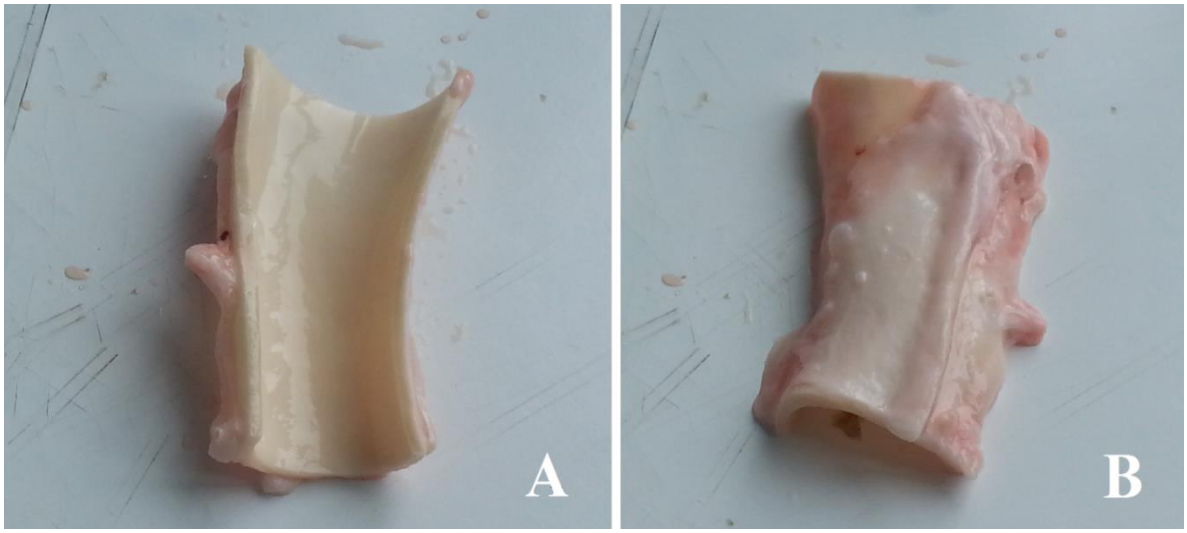

Figure 2.2: Aorta samples cut axially along the intercostal arteries.

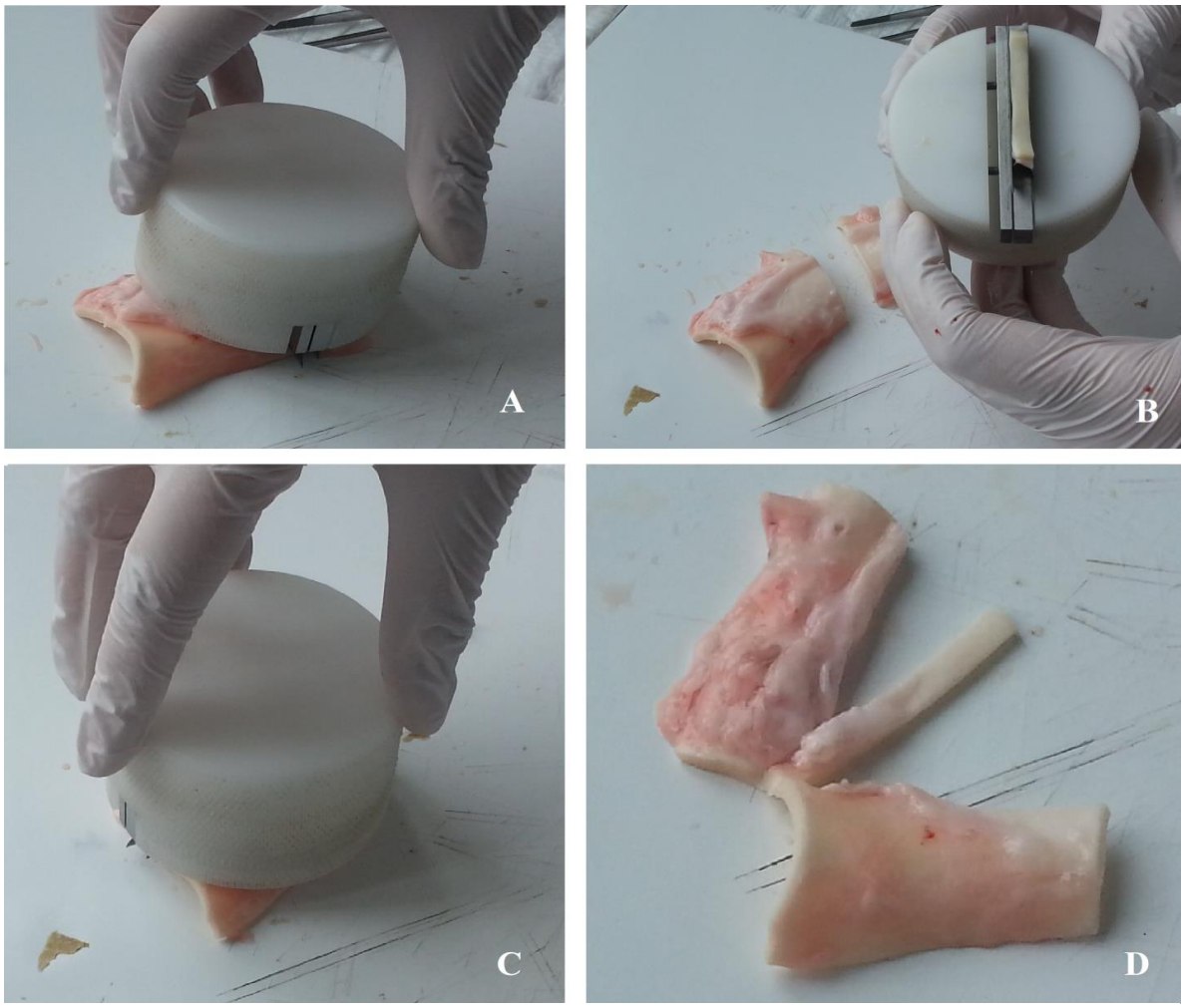

Figure 2.1: The process of cutting samples for mechanical testing. In figure A the cutting block is put across the sample to acquire a circumferential strip (B). In figure C the cutter is placed axially and an axial strip is cut (D).

The samples were taken out of the cassettes using heated forceps and were placed into metal moulds (Leica biosystems) partially filled with paraffin. While holding the sample in its desired orientation the moulds were transferred onto a cold plate to initiate the wax solidification and to secure the orientation. Afterwards, the cassettes were placed on top of the moulds, which then were filled with paraffin. The moulds were transferred onto the cold plate again and remained there until the wax was completely solid, at which point they were removed from the moulds.

The dehydration of the samples was carried out by the histology department of the Hannover Medical School in a Thermo Scientific Tissue Processor.

2.2.1.3 Sectioning

The paraffin embedded tissues were sectioned using a microtome (Reichert Jung) at a thickness of 5 μm. The sections were transferred into a water bath at 50°C and onto microscope slides (Silverfrost) for histological staining that were covered in glycerol (Sigma Chemical Company) to help attachment. The tissue sections were dried on a 60°C hotplate. Before staining, the sections were dewaxed by immersion in 2 pots of xylene for 10 min each, inside a fume hood and then they were sequentially rehydrated by immersion in a series of graded ethanol to distilled water (2 x 5 min in 100% ethanol, 1x 2 min in 95% ethanol, 1 x 2 min 70% ethanol)

2.2.2 Hematoxylin & Eosin staining

The sections were immersed into Mayer's Hematoxylin for 1 min, rinsed under tap water for 5 min and then immersed into Eosin for 3 min. Finally, they were dehydrated again through the graded alcohol solutions, cleared with xylene and mounted with Corbit Balsam mountant.

2.2.4 Elastica van Gieson staining

The sections were immersed into Elastin according to Weigert's Resorcinfuchsin solution for 11 min, rinsed under tap water for 1 min and then immersed into Weigert's Iron Hematoxylin solution

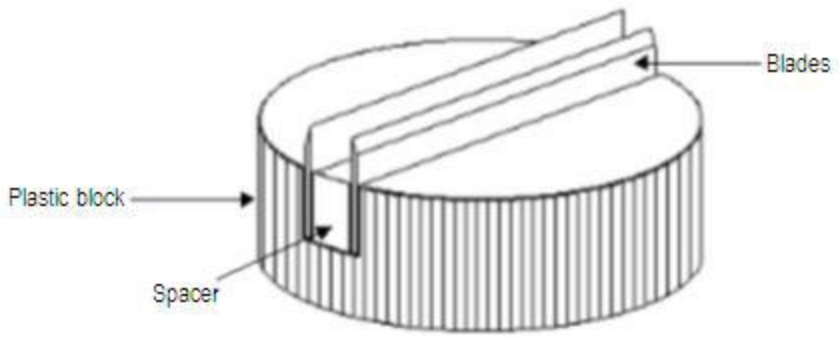

Figure 2.3: Cutting block used for the dissection of the tissue samples (Korossis 2002).

for 5 min. finally, they were dehydrated again through the graded alcohol solutions and mounted with Corbit Balsam mountant. Brightfield microscopy (Nikon Eclipse TE300 Inverted Microscope) was used to photograph the sections stained with Hematoxylin & Eosin and Elastica van Gieson.

2.3 Biomechanical testing

2.3.1 Testing materials

The investigation of the mechanical properties under uniaxial tensile loading involved the study of four groups of porcine aorta. The mechanical properties were determined for two directions – axial and circumferential.

For each group six specimens were dissected from thoracic porcine descending aortas, each 5 mm wide. For the determination of the parameters that was later used for the preconditioning loading limits three samples for each group were tested. Table 2.1 shows the groups that were tested.

Table 2.1: Tissue groups tested under tensile loading.

Uniaxial loading to failure testing				
Group No.	**Group**	**Direction**	**n**	**Abbreviation**
1	Not preconditioned	Axial	6	NPA
2	Preconditioned	Axial	6	PA
3	Not preconditioned	Circumferential	6	NPC
4	Preconditioned	Circumferential	6	PC
Determination of preconditioning parameters				
Group No.	**Parameter**	**Direction**	**n**	**Abbreviation**
1	Transition strain	Axial	3	TSA
2	Transition strain	Circumferential	3	TSC
3	Preconditioning cycle number	Axial	3	CNA
4	Preconditioning cycle number	Circumferential	3	CNC

2.3.2Experimental procedure

2.3.2.1 Uniaxial tensile tests

All uniaxial tensile testing was performed in a Zwick/Roell Z0.5 (200 N load cell) testing system (Figure 2.4)Figure 2.4: **Zwick/Roell Z0.5 uniaxial testing system.**. Prior to the testing each sample's thickness was measured with a force and way sensor (Sylvac, µS246) (Figure 2.5) at three locations and then averaged. Subsequently, the sample was mounted onto the holders of the Zwick Roell which were at a distance of 10 mm. Thus, the testing length of each sample was 10 mm. Due to the lack of a saline bath and to prevent dehydration during the test, PBS was sprayed frequently onto the sample. All measurements were executed at room temperature.

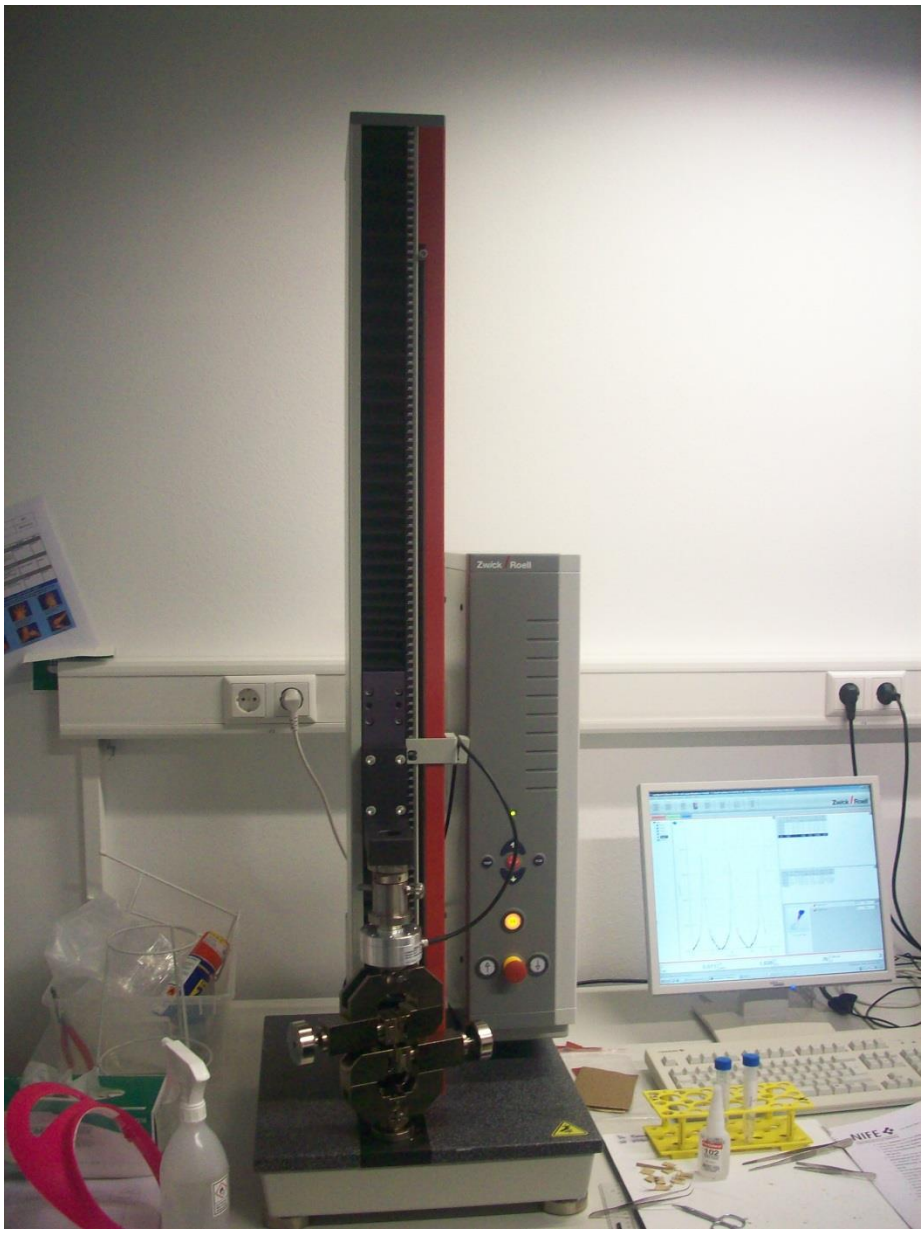

Figure 2.4: Zwick/Roell Z0.5 uniaxial testing system.

2.3.2.1.1 Preconditioning and loading to failure

After the samples were mounted onto the holders they were subjected to low strain rate uniaxial tensile loading to failure at 20 mm/min extension rate. The tensile machine was programmed to produce a sample preloading of 0.005 N before the operating program started to record any data. The reason behind this was the level of noise of the load cell. The value of 0.005 N was set just above the noise level of the load cell. During the testing, the force data from the load cell and the sample extension data were recorded.

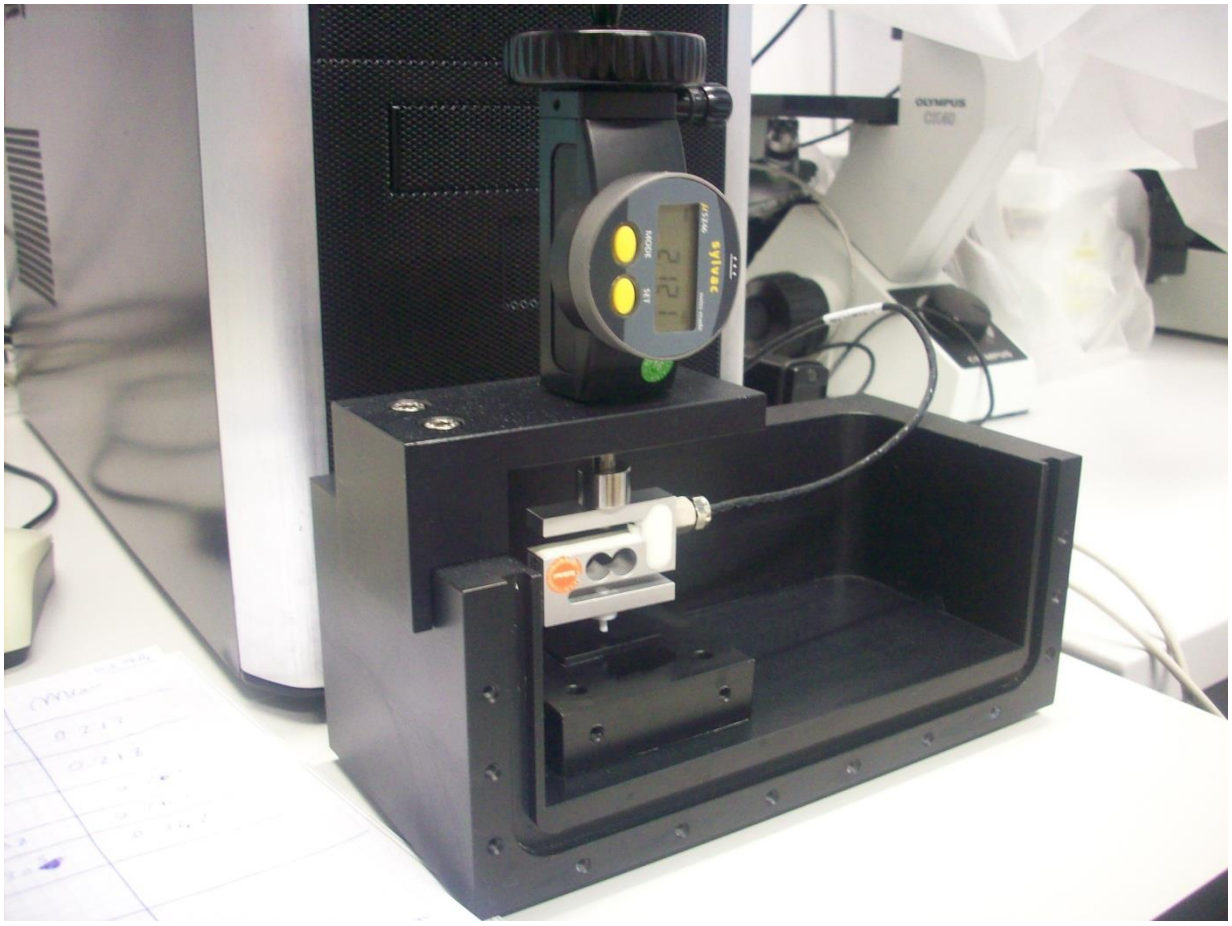

Figure 2.5: The force and way sensor (Sylvac µS246) that was used for the measuring of the thickness of the samples before the uniaxial loading.

Simple loading to failure was performed on groups NPA, NPC, TSA, TSC. The data from groups TSA and TSC were used to calculate the transition strain that was used as the limit for the preconditioning testing. The groups CNA and CNC were loaded 60 times to the transition strain and then back to zero strain. After the determination of the average number of cycles needed for preconditioning the groups PA and PC were preconditioned for the average number of cycles up to the transition strain and then immediately loaded to failure. The same extension rate of 20 mm/min was used in every test.

2.3.3 Analysis of the results

2.3.3.1 Analysis of the mechanical test results

The recorded force – extension data were transformed into stress – strain in Microsoft Excel 2010. The engineering stress was calculated according to the formula

(2)

$$\boldsymbol{\sigma} = \frac{\boldsymbol{F}}{\boldsymbol{A_0}} \tag{2.1}$$

where F was the force in N and A_0 the cross sectional area of the undeformed state in mm^2. Thus the engineering stress result was in MPa. All results for stress and length are presented MPa and mm. The formula used for the cross sectional are was

$$\boldsymbol{A = wt} \tag{2.2}$$

where w is the width (5 mm) of the sample and t its average thickness. The engineering strain was calculated from the formula

$$\boldsymbol{\varepsilon} = \frac{\boldsymbol{\Delta l}}{\boldsymbol{\Delta l_i + l}} \tag{2.3}$$

where Δl is the extension of the crosshead (deformation of the sample), l its original length (10 mm) and Δl_i is the extension produced by the preloading. The stress – strain data were plotted to give the stress – strain curve which was then used to calculate the elastin phase elastic modulus (E_{el}), the collagen phase elastic modulus E_{coll} , the ultimate tensile strength (UTS) and failure strain (ε_{fail}) and the transition strain (ε_{tr}) and stress (σ_{tr}) as they were defined in paragraph 1.6 Stress-strain relationship of soft tissues under uniaxial elongation. For the E_{coll} and E_{el} the parts of the curve which represented most these slopes were isolated in Microsoft Excel 2010 and a linear trendline was fitted the slope of which were the E_{coll} and E_{el}. The six parameters were then averaged over the number of samples and used for the statistical analysis.

2.3.3.2 Statistical analysis

All statistical analyses were performed in Microsoft Excel 2010 and all numerical values are presented as mean ± 95% confidence interval (C.I.). For the comparison of the groups of two means, the Student's t-test was used. The confidence intervals were as such: calculated by the Student's t-distribution and the standard error of the mean (SE mean) for each parameter, estimated from

$$\mathbf{95\%}\ \boldsymbol{C.I.} = \boldsymbol{Mean} \pm \boldsymbol{t}\ \frac{\boldsymbol{\sigma}}{\sqrt{\boldsymbol{n}}} \tag{2.4}$$

where σ is the standard deviation, n the sample size and t the t-distribution's value for n-1 degrees of freedom. The statistical significance of the difference between the groups was determined at the 0.05 cut-off level.0

2.4 Computational modelling of the aorta

2.4.1 Geometry

All finite element analyses were performed on ABAQUS/Standard (Dassault Systèmes). A porcine fresh aorta is modeled as a straight tube with a constant inner radius of 9 mm, a constant wall

thickness of 2 mm and an arbitrary length of 150 mm created from a 3D deformable solid part. The values for the thickness and diameter are the results of measurements of the thickness and diameter on five aorta samples. Refer to Figure 2.6 for the ABAQUS model of the geometry.

2.4.2 Material

2.4.2.1 Curve averaging

The experimental data from the uniaxial loading were used for the curve fitting of the different material models that were investigated. For that reason, the stress – strain curves from each of the four test groups were averaged. After the mean ε_{tr} for each group was calculated, the curves were moved to become in phase according to the ε_{tr}. Then the curves were fitted with trendlines, extended to the mean ε_{fail} and to zero and averaged.

2.4.2.2 Elastic Isotropic Material

Since it is known that during physiological loading inside the body the tissues do not surpass the transition phase, the first and simplest material model that was used to simulate the porcine aorta was a linear isotropic model with Young's modulus equal to the E_{el} from the preconditioned and not preconditioned circumferential test groups and Poisson's ratio $\nu = 0.499999$ (the material was modeled as incompressible in all cases (Chuong & Fung 1984; Carew et al. 1968). The reason that the modulus from the circumferential direction was chosen is the loading conditions that were imposed on the model.

2.4.2.3 Neo Hookean Material

The second material model applied was the Neo Hookean material model (ABAQUS User Manual). A Neo Hookean solid is a hyperelastic material model proposed by Ronald Rivlin in 1948 similar to Hooke's law that can be used to predict the non-linear behaviour of materials undergoing large deformations. The strain energy function of an incompressible Neo Hookean material is

$$\boldsymbol{W = C_1(I_1 - 3)} \tag{2.5}$$

Where C_1 is a material constant to be determined by data fitting and I_1 is the first invariant of the left Cauchy – Green deformation tensor **B**.

2.4.2.4 Mooney – Rivlin Material

The Mooney – Rivlin (ABAQUS, User Manual) solid is a hyperelastic material model where the strain energy function W defined as

$$\boldsymbol{W = C_{10}(I_1 - 3) + C_{01}(I_2 - 3)} \tag{2.6}$$

where C_{10} and C_{01} are material constants related to the distortional response, I_1 and I_2 are the first and second invariants of the left Cauchy – Green deformation tensor **B.**

2.4.2.5 Ogden Material

The Ogden material model was developed in 1972 by Ogden (ABAQUS User Manual). to describe the non-linear behaviour of rubbers, soft tissues and polymers. The strain energy function is

$$\boldsymbol{W = \sum_{i=1}^{N} \frac{2\mu_i}{a_i^2}\left(\lambda_1^{\alpha_i} + \lambda_2^{\alpha_i} + \lambda_3^{\alpha_i} - 3\right)} \tag{2.7}$$

Where μ_i and α_i are the material constants and $\lambda_1, \lambda_2, \lambda_3$ the principal stretches.

2.4.2.6 Reduced polynomial material

A special case of the general polynomial material model is the reduced polynomial model which is obtained if all C_{ij} with $j \neq 0$ are set to zero (ABAQUS User Manual).

$$\boldsymbol{W = \sum_{i=0,j=0}^{\infty} C_{ij}(I_1 - 3)^i (I_2 - 3)^j \Rightarrow W = \sum_{i=0}^{\infty} C_{i0}(I_1 - 3)^i} \tag{2.8}$$

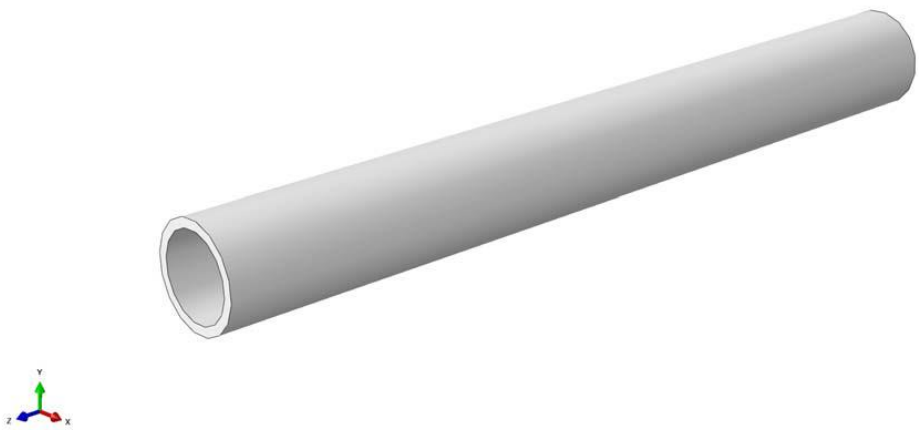

Figure 2.6: Geometry for a straight tube approximation of a porcine thoracic descending aorta modeled in ABAQUS.

The reason behind this modification according to Yeoh (1993) is the sensitivity in which the strain energy function changes with respect to the second invariant, which is much smaller than the sensitivity to changes in the first invariant. In addition, this dependence on I_2 is difficult to measure, thus it might be preferable to neglect it rather than calculate it based on potentially inaccurate measurements. Finally, it seems that neglecting the I_2 dependence makes the model better able to predict response to other modes of loading if only one is known.

2.4.2.7 Holzapfel – Gasser – Ogden material

Until now, the constitutive behaviour of hyperelastic materials was discussed in the isotropic context. However, many materials of industrial and technological interest exhibit anisotropic elastic behavior due to the presence of preferred directions in their microstructure. Examples of such materials include common engineering materials (such as fiber-reinforced composites, reinforced rubber, and wood) as well as soft biological tissues (such as those found in arterial walls and heart tissues). Under large deformations these materials exhibit highly anisotropic and nonlinear elastic behavior due to rearrangements in their microstructure, such as reorientation of the fiber directions with deformation. The simulation of these nonlinear effects requires constitutive models formulated within the framework of anisotropic hyperelasticity.

Using the continuum theory of fibre – reinforced composites, the strain energy function can be expressed directly in terms of the invariants of the deformation tensor and fiber directions. For example, consider a composite material that consists of an isotropic hyperelastic matrix reinforced with families of fibers. The directions of the fibers in the reference configuration are characterized by a set of unit vectors $\mathbf{A}_\alpha$ (α = 1,...,N). Assuming that the strain energy depends not only on deformation, but also on the fiber directions, the following form is postulated:

$$\boldsymbol{W = W(C, A_\alpha)} \quad , \quad \boldsymbol{a = 1, \dots, N} \tag{2.9}$$

The form of the strain energy potential is based on that proposed by Holzapfel, Gasser and Ogden (Gasser et al. 2006; Holzapfel et al. 2001) for modeling arterial layers with distributed collagen fibre orientations.

$$\boldsymbol{W = C_{10}(I_1 - 3) + \frac{k_1}{2k_2}\sum_{\alpha=1}^{N}\{exp[k_2\langle\bar{E}_\alpha\rangle^2] - 1\}} \tag{2.10}$$

with

$$\boldsymbol{\bar{E}_\alpha \equiv \kappa(I_1 - 3) + (1 - 3\kappa)(\bar{I}_{4(aa)} - 1)} \tag{2.11}$$

where W is the strain energy per unit of reference volume; C_{10}, D, k_1, k_2 and κ are temperature dependent material parameters; N is the number of fibre ($N \leq 3$); I_1 is the first invariant of **C** and $\bar{I}_{4(aa)}$ are pseudo-invariants of **C** and $\mathbf{A}_\alpha$:

$$\boldsymbol{\bar{I}_{4(aa)} = A_\alpha C A_\alpha} \tag{2.12}$$

The model assumes that the directions of the collagen fibres within each family are dispersed with rotational symmetry about a mean preferred direction. The parameter κ ($0 \leq \kappa \leq \frac{1}{3}$) describes the level of dispersion in the fibre directions. If ρ(Θ) is the orientation density function that represents the normalised number of fibres with orientations in the range [Θ, Θ + dΘ] with respect to the mean direction, the parameter κ is defined as

$$\boldsymbol{\kappa = \frac{1}{4}\int_0^{\pi} \rho(\Theta) sin^3 \Theta d\Theta}. \tag{2.13}$$

It is also assumed that all the families of fibres have the same mechanical properties and the same dispersion. When $\kappa = 0$, the fibres are perfectly aligned. When $\kappa = \frac{1}{3}$, the fibres are randomly and the material becomes isotropic; this corresponds to a spherical orientation density function.

The strain – like quantity $\bar{E}_\alpha$ characterises the deformation of the family of fibres with mean direction $\mathbf{A}_\alpha$.

$$\boldsymbol{\bar{E}_\alpha \equiv \bar{I}_{4(\alpha\alpha)} - 1} \tag{2.14}$$

for perfectly aligned fibres ($\kappa = 0$) and

$$\boldsymbol{\bar{E}_\alpha \equiv \frac{(I_1 - 3)}{3}} \tag{2.15}$$

for randomly dispersed fibres ($\kappa = \frac{1}{3}$) (isotropic material).

The first term in the expression of the strain energy function has a Neo – Hookean form and represents the distortional contribution of the non – collagenous isotropic ground substance; and the second term represents the contributions from the different families of collagen fibers, taking into account the effects of dispersion. A basic assumption of the model is that collagen fibers can support only tension, as they would buckle under compressive loading. Thus, the anisotropic contribution in the strain energy function appears only when the strain of the fibers is positive or, equivalently, when $\bar{E}_\alpha > 0$. This condition is enforced by the term $\langle \bar{E}_\alpha \rangle$, where the operator $\langle \cdot \rangle$ stands for the Macauley bracket and is defined as $\langle \cdot \rangle = \frac{1}{2}(|\cdot| + \cdot)$.

The four parameters (C_{10}, k_1, k_2, κ) are obtained by means of the standard non-linear trust region algorithm. The following objective function is minimised

$$\boldsymbol{E = \sum_{i=1}^{NC} \left(\sigma_{\theta\theta,i} - \sigma^W_{\theta\theta,i}\right)^2 + \sum_{i=1}^{NA} \left(\sigma_{zz,i} - \sigma^W_{zz,i}\right)^2} \tag{2.16}$$

where NC, NA are the numbers of data points for the circumferential and axial direction respectively, $\sigma_{\theta\theta,i}$, $\sigma_{zz,i}$ are the engineering stresses in the circumferential and axial direction respectively that were calculated from the tensile test data, and $\sigma^W_{\theta\theta,i}$, $\sigma^W_{zz,i}$ are the engineering stresses in the circumferential and axial direction respectively predicted by the function W for the *i*th data record. The angle φ was kept constant at 39° and the aorta was modelled as a one layer with two fibre families.

Figure 2.7: Boundary and loading conditions. Internal pressure and fixed ends.

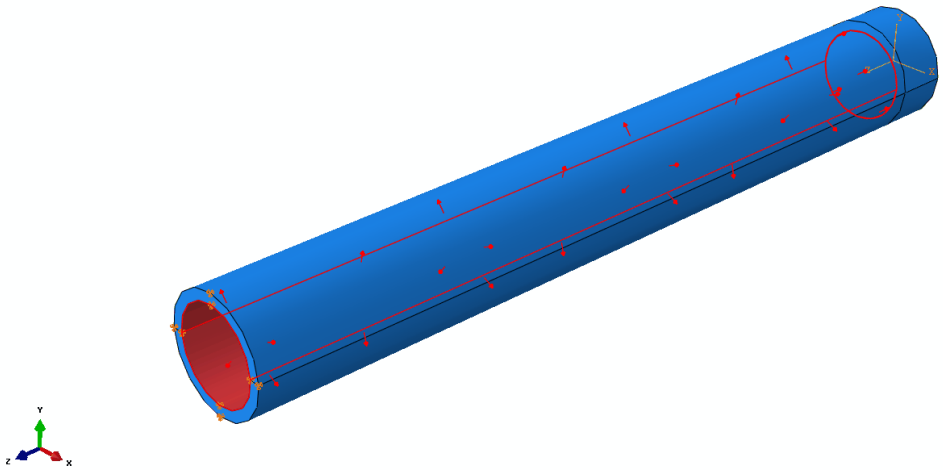

Figure 2.8: Boundary and loading conditions. Internal pressure and one fixed and one free end with plug.

In the formulation of their constitutive model of a blood vessel, Holzapfel et al. (2001) assigned separate strain energy functions, each of the form of (2.10, to the media layer and the adventitia layer. However, the media layers of the porcine thoracic aorta specimens used in this work were much thicker than the adventitia layers. This is not surprising considering the close proximity of the thoracic aorta to the heart, and the relative youth of the animals at the time of harvest (Fung 1993) . It was therefore assumed that the arterial wall for these specimens was approximately homogeneous and could be modeled by a single strain energy function with two fibre families. Holzapfel et al. (2001) also prescribed a fibre orientation angle, φ, for each layer, based on computation analysis of microscopy data. Such analysis was not performed in this study, instead, the angle φ was chosen as one that would help in the minimization of the objective function (2.16)

2.4.3 Boundary and loading conditions

The loading condition that was applied to the model was an internal pressure of 16 kPa which corresponds to the maximum physiological blood pressure in the thoracic aorta. The amplitude of the loading followed a ramp and hold fashion. The analysis is performed using an initial step and one

main analysis step. The initial step contains the boundary conditions and the main analysis step contains the pressure loading. The imposed boundary conditions and loading can be seen in Figure 2. and Figure 2.7.

2.4.4 Element type

When the material response is incompressible, the solution to a problem cannot be obtained in terms of the displacement history only, since a purely hydrostatic pressure can be added without changing the displacements. The nearly incompressible case (that is, when the bulk modulus is much larger than the shear modulus or Poisson's ratio, ν, is greater than 0.4999999) exhibits behavior approaching this limit, in that a very small change in displacement produces extremely large changes in pressure, so that a purely displacement-based solution is too sensitive to be useful numerically (for example, round-off on the computer may cause the method to fail). This singular behavior in the system is removed by treating the pressure stress as an independently interpolated basic solution variable, coupled to the displacement solution through the constitutive theory and the compatibility condition, with this coupling implemented by a Lagrange multiplier. This independent interpolation of pressure stress is the basis of these "hybrid" elements. More precisely, they are "mixed formulation" elements, using a mixture of displacement and stress variables with an augmented variational principle to approximate the equilibrium equations and compatibility conditions. The hybrid elements also remedy the problem of volume strain "locking," which can occur at much lower values of ν (i.e., ν = 0.49). Volume strain locking occurs if the finite element mesh cannot properly represent incompressible deformations. Volume strain locking can be avoided in regular displacement elements by fully or selectively reduced integration. All elements in ABAQUS are integrated numerically. Hence, the virtual work integral will be replaced by the summation

$$\int_V \boldsymbol{\sigma} : \boldsymbol{\delta D}\, \boldsymbol{dV} \rightarrow \sum_{i=1}^{n} \boldsymbol{\sigma_i} : \boldsymbol{\delta D_i V_i} \tag{2.17}$$

where n is the number of integration points in the element and V_i is the volume associated with the integration point i. Reduced integration is a procedure in which the number of integration point is sufficient to integrate exactly the contributions of the strain field that are one order less than the order of interpolation. The advantage of this procedure is that the strains and stresses are calculated at the locations that provide optimal accuracy, the so-called Barlow points (Barlow 1976). A second advantage is that the reduced number of integration points decreases CPU time and storage requirements. The disadvantage is that the reduced integration procedure can admit deformation modes that cause no straining at the integration points. These zero-energy modes make the element rank-deficient and cause a phenomenon called "hourglassing," where the zero energy mode starts propagating through the mesh, leading to inaccurate solutions. This problem is particularly severe in first-order quadrilaterals and hexahedra. To prevent these excessive deformations, an additional artificial stiffness is added to the element. In this so-called hourglass control procedure, a small artificial stiffness is associated with the zero-energy deformation modes. Consequently, the elements that were used for the model were 8-node linear, hybrid, brick elements with reduced integration and hourglass control (C3D8RH).

2.4.5 Equation solver and convergence criteria

Full Newton's method was used as the equation solver. Newton's method is a numerical technique for solving the nonlinear equilibrium equations. The motivation for this choice is primarily the convergence rate obtained by using Newton's method compared to the convergence rates exhibited by alternate methods (usually modified Newton or quasi-Newton methods) for the types of nonlinear problems most often studied with ABAQUS. The basic formalism of Newton's method is as follows. Assume that, after iteration i, an approximation u_i^M to the solution has been obtained. Let c^M_{i+1} be the difference between this solution and the exact solution to the discrete equilibrium equation $F^N(u^M) = 0$. This means that expanding this equation in a Taylor series about the approximate solution u_i^M gives

$$\boldsymbol{F^N(u_i^M) + \frac{\partial F^N}{\partial u^P}(u_i^M)c_{i+1}^P + \frac{\partial^2}{\partial u^P \partial u^Q}(u_i^M)c_{i+1}^P c_{i+1}^Q + \cdots = 0} \tag{2.18}$$

If u_i^M is an close approximate solution the magnitude of each c^M_{i+1} will be small so all but the two first terms can be neglected giving a linear system of equations:

$$\boldsymbol{K_i^{NP} c_{i+1}^P = -F_i^N} \tag{2.19}$$

where

$$\boldsymbol{K_i^{NP} = \frac{\partial F^N}{\partial u^P}(u_i^M)} \tag{2.20}$$

is the Jacobian matrix and

$$\boldsymbol{F_i^N = F^N(u_i^M).} \tag{2.21}$$

The next approximation to the solution is then

$$\boldsymbol{u_{i+1}^M = u_i^M + c_{i+1}^M} \tag{2.22}$$

and the iteration continues. Convergence of Newton's method is best measured by ensuring that all entries in F_i^N and all entries in c_{i+1}^M are sufficiently small.

For the time step ABAQUS/Standard uses a scheme based predominantly on the maximum force residuals following each iteration. By comparing consecutive values of these quantities, ABAQUS/Standard determines whether convergence is likely in a reasonable number of iterations. If convergence is deemed unlikely, ABAQUS/Standard adjusts the load increment; if convergence is deemed likely, ABAQUS/Standard continues with the iteration process. In this way excessive iteration is eliminated in cases where convergence is unlikely, and an increment that appears to be converging is not aborted because it needed a few more iterations. One other ingredient in this algorithm is that a minimum increment size is specified, in this case 10^{-7}, which prevents excessive computation in cases where buckling, limit load, or some modeling error causes the solution to stall.

3. RESULTS

This chapter summarises the experimental results obtained from the structural and biomechanical characterization and the computational models of the porcine thoracic aorta. The structural characterisation involved histological staining of aortic wall tissue sections. The biomechanical testing involved low strain uniaxial tensile loading of aortic wall strips. The computational models included the material model fitting of the data obtained from the uniaxial tests and their implementation in a finite element model. Finally, the validation study of the computational models involved the measuring of the aorta's dilation under internal pressure.

3.1 Histological characterisation

The mechanical properties of soft biological tissue depend highly on their structure, as they are anisotropic, composite materials. Thus histological staining of aortic wall strips to reveal the underlying microstructure was carried out to assist in interpreting the results from the biomechanical tests. Basic histology involved H & E staining of aortic wall strips (Figure 3.1). Collagen fibres and elastin were detected in the Elastica van Gieson staining. Collagen fibers were stained light purple, elastin dark purple, nuclei black-brown and muscle yellow (Figure 3.2).

The histological examination of the cross – sectional images revealed the three layers that comprise the aortic wall, the adventitia, media and intima, the adventitia showing a loosely formed network mostly out of collagen fibres and some elastin, the media consisting of a well- organized network of thickly woven collagen and elastin. H&E staining clearly demonstrated e spatial cell distribution in the aorta with the cell nuclei stained black by the haematoxylin and the cells appear to be spread throughout all the aortic layers. Samples stained with Elastic van Gieson demonstrate deep purple stained elastin and light purple stained collagen fibres.

3.2 Biomechanical characterisation

The effect of preconditioning on the tissue was investigated by employing uniaxial tensile tests on aortic wall strips. The strips were tested under low strain rate loading to failure with and without preconditioning. In the following paragraphs the results of these tests are presented.

3.2.1 Stress – strain behaviour

Four groups were used, each in the axial or circumferential direction with or without preconditioning. Each group included six samples of 10 mm in length and 5 mm in width. The average thickness of the samples in each group, measured at three points along their length, is shown in Figure 3.3. There were no significant differences between directions ($p = 0.91$ for the circumferential and $p = 0.37$ for the axial) but

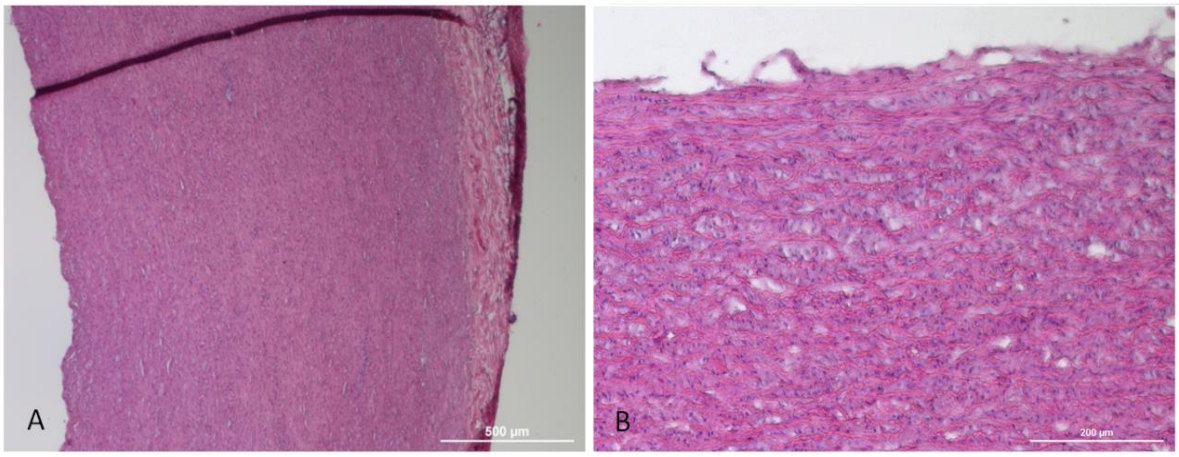

Figure 3.1: H & E staining of circumferential (A) and axial (B) strips or the aortic wall. The nuclei are stained black.

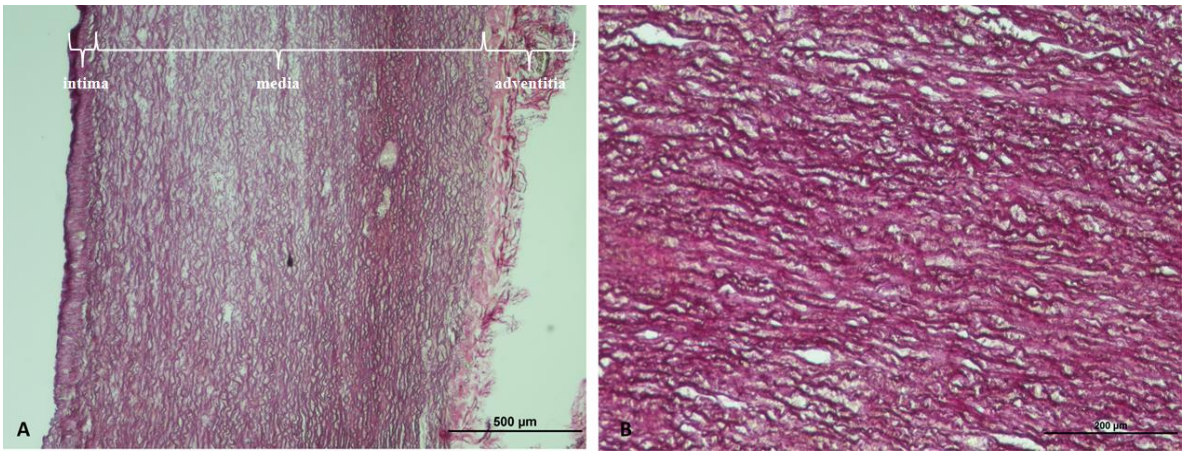

Figure 3.2: Elastica van Gieson staining of circumferential (A) and axial (B) strips of the aortic wall. Elastin is stained dark purple and the collagen fibres lighter purple/pink.

there were significant differences between groups ($p = 10^{-4}$ without preconditioning and $p = 0.03$ with preconditioning).

For the groups without preconditioning, the strips were loaded to failure at a constant speed of 20 mm/min. The mode of failure was middle section necking and rupture for most of the specimens while the rest failed at the clamping point.

For the groups with preconditioning, firstly the average transition strain and number of preconditioning cycles the strips were determined as described in Chapter 2. The average transition strain and preconditioning cycles for the circumferential and axial groups are presented in Table 3.1. The strips were then subjected to preconditioning and immediate loading to failure using these parameters as the preconditioning limits. The same observations as for the groups without preconditioning apply in this case as well. The load – elongation graphs of all groups were then converted into stress – strain graphs and the average curve was obtained (Figure 3.5Figure 3.5: **Average and individual stress – strain curves for the four groups.**).

The curves showed the characteristic J – like shape, staring with a low modulus region during the elastin phase and ending with a high modulus region during the collagen phase. The anisotropy of the tissue is highly expressed with the increased extensibility of the circumferential direction over the axial and the reduced ultimate tensile strength in the case of no preconditioning.

The groups with preconditioning showed similar loading to failure curves in the axial and circumferential directions.

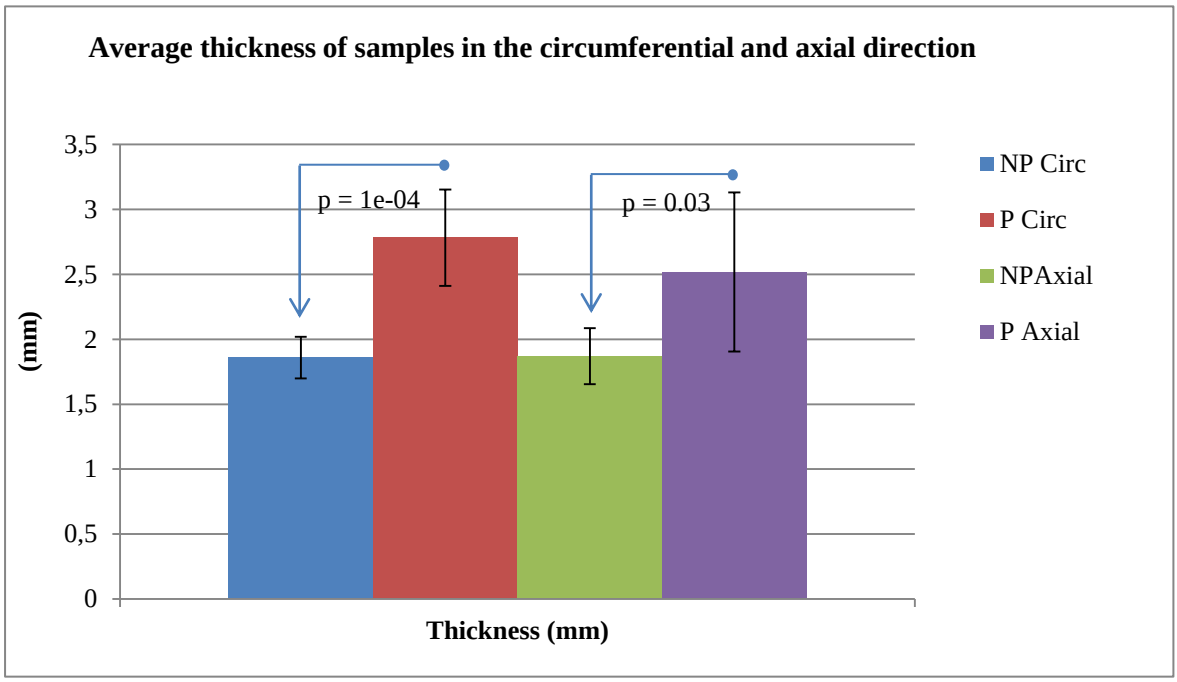

Figure 3.3: Average thickness of samples in the circumferential and axial direction for both the preconditioned and not preconditioned groups.

The elastin phase elastic modulus (E_{el}), the collagen phase elastic modulus (E_c), transition stress (σ_{tr}) and strain (ε_{tr}), ultimate tensile strength (UTS) and failure strain (ε_{UTS}) were calculated from the stress – strain curves of all the specimens. The average values of these parameters and the 95% confidence interval and the corresponding p – values obtained by the t – test among the preconditioned and not preconditioned groups are shown in Figure 3.6 - Figure 3.6 and in Table 3.2. In all cases, significant differences in the 95% confidence level were detected between the

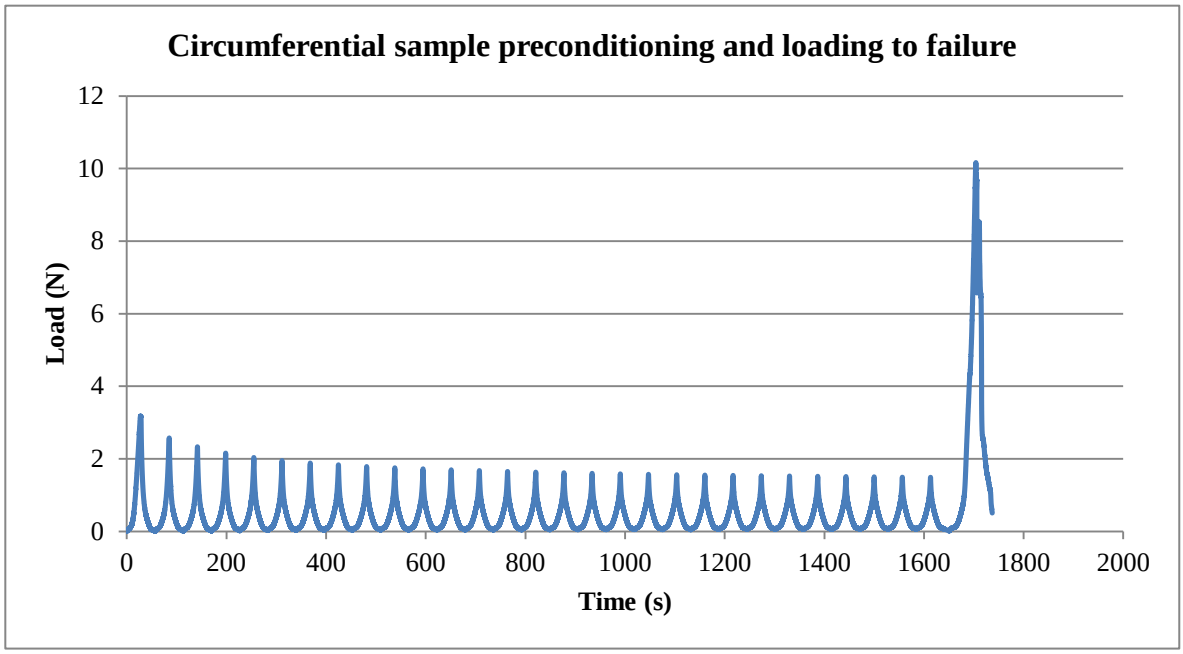

Figure 3.4: A typical graph of an aorta strip showing the preconditioning level – off and loading to failure right after.

preconditioned and not preconditioned groups except in the cases of ultimate tensile strength and elastin phase elastic modulus in the axial direction.

Table 3.1: Average values for transition strain and number of cycles for preconditioning.

	Transition strain	Number of cycles
Circumferential	86%	29
Axial	64%	47

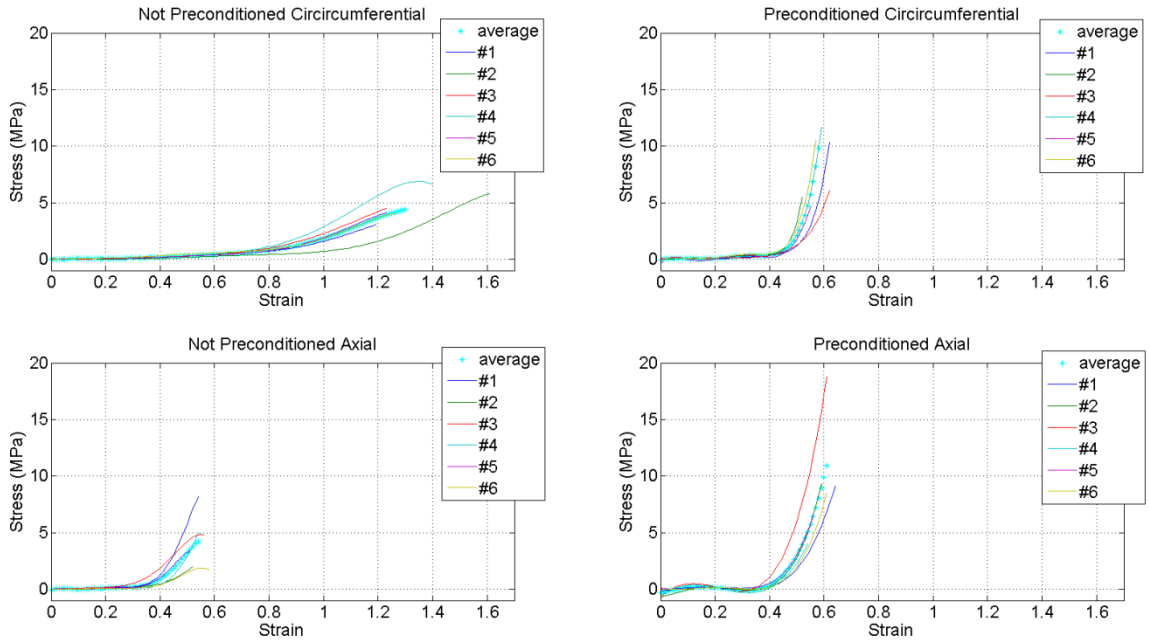

Figure 3.5: Average and individual stress – strain curves for the four groups.

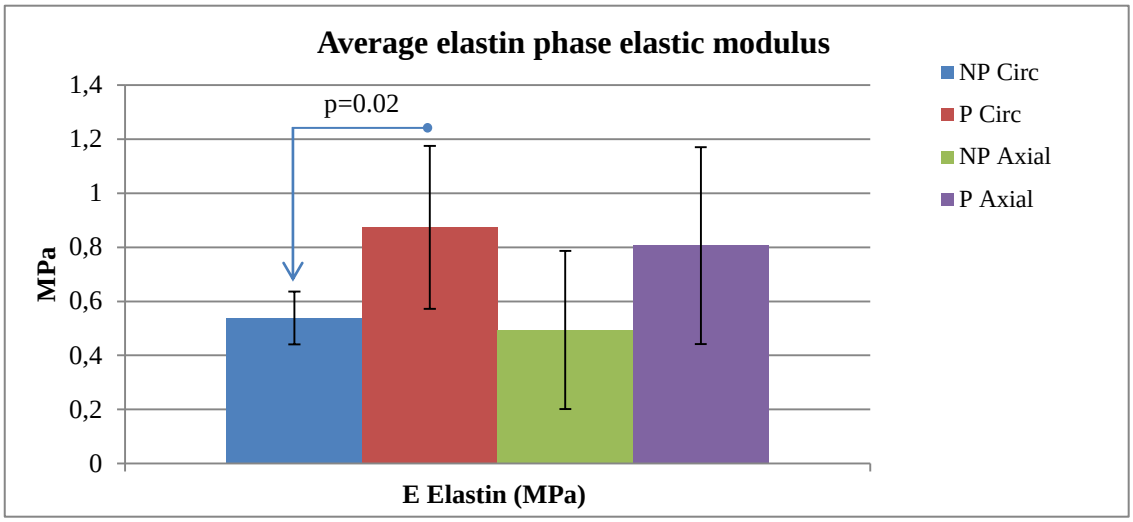

Figure 3.6: Average elastin phase elastic modulus for the two directions with and without preconditioning (mean ± 95% C.I.).

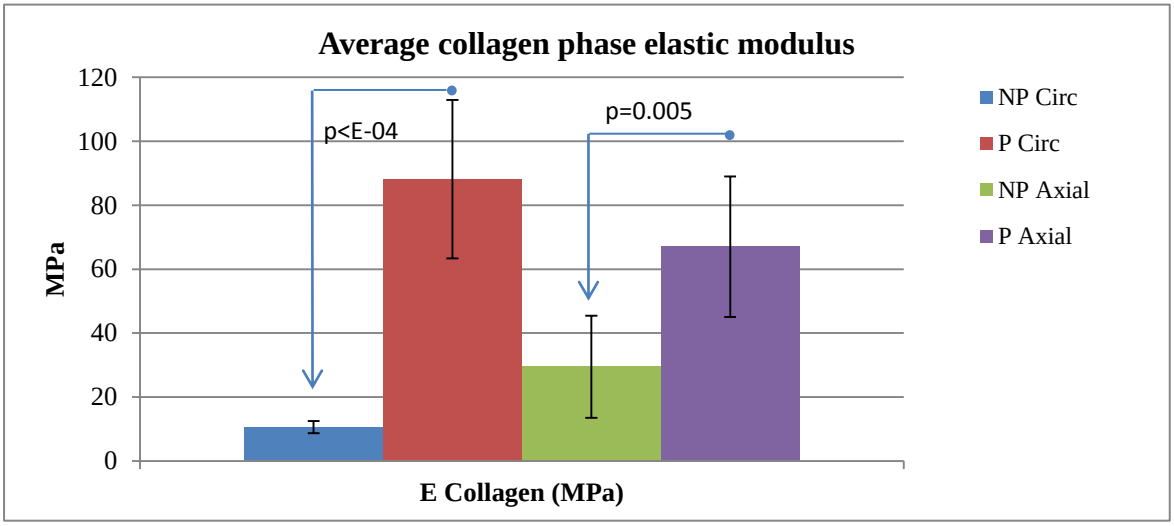

Figure 3.7: Average collagen phase elastic modulus for the two directions with and without preconditioning (mean ± 95% C.I.).

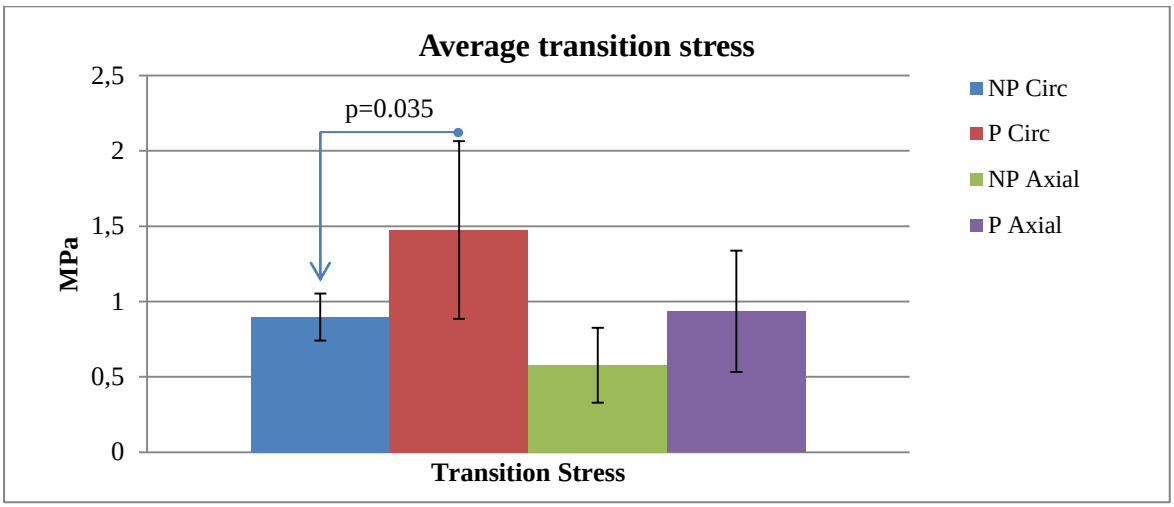

Figure 3.8: Average transition stress for the two directions with and without preconditioning (mean ± 95% C.I.).

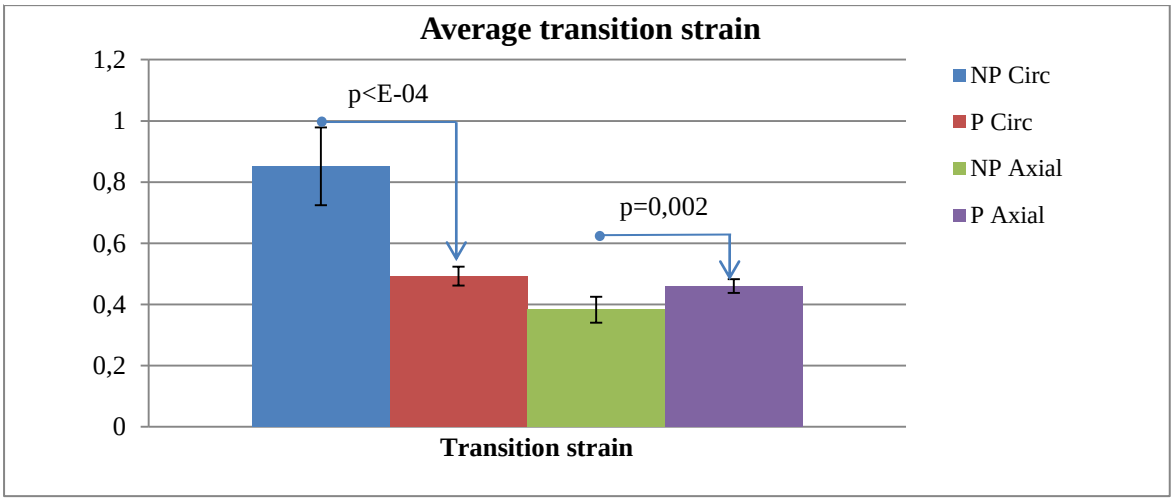

Figure 3.9: Average transition strain for the two directions with and without preconditioning (mean ± 95% C.I.).

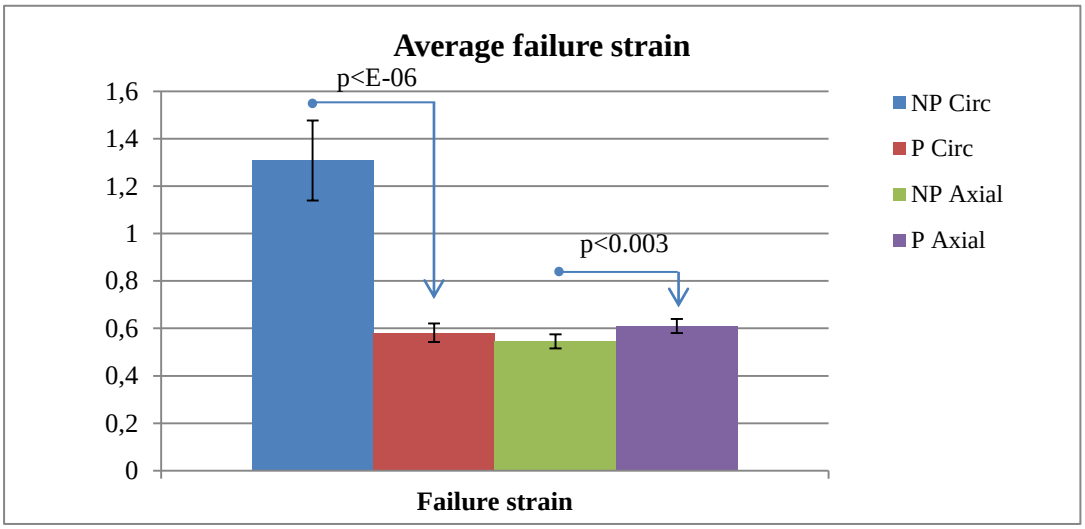

Figure 3.10: Average failure strain for the two directions with and without preconditioning (mean ± 95% C.I.).

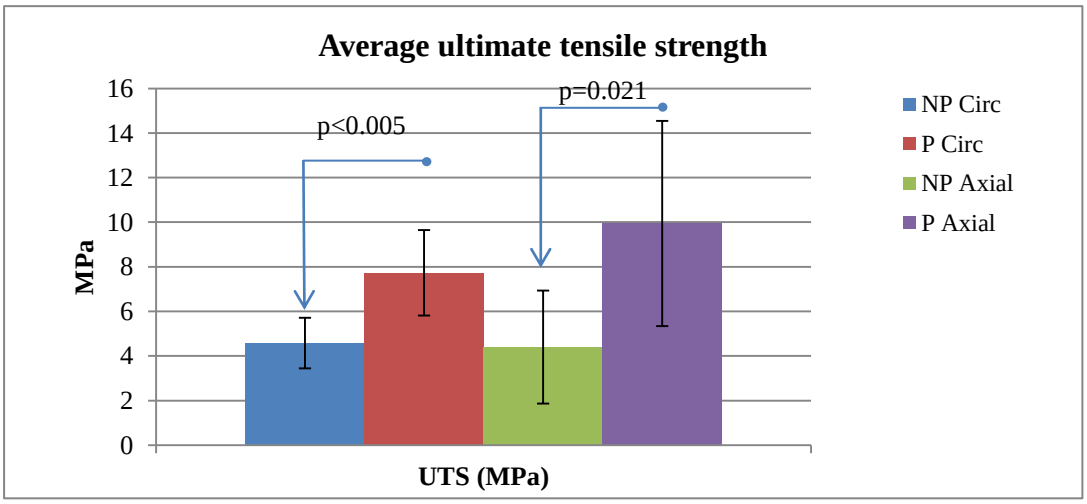

Figure 3.11: Average ultimate tensile strength for the two directions with and without preconditioning (mean ± 95% C.I.).

3.2.2 Material model fitting

The Neo – Hookean, Mooney – Rivlin, Ogden and Holzapfel material models were tested using the stress – strain curves obtained from the biomechanical testing. The average curves from the four groups were used in for the material model fitting. The model coefficients for the best fit to the experimental stress were calculated using the least squares regression (LSQ) function lsqcurvefit in MATLAB (8.3.0.532, The MathWorks Inc, Natick, MA). The residual norm of the LSQ was taken as a measure of best fit. The LSQ derived coefficients can be found in Table 3.3. The stresses in the circumferential and axial direction for each of the material models that were tested are

Table 3.2: Mean ± 95% C.I. and p-values for the parameters obtained from the uniaxial tensile tests as determined by the t – test between the preconditioned and the not preconditioned groups (n = 6). The asterisk indicates significant difference at the 95% confidence level.

Circumferential (n=6)						
	E_{el} (MPa)	E_c (MPa)	σ_{tr} (MPa)	ε_{tr}	σ_{UTS} (MPa)	ε_{UTS}
Preconditioned	0.87±0.12	88.13±24.73	1.47±0.59	0.49±0.03	7.73±1.92	0.58±0.04
Not preconditioned	0.54±0.10	10.59±1.90	0.90±0.16	0.85±0.13	4.58±1.14	1.31±0.17
p-value	0.0216*	1.13E-05*	0.035*	3.49E-05*	0.00465*	7.99E-07*
Axial (n=6)						
Preconditioned	0.81±0.36	66.97±21.97	0.93±0.40	0.46±0.02	9.94±4.61	0.61±0.03
Not preconditioned	0.49±0.29	29.46±15.99	0.38±0.24	0.57±0.04	4.39±2.53	0.55±0.03
p-value	0.116	0.00528*	0.0805	0.00211*	0.0218*	0.00255*

Neo Hookean

$$\sigma_{11} = x_1\left(2F_{11} - \frac{2}{F_{11}^3F_{22}^2}\right)$$
$$\sigma_{22} = x_1\left(2F_{22} - \frac{2}{F_{11}^2F_{22}^3}\right)$$

Mooney – Rivlin

$$\sigma_{11} = x_1\left(F_{22} - \frac{1}{F_{11}^2}\right) + x_2\left(2F_{11} - \frac{2}{F_{11}^3F_{22}^2}\right)$$
$$\sigma_{22} = x_1\left(F_{11} - \frac{1}{F_{22}^2}\right) + x_2\left(2F_{22} - \frac{2}{F_{11}^2F_{22}^3}\right)$$

Yeoh

$$\sigma_{11} = x_1\left(2F_{11} - \frac{2}{F_{11}^3F_{22}^2}\right) + 3x_3\left(2F_{11} - \frac{2}{F_{11}^3F_{22}^2}\right)\left(F_{11}^2 + F_{22}^2 + \frac{1}{F_{11}^2F_{22}^2} - 3\right)^2$$
$$+ 2x_2\left(2F_{11} - \frac{2}{F_{11}^3F_{22}^2}\right)\left(F_{11}^2 + F_{22}^2 + \frac{1}{F_{11}^2F_{22}^2} - 3\right)$$
$$\sigma_{22} = x_1\left(2F_{22} - \frac{2}{F_{11}^3F_{22}^2}\right) + 3x_3\left(2F_{22} - \frac{2}{F_{11}^2F_{22}^3}\right)\left(F_{11}^2 + F_{22}^2 + \frac{1}{F_{11}^2F_{22}^2} - 3\right)^2$$
$$+ 2x_2\left(2F_{22} - \frac{2}{F_{11}^2F_{22}^3}\right)\left(F_{11}^2 + F_{22}^2 + \frac{1}{F_{11}^2F_{22}^2} - 3\right)$$

Ogden 3rd order

$$\sigma_{11} = 2\frac{x_1}{x_2}\left(F_{11}^{x_2-1} - F_{22}(F_{11}F_{22})^{-x_2-1}\right) + 2\frac{x_3}{x_4}\left(F_{11}^{x_4-1} - F_{22}(F_{11}F_{22})^{-x_4-1}\right)$$
$$+ 2\frac{x_5}{x_6}\left(F_{11}^{x_6-1} - F_{22}(F_{11}F_{22})^{-x_6-1}\right)$$

$$\sigma_{22} = 2\frac{x_1}{x_2}\left(F_{22}^{x_2-1} - F_{11}(F_{11}F_{22})^{-x_2-1}\right) + 2\frac{x_3}{x_4}\left(F_{22}^{x_4-1} - F_{11}(F_{11}F_{22})^{-x_4-1}\right) + 2\frac{x_5}{x_6}\left(F_{22}^{x_6-1} - F_{11}(F_{11}F_{22})^{-x_6-1}\right)$$

where σ_{ii} are the components of the engineering stress tensor, x_i the LSQ derived model coefficients, F_{ii} components of the deformation gradient tensor. Table 3.4 shows the residual norm values between the constitutive models and the experimental data. The material models with the least residuals were the isotropic 3rd order Ogden and the anisotropic Holzapfel. The graphs presented in Figure 3.14 to Figure 3.18 show the curve fits.

Table 3.3: LSQ regression coefficients for the different material models for the preconditioned and not preconditioned.

		x_1	x_2	x_3	x_4	x_5	x_6
Neo Hookean	P	0.921	-	-	-	-	-
	NP	0.442	-	-	-	-	-
Mooney – Rivlin	P	0.00	2.581	-	-	-	-
	NP	0.12600	0.83730	-	-	-	-
Ogden 3rd order	P	0.00000	1.90620	0.00350	23.31520	0.00000	0.96900
	NP	0.12840	5.46470	1.48840	-6.02880	-1.4920	-6.01960
Reduced Polynomial 3rd order	P	0.00000	0.00000	0.14861	-	-	-
	NP	0.00000	0.00000	0.01726	-	-	-
Holzapfel	P	0.0043	0.06443	1.45017	0.00000	0.6873	-
	NP	0.0043	1.32268	0.53071	0.30742	0.6873	-

Table 3.4: Residual norms of LSQ regression against the experimental data preconditioned and not preconditioned.

Residual Norms

Neo Hookean	P	114.13
	NP	32.03
Mooney – Rivlin	P	104.25
	NP	29.58
Ogden 3rd order	P	2.39
	NP	0.31
Reduced Polynomial 3rd order	P	31.32
	NP	2.09
Holzapfel	P	3.15
	NP	1.15

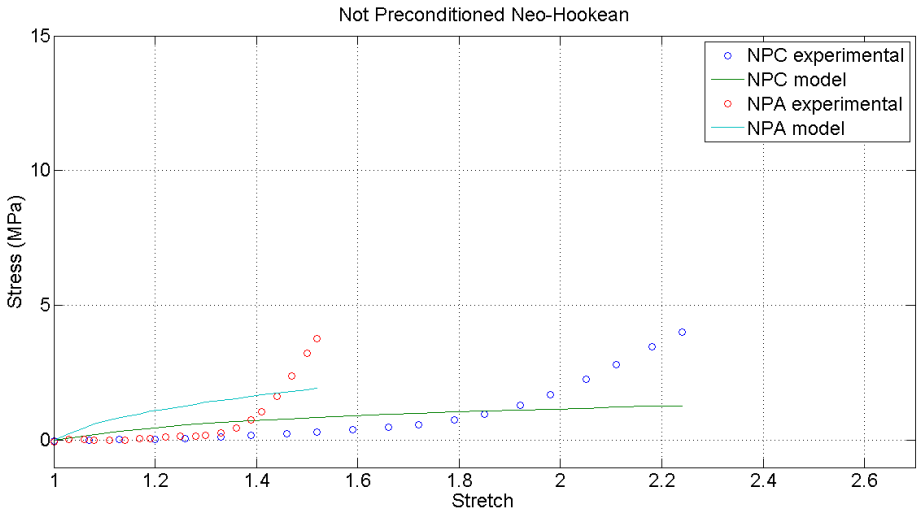

Figure 3.12: Experimental stress – strain data without preconditioning compared to the Neo - Hookean material model response.

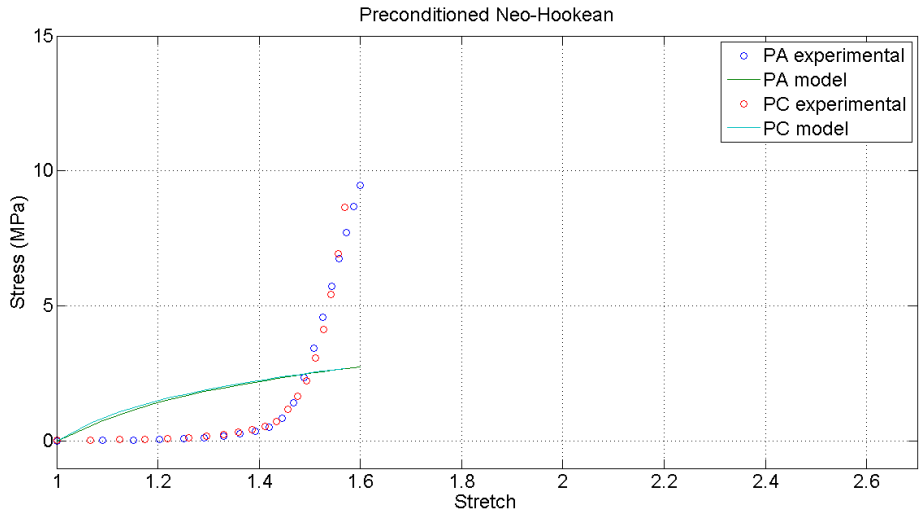

Figure 3.14: Experimental stress – strain data with preconditioning compared to Neo - Hookean material model response.

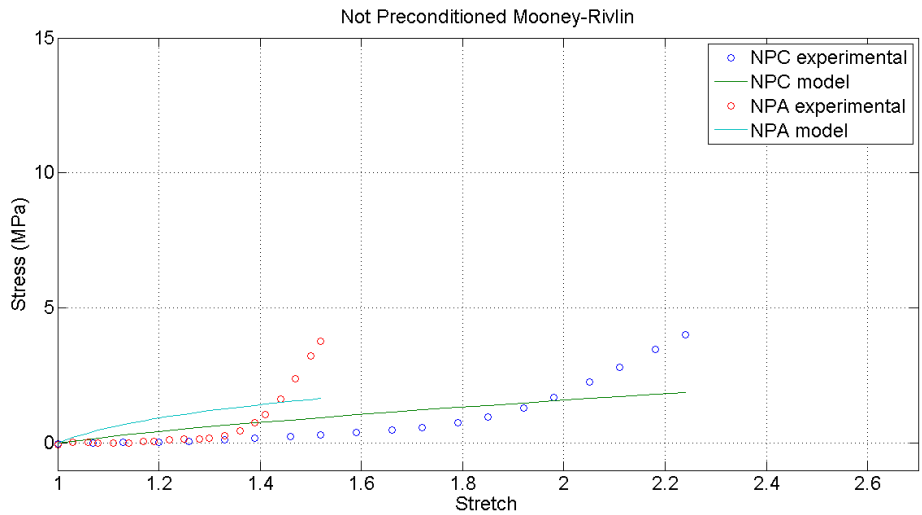

Figure 3.13: Experimental stress – strain data without preconditioning compared to the Mooney – Rivlin material model response.

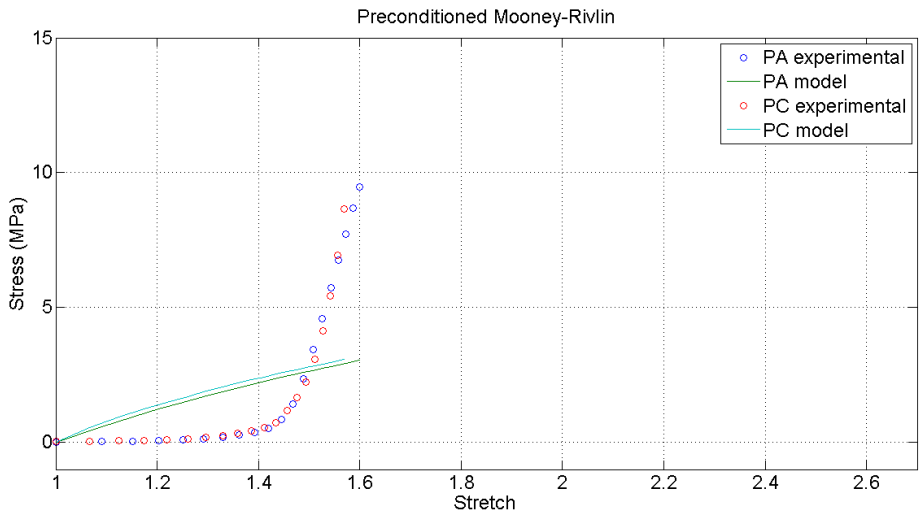

Figure 3.15: Experimental stress – strain data with preconditioning compared to the Mooney - Rivlin material model response.

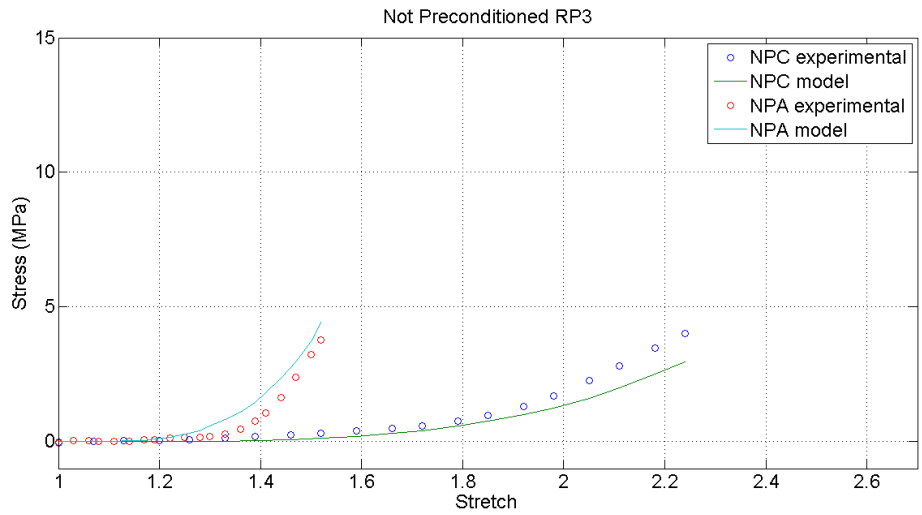

Figure 3.16: Experimental stress – strain data without preconditioning compared to the Reduced Polynomial 3rd order material model response.

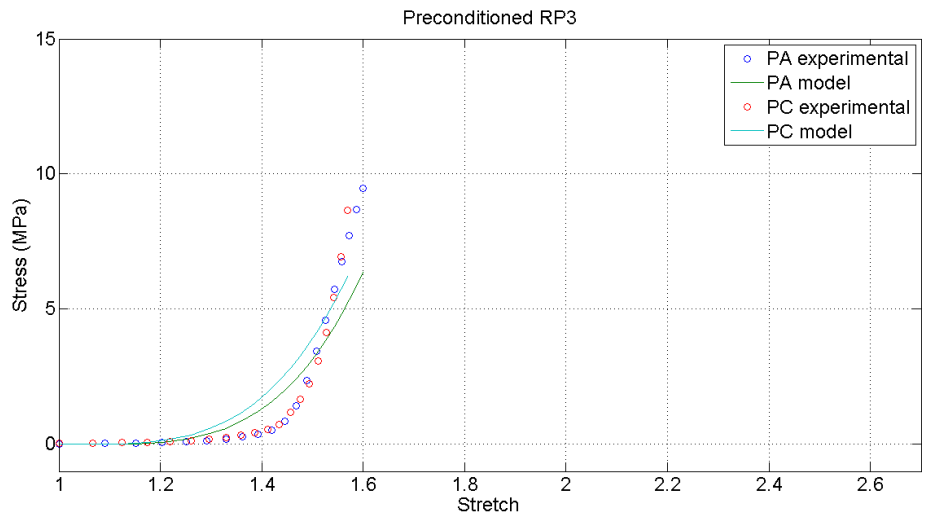

Figure 3.17: Experimental stress – strain data with preconditioning compared to the Reduced Polynomial 3rd order material model response.

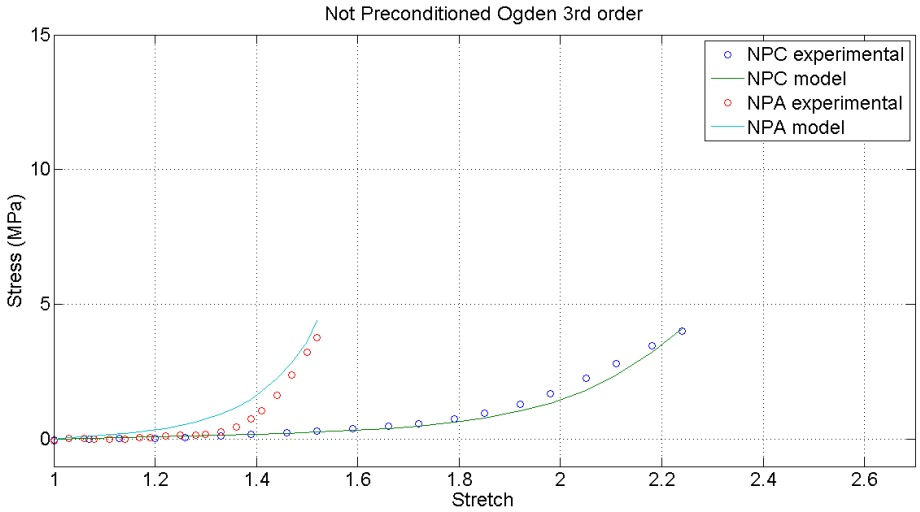

Figure 3.18: Experimental stress – strain data without preconditioning compared to the Ogden 3rd order material model response.

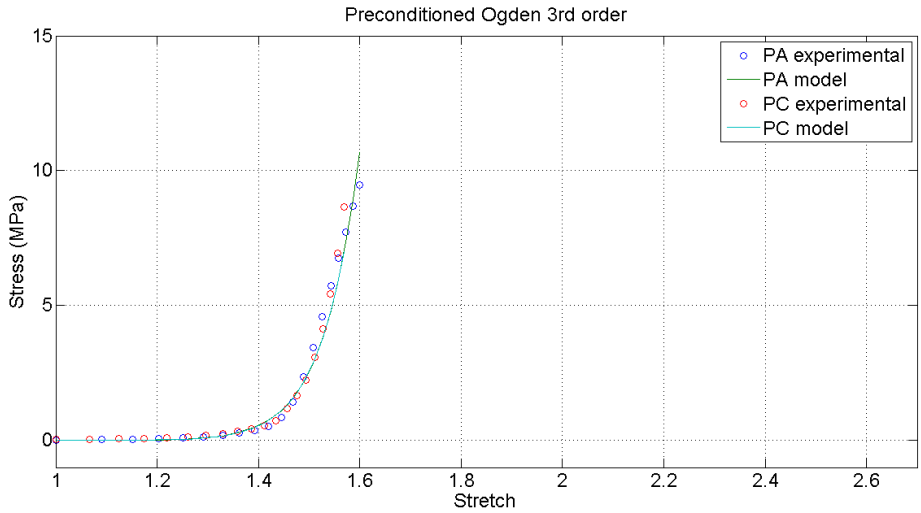

Figure 3.20: Experimental stress – strain data with preconditioning compared to the Ogden 3rd order material model response.

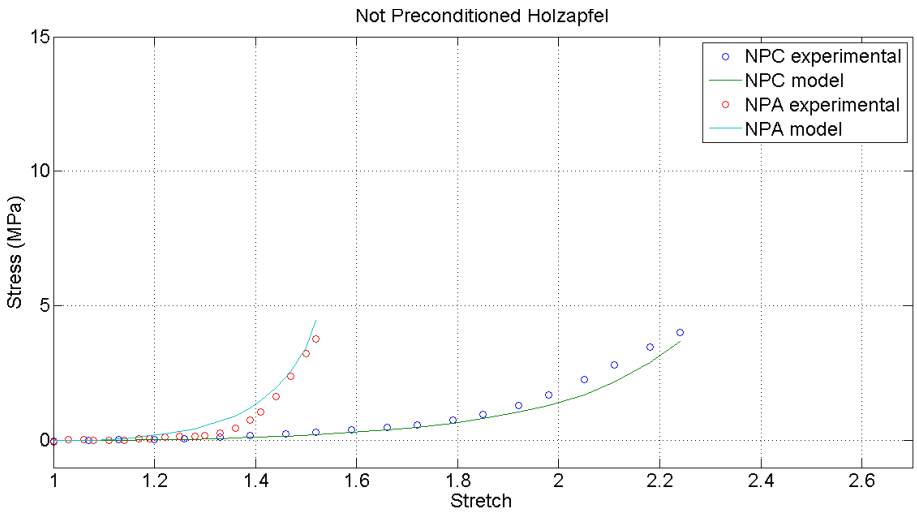

Figure 3.19: Experimental stress – strain data without preconditioning compared to the Holzapfel material model response.

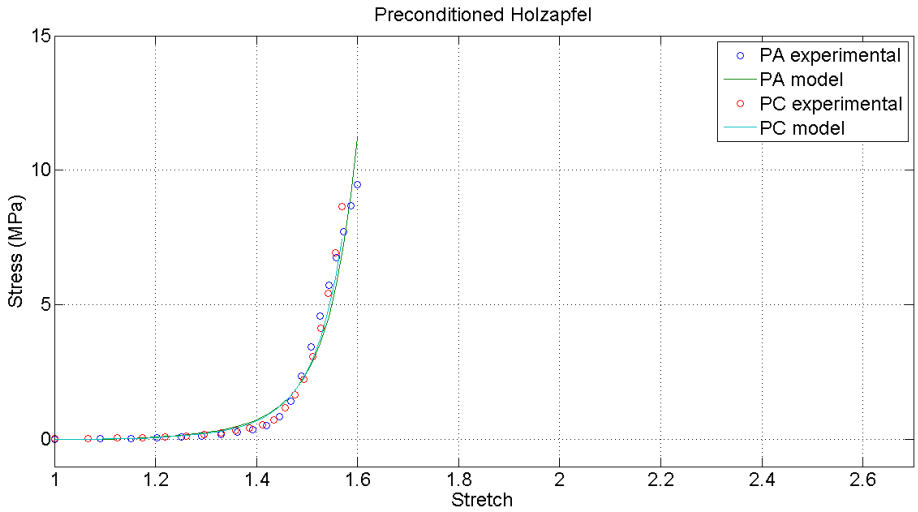

Figure 3.21: Experimental stress – strain data with preconditioning compared to the Holzapfel material model response.

3.3 Finite element method implementation

3.3.1 Mesh sensitivity study

A mesh sensitivity analysis was performed using three mesh sizes; coarse with 2,375 C3D8HR elements, medium with 18,600 C3D8HR elements and fine with 140,920 C3D8HR elements. The dependence of the analysis results on the mesh size was studied using the radial displacement of an area 75 mm axially from the end of the aorta. At the end of the analysis the discrepancy between the coarse mesh and the fine mesh for the two cases of geometry (fixed ends and free end with plug) were 2.5% and 55% respectively. The difference was reduced to 0.5% and 9.8% using the medium mesh. Due to the negligible differences between the medium and fine meshes and the large amount of time the fine mesh would require, the medium mesh was used in the fixed ends geometry. In the case of one free end the finer mesh was used (Figure 3.23-Figure 3.22).

The meshes were created with the medial axis algorithm with minimising the mesh transition. The medial axis algorithm first decomposes the region to be meshed into a group of simpler regions. The algorithm then uses structured meshing techniques to fill each simple region with elements. If the region being meshed is relatively simple and contains a large number of elements, the medial axis algorithm generates a mesh faster than the advancing front algorithm. Minimising the mesh transition may improve the mesh quality. The meshes of the model are shown in Figure 3.25 and Figure 3.24.

3.4 Finite element model results

The mechanical response of the porcine thoracic aorta under internal pressure equal to the maximum physiological blood pressure is investigated. The stresses and stretches are presented for a combination of different geometries and material models. The first geometry represents an aorta tube fixed at the two ends while the second represents an aorta with one free end that is plugged. The plug was modelled as an elastin isotropic material with elastic modulus 200 GPa and Poisson's ratio ν = 0.3 For the two geometries three material models were implemented to describe the preconditioned and the not preconditioned mechanical behaviour of the porcine aorta. The three different material

models that were implemented are a linear isotropic elastic material model the elastin phase elastic modulus E_{el} as the elastic modulus and ν = 0.499999 for Poisson's ratio (almost incompressible material) and the two hyperelastic material models with the best fits, the 3rd order Ogden hyperelastic material model and the Holzapfel anisotropic hyperelastic material model that takes into consideration the collagen fibre reinforcement of the aortic wall. The stability of the hyperelastic materials was confirmed in ABAQUS with the Drucker stability criterion.

The results of the simulations are listed below in Figure 3.27 - Figure 3.32 and include the von Mises stress distribution along the aorta specimen, the maximum and minimum principal stresses and the circumferential and axial stretches of the aorta at the final position of the loading step for the different combinations of geometries and material models. In addition, in

Table 3.5 and Table 3.6 the dilation of the preconditioned and the not preconditioned tissue is calculated for the different material models and geometries at the end of the loading step.

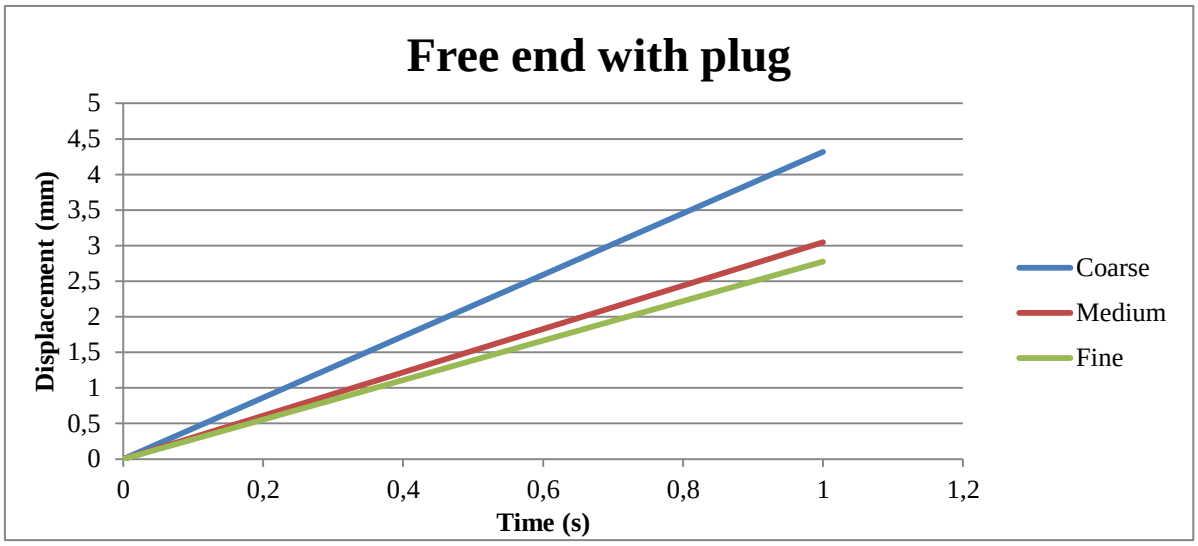

Figure 3.22: The radial displacement for the middle of the aorta for the three mesh densities for the free end with plug configuration.

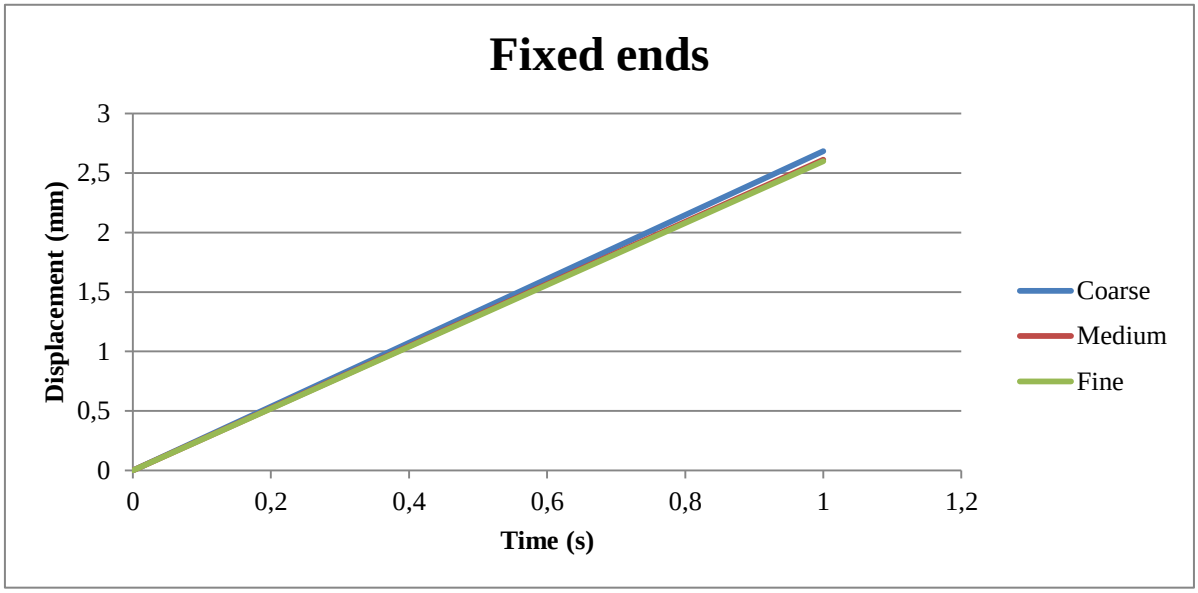

Figure 3.23: The radial displacement for the middle of the aorta for the three mesh densities for the fixed ends configuration.

Table 3.5: Circumferential stretches of the aorta model for the different geometries and material models at the end of the loading step (120 mmHg) compared to experimental data from inflation tests of porcine native thoracic aortas in the literature. The tissue in Guo & Kassab (2004) was not preconditioned while the tissue in Stergiopulos et al. (2001) and Kim & Baek (2011) was preconditioned.

		Circumferential stretch		Kim & Baek (2011)	Stergiopulos et al. (2001)	Guo & Kassab (2004)
		NP	P			
Fixed ends	Isotropic elastic	1.13	1.08	1.35	1.20	1.26
	Ogden 3rd order	1.28	1.19			
	Holzapfel	1.20	1.27			
Free end with plug	Isotropic elastic	1.20	1.10			
	Ogden 3rd order	1.35	1.26			
	Holzapfel	1.19	1.24			

Table 3.6: Axial stretch for the case of one free end with plug in percentage of the original length of the aorta model for the different material models at the end of the loading step (120 mmHg).

	Axial stretch		
	NP	P	Han & Fung (1995)
Isotropic elastic	0	0	1.20 – 1.45
Ogden 3rd order	1.23	1.20	
Holzapfel	1.03	1.08	

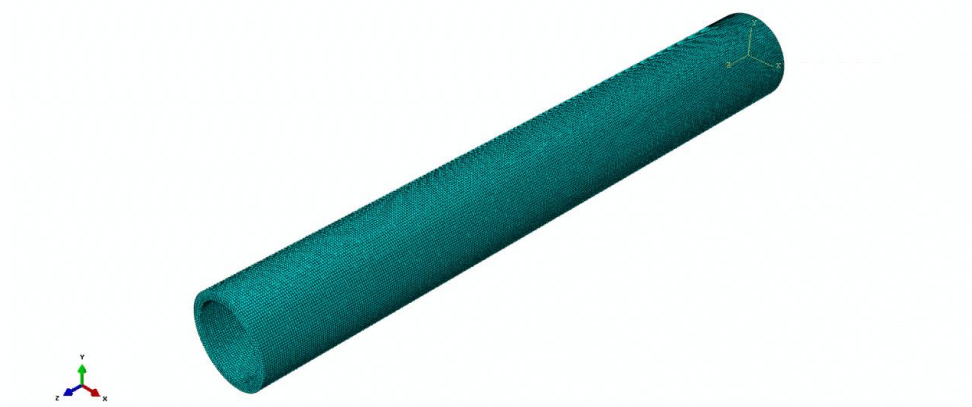

Figure 3.25: The fine mesh of the model.

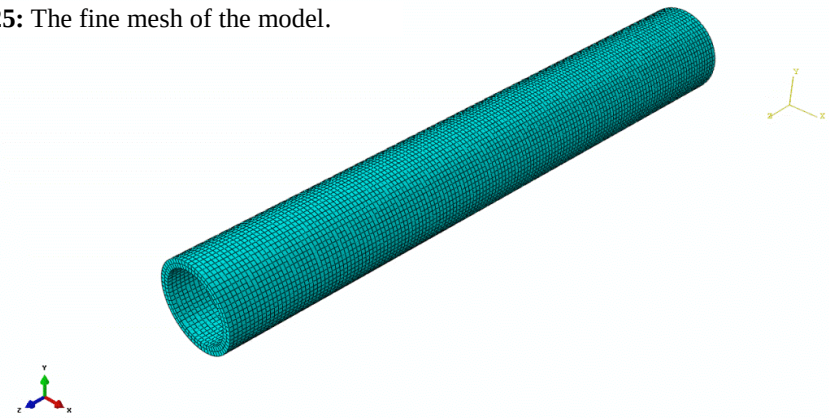

Figure 3.24: The medium mesh of the model.

Table 3.7: Values of Mises, maximum principal and minimum principal stresses in the aortic walls for the different material models and geometries at the end of the loading step (120 mmHg).

		Mises (kPa)		Max Principal (kPa)		Min Principal (kPa)	
		NP	P	NP	P	NP	P
Fixed ends	Isotropic elastic	7.37	7.37	7.37	7.37	0.02	0.02
	Ogden 3rd order	10.76	18.94	10.93	18.17	0.79	0.14
	Holzapfel	8.21	12.64	8.33	13.36	1.01	1.27
Free end with plug	Isotropic elastic	10.59	9.97	10.83	9.19	1.08	0.14
	Ogden 3rd order	10.94	29.39	14.55	30.35	0.20	1.11
	Holzapfel	9.25	13.67	9.27	14.53	1.21	1.45

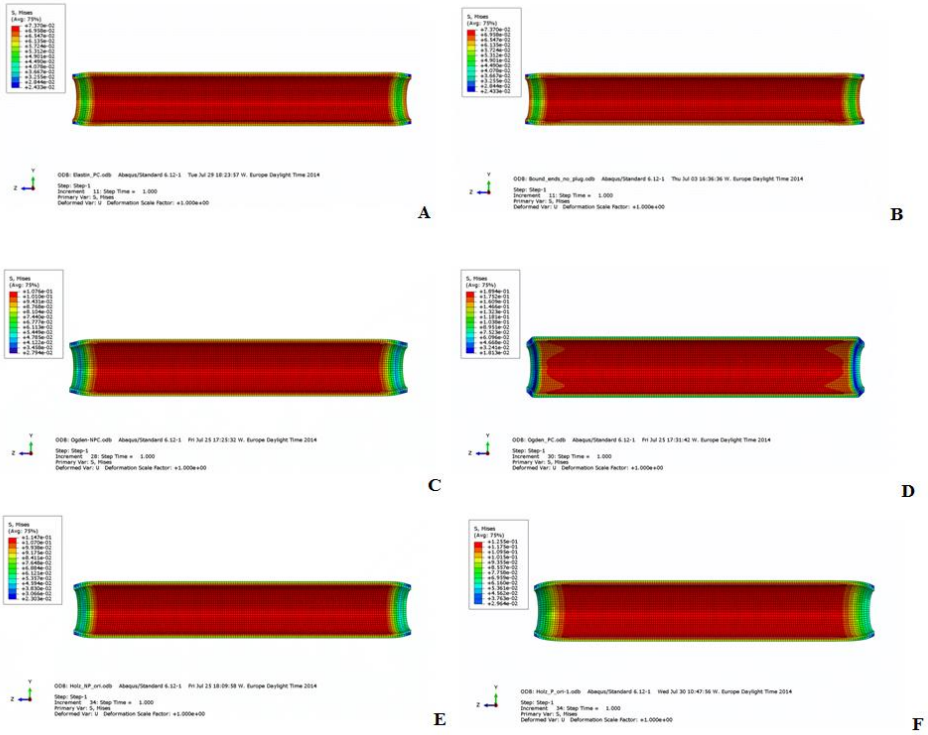

Figure 3.27: Von Mises stress distribution for the fixed ends geometry: (A) Linear elastic not preconditioned, (B) Linear elastic preconditioned, (C) Ogden not preconditioned, (D) Ogden preconditioned, (E) Holzapfel not preconditioned, (F) Holzapfel preconditioned.

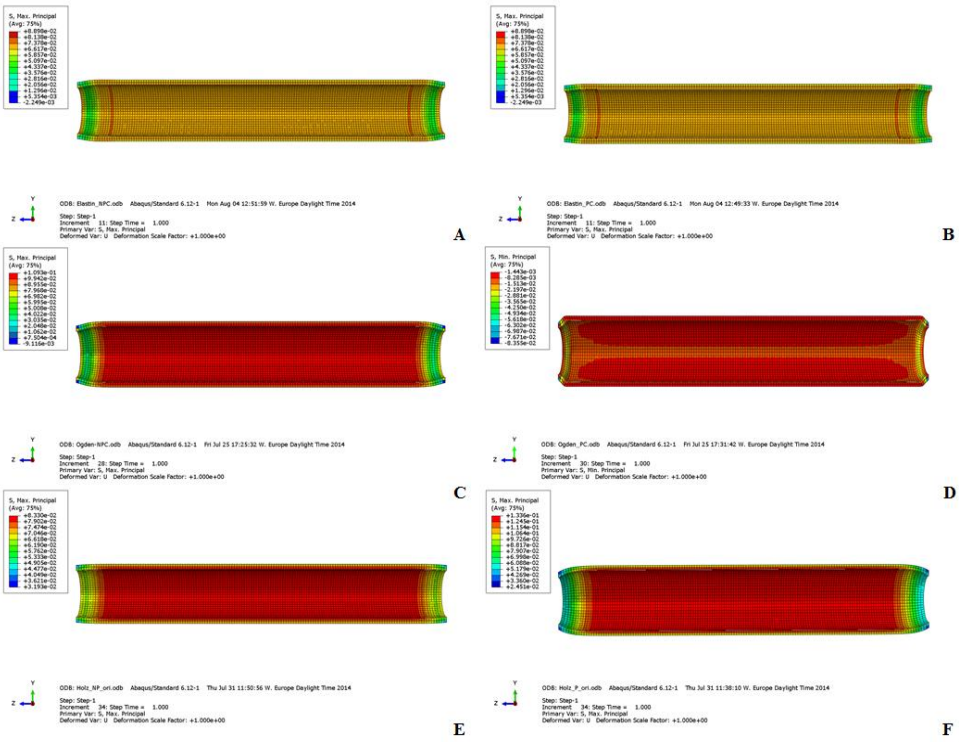

Figure 3.26: Maximum principal stress distribution for the fixed ends geometry: (A) Linear elastic not preconditioned, (B) Linear elastic preconditioned, (C) Ogden not preconditioned, (D) Ogden preconditioned, (E) Holzapfel not preconditioned, (F) Holzapfel preconditioned.

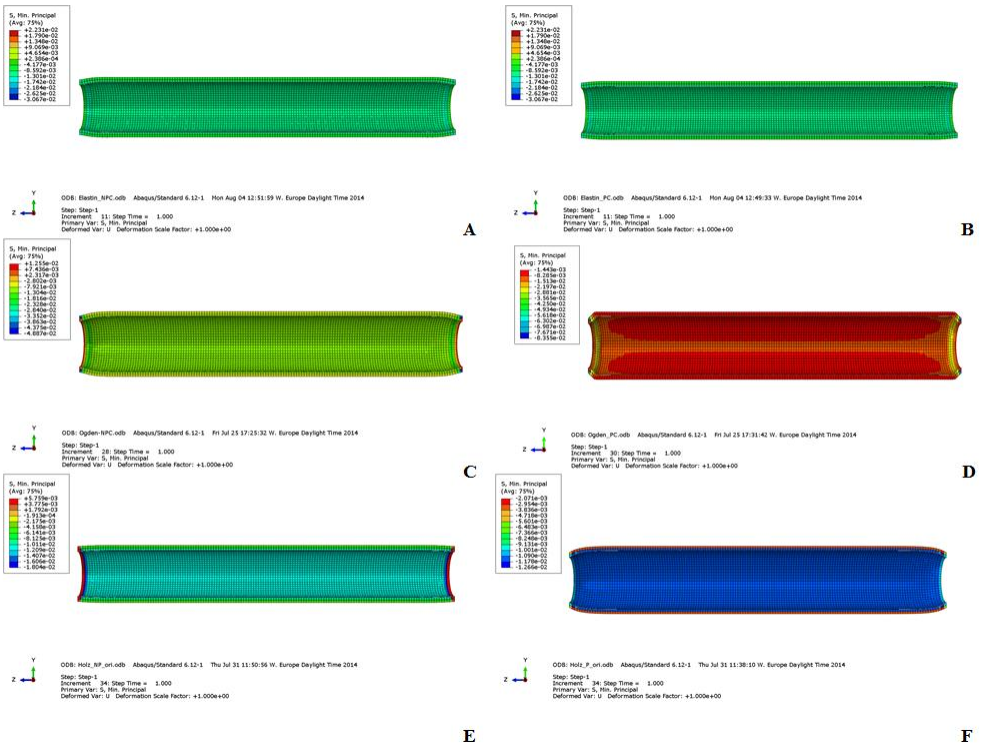

Figure 3.28: Minimum principal stress distribution for the fixed ends geometry: (A) Linear elastic not preconditioned, (B) Linear elastic preconditioned, (C) Ogden not preconditioned, (D) Ogden preconditioned, (E) Holzapfel not preconditioned, (F) Holzapfel preconditioned.

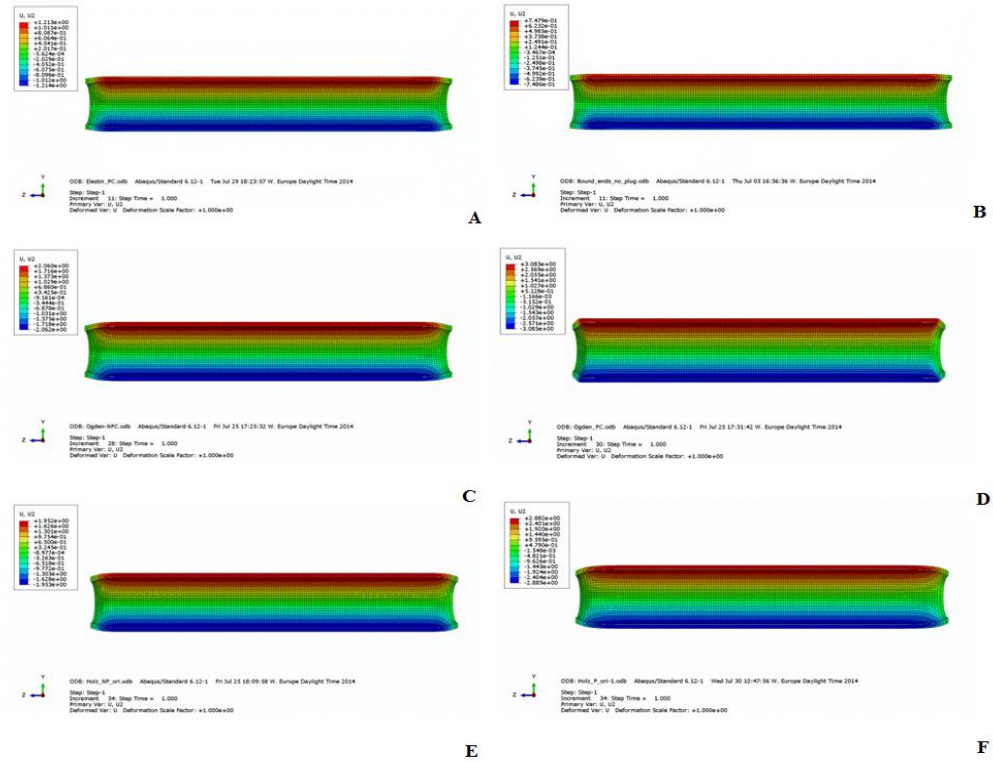

Figure 3.29: Displacement in the y – axis for the fixed ends geometry: (A) Linear elastic not preconditioned, (B) Linear elastic preconditioned, (C) Ogden not preconditioned, (D) Ogden preconditioned, (E) Holzapfel not preconditioned, (F) Holzapfel preconditioned.

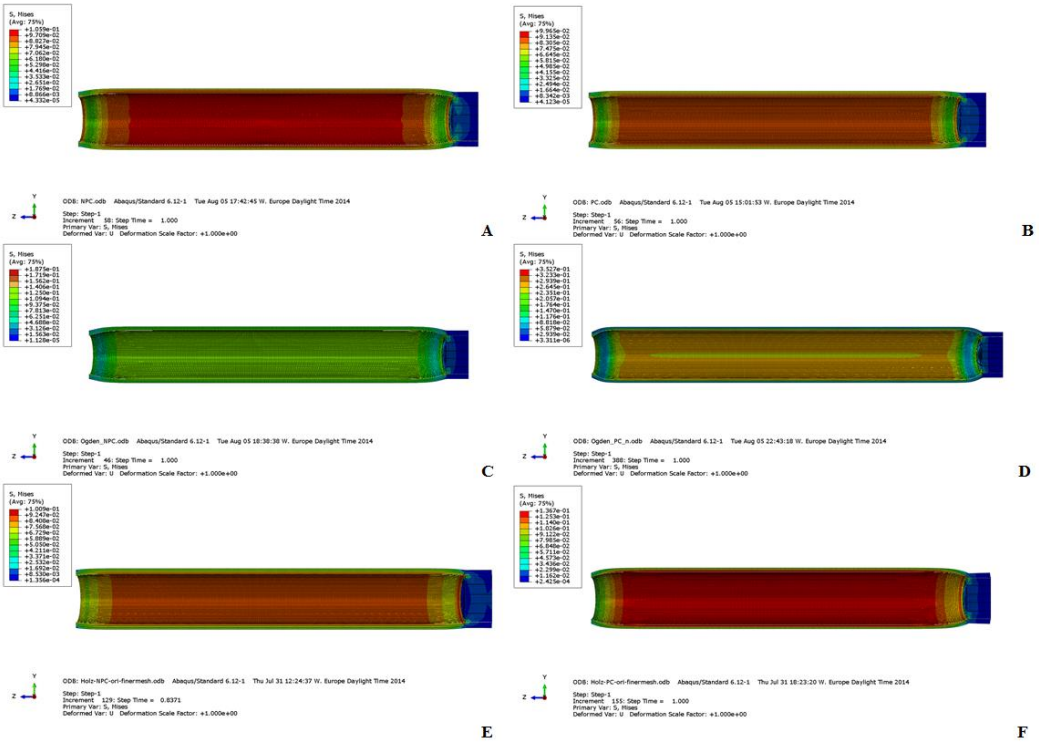

Figure 3.30: Von Mises stress distribution for the free end with plug geometry: (A) Linear elastic not preconditioned, (B) Linear elastic preconditioned, (C) Ogden not preconditioned, (D) Ogden preconditioned, (E) Holzapfel not preconditioned, (F) Holzapfel preconditioned.

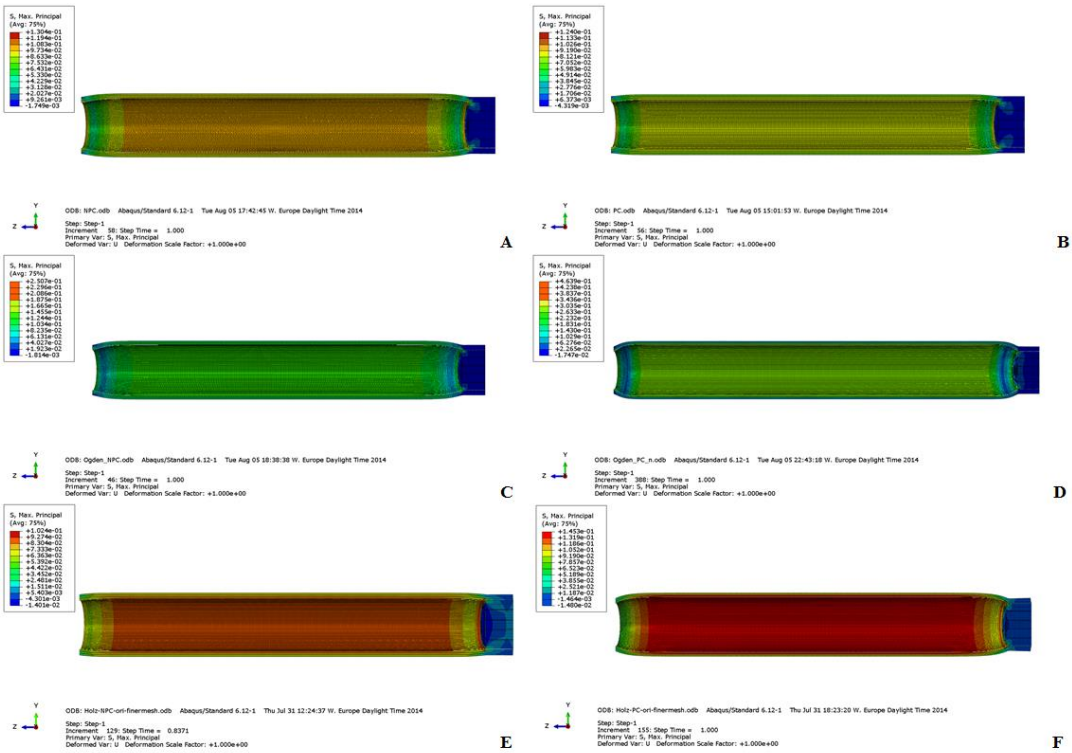

Figure 3.31: Maximum principal stress distribution for the free end with plug geometry: (A) Linear elastic not preconditioned, (B) Linear elastic preconditioned, (C) Ogden not preconditioned, (D) Ogden preconditioned, (E) Holzapfel not preconditioned, (F) Holzapfel preconditioned.

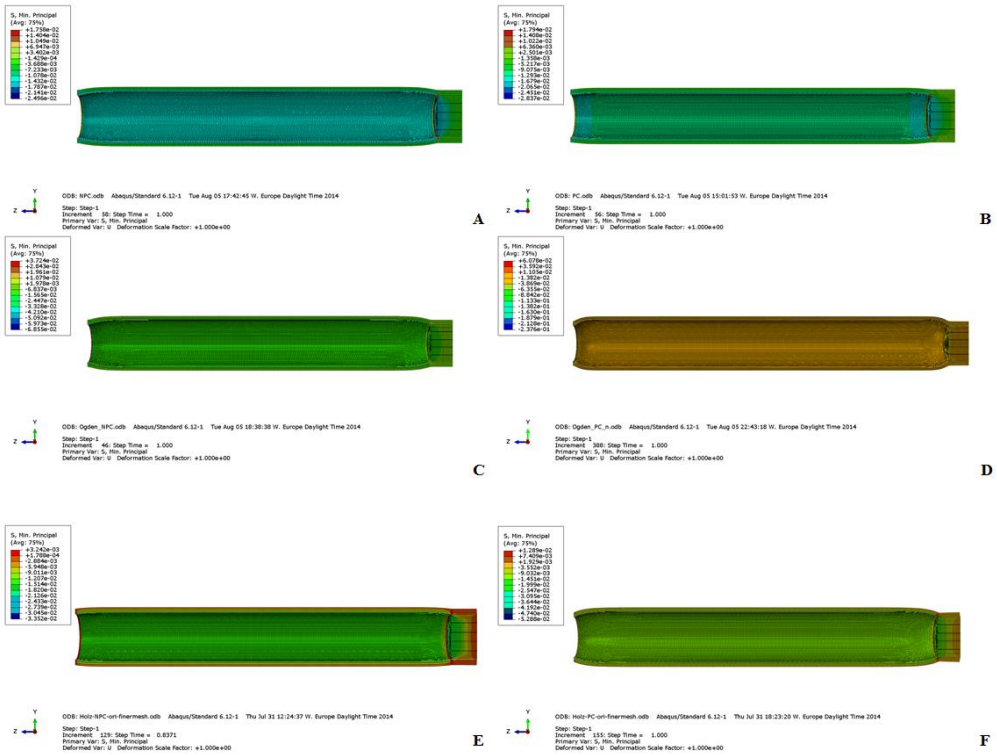

Figure 3.32: Minimum principal stress distribution for the free end with plug geometry: (A) Linear elastic not preconditioned, (B) Linear elastic preconditioned, (C) Ogden not preconditioned, (D) Ogden preconditioned, (E) Holzapfel not preconditioned, (F) Holzapfel preconditioned.

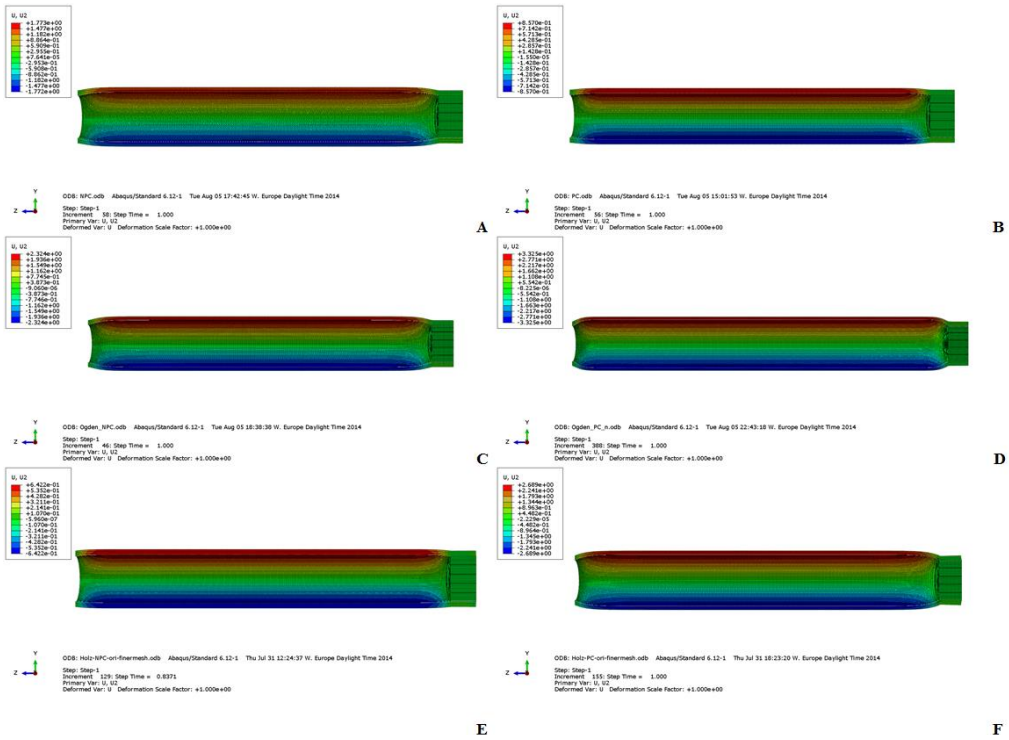

Figure 3.33: Displacement in the y – axis for the free end with plug geometry: (A) Linear elastic not preconditioned, (B) Linear elastic preconditioned, (C) Ogden not preconditioned, (D) Ogden preconditioned, (E) Holzapfel not preconditioned, (F) Holzapfel preconditioned.

4. DISCUSSION

4.1 Biomechanical testing

In this study, uniaxial tensile testing was carried out to investigate the characteristic stress – strain response of fresh porcine thoracic aorta, the effect of preconditioning to its material parameters and its anisotropy.

The stress – stress response of the tissue demonstrated the distinctive non – linear behaviour discussed in Chapter 2 which is related to the aortic wall histoarchitecture. This behaviour demonstrated the typical J – shaped curve with a low modulus region during the elastin phase and a high modulus region during the collagen phase.

The average thickness of the samples was 1.85 ± 0.16 mm and 1.87 ± 0.21 mm for the circumferential direction and axial direction respectively without preconditioning and 2.78 ± 0.37 mm and 2.52 ± 0.61 mm for the circumferential and axial directions respectively with preconditioning. Significant differences were detected between the preconditioned and not preconditioned groups for both directions. Since specimens for the experiments with and without preconditioning were procured different days from the abattoir the difference may be because the pigs used for the preconditioned tests were heavier. Despite that, stress is a property of the material and is not affected by the cross sectional area.

The load – elongation curves obtained from the uniaxial tests were converted to engineering stress – strain graphs. Although engineering stress does not take into account the reduction in the cross – sectional area of the specimen during loading, because of the easier calculation of the engineering stress and because the results were used for comparison between the preconditioned and the not preconditioned groups distinction between true and engineering stress and strain was deemed unnecessary.

Comparison with the t – test between the preconditioned and the not preconditioned groups showed significant differences between all the material parameters except for the transition stress and the elastin phase elastic modulus of the axial direction. Therefore, the results indicate that preconditioning indeed has an effect on the tissue parameters. The differences in the parameters between the preconditioned and the not preconditioned groups show that preconditioning made the tissue stiffer in both directions and increased its strength. These results make sense, considering the alignment of the collagen fibres in the direction of loading during preconditioning.

Preconditioning also had an effect on the anisotropy of the tissue. While in not preconditioned tissue anisotropy was strongly pronounced, preconditioned groups showed very similar stress – strain curves indicating an almost isotropic response. The isotropy that is introduced with the preconditioning may be because of the close proximity of the thoracic aorta to the aortic valve. Properties of aorta vary significantly along its length and distally the aorta becomes progressively stiffer circumferentially (Gundiah et al. 2008). It appears that preconditioning has an effect on the higher strains as axial and circumferential groups had similar elastin phases which suggests that the ground matrix does not play a role in the anisotropy of the tissue and that it is mainly a property exerted by the collagen fibres, thus the overlapping elastin phases in both directions.

4.2 Constitutive modelling and computational simulations

The stress – strain data obtained from the uniaxial tensile tests were used for the constitutive material model for the arterial wall. The material models were then used for a finite element model of the thoracic aorta under internal pressure of 120 mmHg and two different geometries.

From the material models that were tested, the Neo – Hookean, Mooney – Rivlin and reduced polynomial 3rd order were unable to describe the material behaviour of the aortic walls for both the preconditioned and not preconditioned states. The Ogden 3rd order and the Holzapfel anisotropic material models had the best fits and they were the ones used for the finite element simulations. Apart from the hyperelastic material models, a simple isotropic linearly elastic material model was implemented. It is known that during physiological loading inside the body the tissues do not surpass the transition phase, thus the first material model that was tested was the linearly elastic isotropic material with Young's modulus the elastin phase modulus and Poisson's ratio ν = 0.0499999.

The mesh sensitivity analysis showed that for the optimal results the mesh for the fixed ends geometry should be of a medium size (Figure 3.24) while for the one free end geometry the mesh should be a fine size (Figure 3.25). Computational time for the medium mesh was approximately 3 minutes while for the fine size 30'.

For both geometries the results on the dilation at the end of the load step were similar, with the one free end geometry having slightly more. According to the literature, inflation tests on porcine thoracic aortas give circumferential stretches of 1.20 – 1.26 (Stergiopulos et al. 2001; Guo & Kassab 2004) and axial stretches of about 1.20 – 1.45 (Han & Fung 1995) for preconditioned tissue. There seems to be a discrepancy in the literature between the preconditioned tissue and not preconditioned tissue circumferential stretches relation as in Guo & Kassab (2004) for not preconditioned inflation tests the circumferential stretches were higher than in Stergiopulos et al. (2001) and lower than in Kim & Baek (2011) for preconditioned inflation tests. A reason for this may be the size and age of the animals used for the tests. Stergiopulos et al. (2001) used ~80 kg animals while Guo & Kassab (2004) ~29 kg animals.

The circumferential stretches obtained when the linearly elastic material was used were 1.13 and 1.20 for the not preconditioned tissue and 1.08 and 1.10 for the preconditioned tissue. The axial stretches were 1 for both the preconditioned and not preconditioned tissue. The next material model that was used was the Ogden 3rd order. In this case the circumferential stretches calculated were closer to the ones found in the literature with 1.28 and 1.35 for the not preconditioned tissue and 1.19 and 1.26 for the preconditioned for fixed ends and one free end geometry respectively. The axial stretches were 1.23 for the not preconditioned tissue and 1.20 for the preconditioned tissue. Finally, the circumferential stretches for the fixed ends and one free end geometries were 1.20 and 1.19 for the not preconditioned tissue and 1.27 and 1.24 for the preconditioned tissue when the Holzapfel anisotropic material model was used. The axial stretches were 1.03 and 1.08 for the not preconditioned and preconditioned tissue respectively. The results indicate that in this particular FE model, the material model that was able to be closer to reality was the Ogden 3rd order hyperelastic material. Although the geometry of the FE model was a simplistic one, the results show that is an acceptable approximation when the correct material model is used.

The stresses in the aortic walls for all the cases were uniform along the length of the model (Figure 3.27 – Figure 3.33). The Mises, maximum and minimum principal stresses predicted by each model are summarised in Table 3.7. The maximum principal stresses were directed circumferentially and the minimum principal stresses radially.Figure 3.14:

The Holzapfel anisotropic material model has been applied in many situations and its validity is accepted (Holzapfel & Weizsäcker 1998; Gasser et al. 2006; Holzapfel 2006; Vychytil et al. 2012; Kim 2009). However, in this study it failed to give the best results. There are certain limitations in this study that can account for this result. Firstly, having considered the same material properties for all elements can be considered as another limitation of the analysis. A homogenised characterisation of the aorta was obtained, which was then used in the finite element model. The FE strains for the geometry of the aorta show a distribution of strains generally uniform throughout the volume, with concentration effects only at the constrained end, in agreement with that anticipated by theory. Secondly, the parameters γ and κ are to be invasively determined by confocal microscopy but here they were treated as additional material parameters. It has been reported that for the media layer of the aorta there are two fibers of families running at $\pm 15^{o}$ but this value was tested and only had acceptable fit with the not preconditioned data. As it seen be the residuals in Table 3.4: **Residual norms of LSQ regression against the experimental data preconditioned and not preconditioned.**Table 3.4 all the models had better fit with the not preconditioned data and struggled with the nearly isotropic response of the preconditioned data.

Because only strip samples were prepared for uniaxial tension tests, the data do not cover the whole physiological domain. Biaxial properties of specimens may help extend the present data. However, it is theoretically impossible to characterize the three – dimensional response of anisotropic elastic materials by planar biaxial tests alone. Moreover, this model cannot be used to characterize *in vivo* the response of the tissue because uniaxial tensile tests can only be performed on harvested tissue.

Finding a suitable model for aortic tissue is a challenging task, because of the complex three layered structure of the tissue. This complex structure has implications in the mechanical behaviour of the tissue, which responds non-linearly to loading. Moreover it is noteworthy that *in vivo* the aorta is subjected to a variety of loads: the axial pre-stretch, the circumferential residual stress, the cyclic inflation by blood pressure. Improvements can be: stripping the aortic wall into its three layers and determining the parameters for each layer and then modelling the aorta as a three layer vessel and determining for each layer the number of families and the orientations and dispersions with confocal microscopy for example, applying pulsatile flow of blood, the appropriate axial pre – stretches and circumferential residual stresses that are responsible for the opening angle of the vessels once it is cut axially, using MRI for the determination of the correct boundary conditions. The use of engineering stress – strain data instead of true stress may also account for differences between the computational and inflation test results. The first limitation to a wide application of this constitutive model is due to the lack of knowledge of the *in vivo* structural parameters γ and κ. Finally, determination of the passive mechanical properties of arterial walls is based not only on the distribution and orientation of tissue elements (layers) but also on their coupling. Hence, continued research is required to identify the related mechanics of tissue interconnection.

5. CONCLUSIONS

In this study, the significance of the process of preconditioning in uniaxial low strain rate tensile loading of the porcine thoracic aorta was investigated. In addition, a simple finite element model of the aorta was implemented for which the extent to which different material models could describe its stress – strain behaviour was evaluated. The major conclusions of the work are:

- Preconditioning affects the biomechanical properties of the porcine thoracic aorta and every biomechanical testing protocol should involve the process of preconditioning.
- The aorta's anisotropy almost vanishes after preconditioning.
- The linearly isotropic material model failed to describe adequately the behaviour of the aorta under internal pressure and thus the use of hyperelastic materials is mandatory.
- The Ogden hyperelastic material model was the best fit for the stress – strain data and gave the most realistic computational results.
- While the Holzapfel anisotropic material model has been proved to be valid for arteries, the limitations of its implementation in this study as described in the Discussion did not make it the best one.

REFERENCES

Barlow, J., 1976. Optimal Stress Locations in Finite Element Models. *International Journal for Numerical Methods in Engineering*, 10, pp.243–251.

Berillis, P., 2013. The Role of Collagen in the Aorta's Structure. *The Open Circulation and Vascular Journal*, 6(1), pp.1–8. Available at: http://benthamscience.com/open/openaccess.php?tocvj/articles/V006/1TOCVJ.htm.

Carew, E.O. et al., 1999. Quasilinear viscoelastic theory applied to internal shearing of porcine aortic valve leaflets. *J. Biomech Eng.*, 121, pp.386–392.

Carew, E.O. et al., 2004. Stress relaxation preconditioning of porcine aortic valves. *Annals of biomedical engineering*, 32(4), pp.563–72. Available at: http://www.ncbi.nlm.nih.gov/pubmed/15117030.

Carew, E.O., Barber, J.E. & Vesely, I., 2000. Role of preconditioning and recovery time in repeated testing of aortic valve tissues: validation through quasilinear viscoelastic theory. *Annals of biomedical engineering*, 28(9), pp.1093–100. Available at: http://www.ncbi.nlm.nih.gov/pubmed/11132193.

Carew, T.E., Vaishnav, R.N. & Patel, D.J., 1968. Compressibility of arterial walls. *Circulation Res.*, 23, pp.61–68.

Cheng, S., Clarke, E.C. & Bilston, L.E., 2009. The effects of preconditioning strain on measured tissue properties. *Journal of biomechanics*, 42(9), pp.1360–2. Available at: http://www.ncbi.nlm.nih.gov/pubmed/19394022 [Accessed June 2, 2014].

Chuong, C.J. & Fung, Y.C., 1984. Compressibility and constitutive equation of arterial wall in radial compression experiments. *J. Biomechanics*, 17(1), pp.35–40.

Dassault Systemes, 2012. *ABAQUS User Manual*, Simulia, Dassault Systemes.

Detweiler, D.K. & Erickson, H.H., 2004. Regulation of the Heart. In *Dukes' Physiology of Domestic Animals*. Reece W.O.

Ehret, A.E. & Itskov, M., 2007. A polyconvex hyperelastic model for fiber-reinforced materials in application to soft tissues. *Journal of Materials Science*, 8, pp.853–8 863.

Fung, Y.C., 1993. *Biomechanics: Mechanical Properties of Living Tissues* 2nd ed., New York, NY: Springer-Verlag New York, Inc.

Fung, Y.C., 1979. Pseudoelasticity of arteries and the choice of its mathematical expression of Applied Mechanics.

Gasser, T.C., Ogden, R.W. & Holzapfel, G. a, 2006. Hyperelastic modelling of arterial layers with distributed collagen fibre orientations. *Journal of the Royal Society, Interface / the Royal Society*, 3(6), pp.15–35. Available at:

http://www.pubmedcentral.nih.gov/articlerender.fcgi?artid=1618483&tool=pmcentrez&rendertype=abstract [Accessed May 26, 2014].

Gefen, A. et al., 2003. Age-dependent changes in material properties of the brain and braincase of the rat. *Journal of neurotrauma*, 20(11), pp.1163–77. Available at: http://www.ncbi.nlm.nih.gov/pubmed/14651804.

Gundiah, N. et al., 2008. Significant material property differences between the porcine ascending aorta and aortic sinuses. *Journal of Heart Valve Disease*, 17, pp.606–613.

Guo, X. & Kassab, G.S., 2004. Distribution of stress and strain along the porcine aorta and coronary arterial tree. *American journal of physiology. Heart and circulatory physiology*, 286(6), pp.H2361–8. Available at: http://www.ncbi.nlm.nih.gov/pubmed/15148060.

Han, H.C. & Fung, Y.C., 1995. Longitudinal strain of canine and porcine aortas. *Journal of Biomechanics*, 28(5), pp.637–641.

Hariton, I. et al., 2007. Stress-driven collagen fiber remodeling in arterial walls. *Biomechanics and Modeling in Mechanobiology*, 6, pp.163–175.

Haut, R.C. & Little, R.W., 1972. A constitutive equation for collagen fibres. *J Biomech*, 5, pp.423–430.

Hayashi, K., 1993. Experimental approaches on measuring the mechanical properties and constitutive laws of arterial walls. *Journal of biomechanical engineering*, 115(4B), pp.481–8. Available at: http://www.ncbi.nlm.nih.gov/pubmed/8302029.

Holzapfel, G.A., 2000. Biomechanics of Soft Tissue. In J. Lemaitre, ed. *Handbook of Material Behavior: Nonlinear Models and Properties*. Academic Press.

Holzapfel, G.A., 2006. Determination of material models for arterial walls from uniaxial extension tests and histological structure. *Journal of theoretical biology*, 238(2), pp.290–302. Available at: http://www.ncbi.nlm.nih.gov/pubmed/16043190 [Accessed August 7, 2014].

Holzapfel, G.A., Gasser, T.C. & Ogden, R.W., 2001. A New Constitutive Framework for Arterial Wall Mechanics and a Comparative Study of Material Models. , pp.1–48.

Holzapfel, G.A. & Weizsäcker, H.W., 1998. Biomechanical behavior of the arterial wall and its numerical characterization. *Computers in biology and medicine*, 28(4), pp.377–92. Available at: http://www.ncbi.nlm.nih.gov/pubmed/9805198.

Humphrey, J., 1995. Mechanics of the arterial wall: Review and directions. *Crit Rev Biomed Eng*, 23, pp.1–162.

Itskov, M., Ehret, A.E. & Mavrilas, D., 2006. A polyconvex anisotropic strain-energy function for soft collagenous tissues. *Biomechanics and Modeling in Mechanobiology*, 5, pp.17–26.

Kassab, G.S., 2006. Biomechanics of the cardiovascular system: the aorta as an illustratory example. *Journal of the Royal Society, Interface / the Royal Society*, 3(11), pp.719–40. Available at: http://www.pubmedcentral.nih.gov/articlerender.fcgi?artid=1885359&tool=pmcentrez&rendertype=abstract [Accessed June 2, 2014].

Kim, H.S., 2009. *Nonlinear multi-scale anisotropic material and structural models for prosthetic and native nonlinear multi-scale anisotropic material and structural models for prosthetic and native*. Georgia Institute of Technology.

Kim, J. & Baek, S., 2011. Circumferential variations of mechanical behavior of the porcine thoracic aorta during the inflation test. *Journal of biomechanics*, 44(10), pp.1941–7. Available at: http://www.ncbi.nlm.nih.gov/pubmed/21550609 [Accessed August 7, 2014].

King, M.W., 2014. The Medical Biochemistry Page. Available at: http://themedicalbiochemistrypage.org/index.php.

Korossis, S.A., 2002. *Biomechanics & Hydrodynamics of Decellularised Aortic Valves for Tissue Engineering*. Leeds.

Kwan, M.K., Lin, T.H.C. & Woo, S.L.-Y., 1993. On the viscoelastic properties of the anteromedial bundle of the anterior cruciate ligament. *J. Biomech*, 26, pp.447–452.

Latif, N. et al., 2005. Localization and pattern of expression of extracellular matrix components in human heart valves. *The Journal of heart valve disease*, 14(2), pp.218–27.

Marieb, E.N. & Hoehn, K., 2013. *Human Anatomy & Physiology* 9th ed., Pearson.

Miller, K.S. et al., 2012. Effect of preconditioning and stress relaxation on local collagen fiber re-alignment: inhomogeneous properties of rat supraspinatus tendon. *Journal of biomechanical engineering*, 134(3), p.031007. Available at: http://www.pubmedcentral.nih.gov/articlerender.fcgi?artid=3644292&tool=pmcentrez&rendertype=abstract [Accessed June 2, 2014].

OpenStax ed., 2013. *Anatomy & Physiology*, Rice University.

Pinto, J.G. & Patitucci, P.J., 1980. Visco-elasticity of passive cardiac muscle. *J. Biomech. Eng.*, 102, pp.57–61.

Quinn, K.P. & Winkelstein, B. a, 2011. Preconditioning is correlated with altered collagen fiber alignment in ligament. *Journal of biomechanical engineering*, 133(6), p.064506. Available at: http://www.ncbi.nlm.nih.gov/pubmed/21744935 [Accessed June 2, 2014].

Ricard-Blum, S., 2011. The collagen family. *Cold Spring Harbor perspectives in biology*, 3(1). Available at: http://www.pubmedcentral.nih.gov/articlerender.fcgi?artid=3003457&tool=pmcentrez&rendertype=abstract.

Sauren, A.A.H.J. et al., 1983. The mechanical properties of porcine aortic valve tissues. *J. Biomech.*, 16, pp.327–337.

Schatzmann, L., Brunner, P. & Stäubli, H.U., 1998. Effect of cyclic preconditioning on the tensile properties of human quadriceps tendons and patellar ligaments. *Knee surgery, sports traumatology, arthroscopy : official journal of the ESSKA*, 6 Suppl 1, pp.S56–61. Available at: http://www.ncbi.nlm.nih.gov/pubmed/9608465.

Stergiopulos, N. et al., 2001. Assessing the homogeneity of the elastic properties and composition of the pig aortic media. *Journal of vascular research*, 38(3), pp.237–46. Available at: http://www.ncbi.nlm.nih.gov/pubmed/11399896.

Su, W.-R., Chen, H.-H. & Luo, Z.-P., 2008. Effect of cyclic stretching on the tensile properties of patellar tendon and medial collateral ligament in rat. *Clinical biomechanics (Bristol, Avon)*, 23(7), pp.911–7. Available at: http://www.ncbi.nlm.nih.gov/pubmed/18485553 [Accessed June 2, 2014].

Takamizawa, K. & Hayashi, K., 1987. Strain energy density function and uniform strain hypothesis for arterial mechanics. *J Biomech*, 20, pp.7–17.

Teramoto, A. & Luo, Z.-P., 2008. Temporary tendon strengthening by preconditioning. *Clinical biomechanics (Bristol, Avon)*, 23(5), pp.619–22. Available at: http://www.ncbi.nlm.nih.gov/pubmed/18192094 [Accessed June 2, 2014].

Vychytil, J. et al., 2012. Constitutive modelling of an arterial wall supported by microscopic measurements. *Applied and Computational Mechanics*, 6, pp.107–118.

Weinhaus, A.J. & Roberts, K.P., 2009. Anatomy of the Human Heart. In P. A. Iaizzo, ed. *Handbook of Cardiac Anatomy, Physiology and Devices*. Humana Press Inc. Totowa, NJ, pp. 51–79.